9-25-2013 12:00 AM

Finite Element Analyses of Single-Edge Bend Specimens for J-R Curve Development

Yifan Huang
The University of Western Ontario

Supervisor
Dr. Wenxing Zhou
The University of Western Ontario

Graduate Program in Civil and Environmental Engineering
A thesis submitted in partial fulfillment of the requirements for the degree in Master of Engineering Science

FINITE ELEMENT ANALYSES OF SINGLE-EDGE BEND SPECIMENS FOR *J-R* CURVE DEVELOPMENT

(Thesis format: Integrated Article)

by

Yifan Huang

Graduate Program in Engineering Science
Department of Civil and Environmental Engineering

A thesis submitted in partial fulfillment
of the requirements for the degree of
Master of Engineering Science

The School of Graduate and Postdoctoral Studies
The University of Western Ontario
London, Ontario, Canada

Abstract

The fracture toughness resistance curve such as the *J*-integral resistance curve (*J-R* curve) is widely used in the integrity assessment and strain-based design of energy pipelines with respect to planar defects (i.e. cracks). Two studies about the development of the *J-R* curve are carried out and reported in this thesis. In the first study, the plastic geometry factor, i.e. the η_{pl} factor, used to evaluate *J* in a *J-R* curve test based on the single-edge bend (SE(B)) specimen is developed based on the three-dimensional (3D) finite element analysis (FEA). The main finding of this study is that besides the crack length, both the thickness and side grooves of the specimens have observable impacts on the η_{pl} factor. The η_{pl} factors obtained from 3D FEA are different from those obtained from two-dimensional (2D) FEA. The results of this study can improve the accuracy of the experimentally determined *J-R* curve and facilitate the use of non-standard (e.g. shallow-cracked) SE(B) specimens for the *J-R* curves testing. In the second study, 3D FEA is carried out on SE(B) specimens for which the *J-R* curves have been experimentally determined to develop the constraint-corrected *J-R* curves for X80 grade pipe steels. The constraint parameters considered in this study include Q, A_2, h and T_z. Several different forms of the Q parameter that account for the correction for the load and/or bending stresses are considered. It is observed that three constraint parameters, namely Q_{BM1}, T_z and A_2, lead to reasonably accurate constraint-corrected *J-R* curve for a wide range of crack extension compared with the *J-R* curves experimentally determined from two shallow cracked SE(B) specimens. On the other hand, the constraint-corrected *J-R* curve based on constraint parameters Q_{HRR}, Q_{BM2} and Q_m lead to a relatively large error of prediction. The approach for constructing the constrain-corrected *J-R* curve can be used to develop the structure-specific *J-R* curve based on those obtained from small-scale test specimens to improve the accuracy of the structural integrity assessment.

Keywords

Fracture toughness; *J-R* curve; Three-dimensional (3D); Finite element analysis (FEA); Single-edge notched bend (SE(B)); η_{pl} factor; Constraint

Co-Authorship

A version of Chapter 2 co-authored by Wenxing Zhou, Enyang Wang and Guowu Shen has been accepted as a technical paper and presented in *the 23rd International Offshore and Polar Engineering Conference* (ISOPE 2013) in Anchorage, Alaska between June 30 and July 5, 2013.

An extended version of Chapter 2 co-authored by Wenxing Zhou and Zijian Yan has been submitted to the *International Journal of Pressure Vessels and Piping* as a technical paper.

Chapter 3 is being prepared as a technical paper co-authored by Wenxing Zhou and Enyang Wang, and will be submitted to *Fatigue & Fracture of Engineering Materials & Structures*.

Dedication

To my parents, Qianwen Tan and Bowen Huang

Acknowledgments

My deepest gratitude goes first and foremost to Dr. Wenxing Zhou, my supervisor, for his patient guidance, understanding, encouragement, and most importantly for continuously supporting me with his profound insight throughout this study. He has walked me through all the stages of the writing of this thesis. Without his consistent and illuminating instruction, this thesis could not have reached its present form. It has been a great privilege and joy of being a member of his research group and studying under his guidance and supervision.

I would also like to thank Dr. Ashraf A. El Damatty, Dr. Tim A. Newson and Dr. Robert Klassen for being my examiners and for their constructive advice to this thesis. I would also express my gratitude to Dr. Guowu Shen, senior research scientist at CANMET-MTL and Adjunct Professor in the Department of Civil and Environmental Engineering at Western, for his valuable comments and suggestions during a project in my thesis.

My special thanks to all my colleagues and alumni in our research group: Enyang Wang, Shenwei Zhang, Guoxiong Huang, Ning Zhang, Mohammad Al-Amin, Bernard Kim, Zijian Yan and Hao Qin, for making my graduate life so enjoyable and also for their encouragement and assistances. A friend in need is a friend indeed!

Financial support provided by TransCanada and the Natural Sciences and Engineering Research Council of Canada (NSERC) and by the Faculty of Engineering at Western University is gratefully acknowledged.

Last my hearty thanks would go to my parents and grandparents for their loving considerations and great confidence in me all through these years. I am really grateful to my aunt and my uncle who helped me a lot in both my studying and living. Without the support of my family, I could not fulfill my dream to study abroad. I also owe my sincere gratitude to Guigui Zu for her love, encouragement and support throughout my Master's program.

Table of Contents

List of Tables

List of Figures

List of Nomenclature

A = area under the load-displacement curve

A_1 = parameter in the J-A_2 solution

A_2 = constraint parameter

A_C = area of the cracked body

A_{CMOD} = area under the load versus *CMOD* curve

A_{el}, A_{pl} = the elastic and plastic component of area under load-displacement curve

A_{LLD} = area under the load versus *LLD* curve

A_{pl}^{LLD} = Plastic area under the load versus *LLD* curve

A_{pl}^{CMOD} = Plastic area under the load versus *CMOD* curve

$A_{pl}^{i,i+1}$ = area of AB $\Delta_{pl}^{i}\Delta_{pl}^{i+1}$ in Fig. 2.4

$\bar{A}_{pl}$ = non-dimensionalized plastic area

a = crack length

a_0 = initial crack length

a_i, a_{i+1} = values of a at step i and step i+1

B = thickness of the specimen

B_e = effective thickness of the specimen

B_N = net thickness of the specimen

b = length of the uncracked ligament

b_i, b_{i+1} = values of b at step i and step i+1

C = linearization factor in bending correction of Q

CMOD, V = crack mouth opening displacement

C(T) = compact tension

CTOD = crack tip opening displacement

C_1, C_2 = power-law coefficients of J-R curves

C_i = compliance obtained in the i th loading-unloading sequence

C_i^{CMOD} = *CMOD*-based compliance obtained in the i th loading-unloading sequence

$C_{c(i)}^{CMOD}$ = rotation corrected compliance obtained in the i th loading-unloading sequence

ds = the length increment

$d\lambda$ = scalar factor of proportionality in the associate flow rule

E = elastic modulus

E' = effective modulus of elasticity

EPFM = elastic plastic fracture mechanics

e = error of the J values in the predicted J-R curves

f_{ij} = dimensionless function of θ

G = energy release rate

h = stress triaxiality parameter

I_n = integration constant that depends on n

J = nonlinear energy release rate

$J_{0.2}$, $J_{1.0}$ =J values corresponding to crack extensions of 0.2 and 1.0 mm in a J-R curve

J_2 = the second invariant of the deviatoric stress tensor

J_{ave} = the average J value along the crack front

J_{el} = elastic component of J

J_{Ic}, K_{Ic} = fracture toughness

J_{loc} = the local J value at each layer along the crack front

J_{mid} = the local J value at the mid-plane of the crack front

J_{pl} = plastic component of J

J_{pl}^{B} = value of J_{pl} at B or the intermediate value of J_{pl} between step i and step i+1

J_{pl}^{i}, J_{pl}^{i+1} = values of J at step i and step i+1

$J_{\Delta ai}$ = the J values corresponding to a certain crack extensions in a J-R curve

$\bar{J}_{pl}$ = non-dimensionalized J

K = stress intensity factor

K_c = critical stress intensity factor

k, L = characteristic length that can be simply set equal to 1 mm

LEFM = linear elastic fracture mechanics

LLD, Δ = load-line displacement

LSY = large scale yielding

M = moment per unit thickness acting at the center of the cross section

MBL = modified boundary layer

n = strain hardening exponent

n_j = the component of the unit normal vector to Γ

P = Applied concentrated force

P^i, P^{i+1} = values of P at step i and step i+1

P_l = reference load

Q = constraint parameter

Q_{HRR}, Q_{SSY} = Q parameters based on HRR solution and small scale yielding analysis

Q_m, Q_{BM} = load-dependence modified and bending corrected Q parameters

q_i = fitting coefficients of the function of C_1 and C_2

r, θ = coordinates in the polar coordinate system near the crack tip

r_p = the size of the plastic zone ahead of the crack tip

r_w = radius of the blunt crack tip in FEA model

S = the span of the specimen

SE(B) = single-edge bend

SE(T) = single-edge tension

SSY = small scale yielding

s_1, s_2, s_3 = the stress power exponents in the J-A_2 solution

s_{ij} = the deviatoric stress tensor

T_i = traction vectors

T_z = out-of-plane constraint parameter

t_i = the component or directional cosine of the unit tangent vector along the crack front as shown in Fig. A.2

U = strain energy

u_i = components of the displacement

V_C = volume of the cracked body

V_{pl} = plastic component of *CMOD*

W = the width of the specimen

w = the strain energy density

Y = general constraint parameter

α = coefficient in the Ramberg-Osgood stress-strain relationship

Γ = arbitrary counterclockwise contour around the crack tip

γ = plastic geometry factor used to calculate J_{pl} for a growing crack

γ_i = values of γ at step i

ΔA_C = the increase in crack area during the virtual crack extension

Δa = crack extension

Δa_1, Δa_2 = any two crack extensions

Δ_{el}, Δ_{pl} = the elastic and plastic component of *LLD*

Δ_{pl}^{i}, Δ_{pl}^{i+1} = values of Δ_{pl} at step i and step i+1

δ_{ij} = Kronecker delta

ε_0 = reference strain, $\varepsilon_0 = \sigma_0/E$

ε_{ij}, ε_{ij}^{pl} = total and plastic strain tensor

η = geometry factor used to calculate J

η_{ave} = plastic geometry factor corresponding to the average J value along the crack front

η_{ave}^{LLD}, η_{ave}^{CMOD} = *LLD*- and *CMOD*- based η_{ave}

η_{mid} = plastic geometry factor corresponding to the local J value at the mid-plane.

η_{mid}^{LLD}, η_{mid}^{CMOD} = *LLD*- and *CMOD*- based η_{mid}

η_{pl} = plastic geometry factor used to calculate plastic component of J

η_{pl}^{LLD}, η_{pl}^{CMOD} = *LLD*- and *CMOD*- based η_{pl}

η_{pl}^{i} = value of η_{pl} at step i

σ_0 = reference stress

σ_{22}^{FEA}, σ_{22}^{HRR} = opening stress ahead of the crack tip obtained from the finite element analysis and HRR solution

σ_e = the von Mises effective stress

σ_h = the hydrostatic stress

σ_{ij} = stress tensor

$(\sigma_{ij})_{HRR}$ = stress state obtained in HRR plane-strain solution

$(\sigma_{ij})_{SSY}$ = stress field corresponding to the small-scale yielding solution

$(\sigma_{ij})_{ref}$ = reference stress state used to determine constraint parameter Q

σ_{UTS} = ultimate tensile stress

σ_y = yield strength of the material

$\tilde{\sigma}_{ij}$, $\tilde{\varepsilon}_{ij}$ = dimensionless functions of n, θ in the HRR solution

$\tilde{\sigma}_{ij}^{(k)}$ = angular functions in J-A_2 solution

ν = Poisson's ratio

Chapter 1 Introduction

1.1 Background

Pipelines are effective and safe means to transport large quantity of hydrocarbons over a long distance (PHMSA 2012). Recent years have witnessed the rapid developments of the pipeline industry. According to the Canadian Energy Pipeline Association, there are over 100,000 km of oil and gas transmission pipelines in Canada. It is reported that about $85.5 billion worth of hydrocarbons were shipped through the 71,000 km long pipelines regulated by the National Energy Board (NEB) of Canada in 2010 (NEB 2010).

Energy pipelines may contain planar defects, i.e. cracks, in the pipe base metal and weldments due to various causes such as stress corrosion cracking, fatigue and the welding process. The fracture toughness of the pipe steel and weldments is a key input to the structural integrity assessment of pipelines with respect to planar defects. The fracture toughness also governs the tensile strain capacity of the pipeline, which is a critical component of the strain-based design methodology that is being increasingly used to design pipelines subjected to large plastic deformations resulting from, for example, frost heave, thaw settlement and earthquake-induced ground movements.

For ductile materials such as the modern pipe steels, the fracture process is often accompanied by relatively large plastic deformation at the crack tip and considerable crack extension. In this case, the fracture toughness is typically characterized by the so-called fracture toughness resistance curve that is generally represented by either the *J*-integral resistance curve (*J-R* curve) or the crack tip opening displacement (*CTOD*) resistance curve (*CTOD-R* curve) (Anderson, 2005).

The fracture toughness resistance curve is typically determined from small-scale test specimens such as the single-edge notched bend (SE(B)) and compact tension (C(T)) specimens, which have been standardized in standards such as ASTM E1820-11E2 (ASTM, 2013) and BS748 (BSI, 1997). It is well recognized that the fracture resistance curve depends on the crack tip constraint, defined as a structural obstacle against plastic deformation and dependent on the loading and geometry conditions of the specimens

(Yuan and Brocks, 1998). A high level of constraint results in a low toughness resistance curve, and a low level of constraint results in a high toughness resistance curve (Yuan and Brocks, 1998). Standard SE(B) and C(T) specimens are deeply cracked to ensure high constraint levels at the crack tip such that the corresponding fracture resistance curves represent the lower bound values. On the other hand, the crack tip constraint level for real cracks in pipelines is typically low because real cracks are generally shallow cracks. The application of the fracture resistance curve obtained from high-constraint specimens to low-constraint real structures may lead to overly conservative design and assessment. This is known as the fracture toughness transferability issue.

Over the last decade, non-standard test specimens such as single-edge notched tensile (SE(T)) and shallow-cracked SE(B) specimens have been investigated to address the fracture toughness transferability (e.g. Dodds et al., 1997). Research (Zhu and Jang, 2001) has also been carried out to develop the so-called constrain-corrected *J-R* curves, i.e. the *J-R* curve parameterized by commonly used constraint parameters Q or A_2 (O'Dowd and Shih, 1991; Yang et al., 1993a and 1993b).

1.2 Fundamentals of Fracture Mechanics

1.2.1 Linear Elastic Fracture Mechanics

Fracture mechanics can be separated into two main domains: the linear elastic fracture mechanics (LEFM) and the elastic plastic fracture mechanics (EPFM) (Anderson, 2005). LEFM attempts to describe the fracture behavior of a material when the plastic deformation is confined to a small region surrounding the crack tip, known as the small scale yielding (SSY) condition. On the other hand, EPFM applies to the large scale yielding (LSY) where significant plasticity in the vicinity of the crack tip is considered.

There are three typical loading modes in fracture mechanics (see Fig. 1.1), namely the opening mode (mode I), the in-plane shearing mode (mode II), and the out-of-plane shearing mode (mode III) (Anderson, 2005). This thesis is focused on the Mode I

loading because it is the most critical fracture mode for ductile metals. All the discussions thereafter are with respected to the Mode I loading.

Consider an isotropic linear elastic body containing a crack as illustrated in Fig. 1.2. Define a polar coordinate system with the origin located at the crack tip. The stress field at the crack tip can be written as (Irwin, 1957; Williams, 1957):

$$\lim_{r\to 0}\sigma_{ij} = \left(\frac{K}{\sqrt{2\pi r}}\right) f_{ij}(\theta) \tag{1.1}$$

where σ_{ij}[1] is the stress tensor; r and θ are coordinates defined in Fig. 1.2; f_{ij} is a dimensionless function of θ, and K is the so-called stress intensity factor in the unit of force/area×(length)$^{0.5}$. Equation (1.1) describes a stress singularity at the crack tip, because σ_{ij} approaches infinity as $r\to 0$. The stress intensity factor completely defines the amplitude of the stress singularity; that is, the stresses, strains and displacements near the crack tip can be completely determined given K (Anderson, 2005).

This single-parameter characterization by K relies on satisfaction of the SSY condition, which requires the zone of plastic deformation to be contained well within the singularity fields (Hutchinson, 1983). The size of the plastic zone ahead of the crack tip, r_p, can be approximately calculated using the following equation (Hutchinson, 1983):

$$r_p = \begin{cases} \dfrac{1}{3\pi}\left(\dfrac{K}{\sigma_y}\right)^2 & (\text{plane strain}) \\ \dfrac{1}{\pi}\left(\dfrac{K}{\sigma_y}\right)^2 & (\text{plane stress}) \end{cases} \tag{1.2}$$

[1] In this thesis, only i, j = 1, 2, or 3 are the subscripts of tensors. All symbols with other subscripts denote scalars.

where σ_y is the yield strength. The ASTM standard for experimentally determining the linear elastic plane strain fracture toughness of metallic materials, ASTM E399 (ASTM, 2013), requires the crack length and uncracked ligament of the test specimen to be not less than $25r_p$ at the point of fracture to satisfy SSY. Generally speaking, SSY is considered reasonable if the applied load is less than half the limit load at which plastic yielding extends throughout the uncracked ligament (Hutchinson, 1983). In SSY, the energy release rate G, defined as the rate of decrease in the potential energy with a unit increase in the crack area (Irwin, 1956), can be related to the stress intensity factor K as follows:

$$G = \begin{cases} \dfrac{(1-\nu^2)}{E} K^2 & (\text{plane strain}) \\ \dfrac{1}{E} K^2 & (\text{plane stress}) \end{cases} \tag{1.3}$$

where ν is Poisson's ratio and E denotes the elastic modulus.

For a given material at a given temperature, there exists a critical stress intensity factor, K_c , associated with the onset of crack growth under the monotonic loading (Hutchinson, 1983). In particular, the critical stress intensity factor in mode I, plane-strain condition is called the fracture toughness of the material at the given temperature and denoted by K_{Ic}. K_{Ic} is expected to be a material property (Broek, 1986). To ensure the plane-strain condition in the fracture toughness test, ASTM E399 (ASTM, 2013) also requires the thickness of the test specimen to be at least $25r_p$.

For highly brittle materials, cracks will run dynamically once K reaches K_{Ic}, and K_{Ic} remains constant during the crack growth. For more ductile materials, however, more energy is required to extend the crack after the onset of crack growth, due to the energy dissipation in the plastic zone at the crack tip (Anderson, 2005); that is, the fracture toughness increases as the crack grows. The relationship between the fracture toughness and crack extension Δa under stable quasi-static growth conditions is defined as the fracture toughness resistance curve (Hutchinson, 1983; Anderson, 2005).

1.2.2 Elastic Plastic Fracture Mechanics

Linear elastic fracture mechanics (LEFM) is invalid when the fracture processes are accompanied by significant plastic deformation at the crack tip (Anderson, 2005). As a rough approximation, the application of LEFM becomes questionable if the applied load is greater than one half of the load at which full plastic yielding occurs (Hutchison, 1983). To characterize the fracture behavior of ductile materials with medium-to-high toughness, the elastic plastic fracture mechanics is required.

Before further discussions of the elastic plastic fracture mechanics, it is necessary to introduce some fundamentals of the theory of plasticity. There are two main theories of plasticity based on two different constitutive relations. The incremental (or flow) theory of plasticity employs the formulations relating increments of stress and strain, whereas the deformation theory of plasticity employs the formulations relating the total stress and strain. The incremental theory of plasticity is loading-path-dependent, whereas the deformation theory of plasticity is loading-path-independent. Under the monotonic and proportional loading condition, the deformation theory of plasticity is equivalent to the incremental theory of plasticity.

The *J*-integral proposed by Rice (1968) is perhaps the most important concept in EPFM (Anderson, 2005). Consider a two-dimensional cracked body (see Fig. 1.3) characterized by the deformation theory of plasticity (i.e. small strain kinematics and nonlinear elastic constitutive model) with an arbitrary counterclockwise path (Γ) around the crack tip. The *J*-integral or *J* is defined as

$$J = \int_{\Gamma} \left(w dy - T_i \cdot \frac{\partial u_i}{\partial x} ds \right) \tag{1.4}$$

where u_i and T_i are components of the displacement and traction vectors, respectively (i = 1, 2 or 3); w is the strain energy density, and ds is the length increment along the contour Γ. Note that the unit of J is energy/area or equivalently force/length. The strain energy density w and traction T_i are given by (Anderson, 2005):

$$w = w(x, y) = w(\varepsilon_{ij}) = \int_0^{\varepsilon_{ij}} \sigma_{ij} d\varepsilon_{ij} \tag{1.5}$$

$$T_i = \sigma_{ij} n_j \tag{1.6}$$

where ε_{ij} (i, j = 1, 2, or 3) is the strain tensor, and n_j is the component of the unit normal vector to Γ. Rice (1968) showed that the value of J is independent of the integration path, i.e. Γ, around the crack tip. Therefore, J is a path-independent integral. It can be further shown (Rice, 1968; Anderson, 2005) that J is also equal to the energy release rate for the nonlinear elastic cracked body, and reduces to G for a linear elastic cracked body.

Similar to K, J is also an intensity parameter characterizing the stress state near the crack tip (Anderson, 2005). Consider a two-dimensional (i.e. plane-strain or plane-stress) cracked body characterized by the deformation plasticity and a Ramberg-Osgood stress-strain relationship as follows:

$$\frac{\varepsilon}{\varepsilon_0} = \frac{\sigma}{\sigma_0} + \alpha \left(\frac{\sigma}{\sigma_0} \right)^n \tag{1.7}$$

where σ_0 is the reference stress and typically set equal to the yield strength; $\varepsilon_0 = \sigma_0/E$, and α and n are parameters of the Ramberg-Osgood relationship with n commonly known as the strain hardening exponent. Hutchinson (1968) as well as Rice and Rosengren (1968) independently showed that at distances close to the crack tip, where the elastic strain is negligible compared with the plastic strain, the stresses and strains are related to J through the following equations:

$$\sigma_{ij} = \sigma_0 \left(\frac{J}{\alpha \sigma_0 \varepsilon_0 I_n r} \right)^{\frac{1}{n+1}} \tilde{\sigma}_{ij}(\theta, n) \tag{1.8}$$

$$\varepsilon_{ij} = \frac{\alpha\sigma_0}{E}\left(\frac{J}{\alpha\sigma_0\varepsilon_0 I_n r}\right)^{\frac{n}{n+1}} \tilde{\varepsilon}_{ij}(\theta, n) \tag{1.9}$$

where I_n is an integration constant that depends on n, and $\tilde{\sigma}_{ij}$ and $\tilde{\varepsilon}_{ij}$ are dimensionless functions of n, θ, and stress state (plane strain or plane stress). Equations (1.8) and (1.9) are known as the HRR solutions (singularity) (Anderson, 2005). Therefore, J provides a single-parameter characterization of the crack-tip fields in EPFM, just as K provides a single-parameter characterization of the crack-tip fields in LEFM.

Several important points about J and HRR solutions are worth emphasizing. First, the J-integral as originally proposed by Rice (1968) is applicable to two-dimensional (2D) configurations. Further research has extended the J concept to three-dimensional (3D) configurations (Anderson, 2005; Shih et al. 1986), where J is considered as a local value that varies along the crack front. However, J in a 3D configuration has no direct relationship with the near-tip stress and strain fields, but is simply a characterizing parameter that quantifies the severity of the crack-tip fields (Nikishkov and Atluri, 1987). Second, J is path-independent only for materials characterized by the deformation plasticity (i.e. nonlinear elastic). J is path-dependent for materials characterized by the incremental plasticity. However, as long as the loading is proportional everywhere in the cracked body (Anderson, 2005), the deformation plasticity is equivalent to the incremental plasticity. Finally, the HRR solutions are only applicable at locations near the crack tip, where the elastic strains are negligible and the singularity terms in Eqs. (1.8) and (1.9) dominate. At location immediately ahead of the crack tip, however, the HRR solutions are invalid because they do not account for the finite geometry change (i.e. large strain) at the crack tip (Anderson, 2005).

Because J is considered a characterizing parameter for the crack-tip fields, it is natural to experimentally determine the fracture toughness of the material as the critical value of J at the onset of crack growth, which is known as J_{Ic}. In addition, J can also be considered as an intensity measure even with a small amount of crack growth, as long as the conditions for the so-called J-controlled crack growth are satisfied (Hutchinson, 1983).

These conditions essentially limit the amount of crack growth such that the elastic unloading and nonproportional loading near the crack tip associated with the crack growth are well contained within the region where the deformation plasticity on which the *J*-integral is based is still applicable. Based on this argument, tests can be carried out to develop *J* versus (small amounts of) crack extension Δa for ductile material, known as the *J-R*esistance curve or *J-R* curve (Hutchinson, 1983; Anderson, 2005). The *J-R* curve is a generalization of the *K*-based resistance curve, as the latter is only applicable under the small scale yielding condition. For ductile materials, *J* always increases with small amounts of crack advance; therefore, the *J-R* curve has significant practical implications for structures that are made of ductile materials and can tolerate certain amount of crack growth, because significant additional load carrying capacity can be achieved with the application of the *J-R* curve. The *J-R* curve evaluation and the plastic geometry factor, which is key to the experimental evaluation of the *J*-integral, are investigated in the study reported in this thesis.

1.3 Objective and Research Significance

1.3.1 Investigation of Plastic Geometry Factors

The objective of the first study reported in this thesis was to carry out a systematic investigation of the plastic η factor for SE(B) specimens using three-dimensional (3D) finite element analyses (FEA). Both plane-sided and side-grooved SE(B) specimens with a wide range of the crack depth-over-specimen width ratios (*a/W*) and specimen thickness-over-width ratios (*B/W*) were analyzed. The load line displacement (*LLD*)- and crack mouth opening displacement (*CMOD*)-based η_{pl} corresponding to the average *J* value over the crack front as well as the local *J* at the mid-plane were evaluated. The impact of *a/W*, *B/W* and the strain hardening characteristics on the η factor were also investigated. The research outcome will improve the accuracy of the *J-R* curve obtained from the experiment and facilitate the evaluation of *J-R* curves using non-standard (e.g. shallow-cracked) SE(B) specimens.

1.3.2 Investigation of Constraint-corrected *J-R* Curve

The objective of the second study reported in this thesis was to develop constraint-corrected *J-R* curves for high-strength pipe steel (X80) based on experimentally determined *J-R* curves from SE(B) specimens and the corresponding constraint parameters determined from 3D FEA. Given the constraint-corrected *J-R* curve and level of the crack tip constraint for the real crack in pipelines, the fracture toughness resistance curves corresponding to the real structure can be developed. This will lead to more accurate, economic design and assessment of high-strength energy pipelines.

1.4 Thesis Outline

The thesis is presented as an integrated-article format and consists of four chapters. Chapter 1 is the introduction of the entire thesis where a review of fundamentals of LEFM and EPFM is presented, including the concepts of energy release rate, stress intensity factor, *J*-integral, and resistance curve. The main body of the thesis contains two chapters, Chapters 2 and 3. Each of these chapters is presented as a stand-alone manuscript without any abstract, but with its own references. In Chapter 2, a study of the plastic geometry factor based on 3D FEA is presented. Chapter 3 describes the development of constraint-corrected *J-R* curves. Finally, a summary of the study, main conclusions of the thesis and recommendations for future study are included in Chapter 4.

References

Anderson TL. *Fracture Mechanics—Fundamentals and Applications*, Third edition. CRC Press, Boca Raton; 2005.

ASTM. *ASTM E1820-11E2*: *Standard Test Method for Measurement of Fracture Toughness*, ASTM, West Conshohocken, PA; 2013.

ASTM. *ASTM E399-12E1*: *Standard Test Method for Linear-Elastic Plane-Strain Fracture Toughness K_{Ic} of Metallic Materials*, ASTM, West Conshohocken, PA; 2013.

Broek D. *Elementary Engineering Fracture Mechanics*, Fourth edition. Kluwer Academic Publishers, Dordrecht, The Netherlands; 1986.

BSI. *BS 7448: Fracture Mechanics Toughness Tests*, British Standard Institution, London; 1997.

Dodds RH, Ruggieri C, Koppenhoefer K. 3-D Constraint Effects on Models for Transferability of Cleavage Fracture Toughness. *ASTM Special Technical Publication*; 1997;1321:179-97.

Hutchinson JW. Singular Behavior at the End of a Tensile Crack in a Hardening Material. *Journal of the Mechanics of Physics and Solids*; 1968;16:13-31.

Hutchinson JW. Fundamentals of the Phenomenological Theory of Nonlinear Fracture Mechanics. *Journal of Applied Mechanics*; 1983;50:1042-51.

Irwin GR. Analysis of Stresses and Strains Near the End of a Crack Traversing a Plate; *Journal of Applied Mechanics*; 1957;24:361-4.

National Energy Board (NEB). Annual Report 2010 to Parliament, National Energy Board, Canada; 2010.

Nikishkov GP, Atluri SN. Calculation of Fracture Mechanics Parameters for an Arbitrary Three-dimensional Crack, by the 'Equivalent Domain Integral' Method. *International Journal for Numerical Methods in Engineering*; 1987;24(9):1801-21.

O'Dowd NP, Shih CF. Family of Crack-tip Fields Characterized by a Triaxiality Parameter—I. Structure of Fields. *Journal of the Mechanics and Physics of Solids*; 1991;39(8):989-1015.

PHMSA. Pipeline Incidents and Mileage Reports, March 2012. Pipeline & Hazardous Materials Safety Administration; 2012; http://primis.phmsa.dot.gov/comm/reports/safety/PSI.html.

Rice JR. A Path Independent Integral and the Approximate Analysis of Strain Concentration by Notches and Cracks. *Journal of Applied Mechanics*; 1968;35:379-86.

Rice JR, Rosengren GF. Plane Strain Deformation Near a Crack Tip in a Power Law Hardening Material. *Journal of the Mechanics of Physics and Solids*, 1968;16:1-12.

Shih CF, Moran B, Nakamura T. Energy Release Rate Along a Three-dimensional Crack Front in a Thermally Stressed Body. *International Journal of Fracture*; 1986;30:79-102.

Williams ML. On the Stress Distribution at the Base of a Stationary Crack. *Journal of Applied Mechanics*; 1957;24:109-14.

Yuan H, Brocks W. Quantification of Constraint Effects in Elastic-plastic Crack Front Fields. *Journal of the Mechanics and Physics of Solids*; 1998;46(2):219-41.

Yang S, Chao YJ, Sutton MA. Complete Theoretical Analysis for Higher Order Asymptotic Terms and the HRR Zone at a Crack Tip for Mode I and Mode II Loading of a Hardening Material. *Acta Mechanica*; 1993a;98:79-98.

Yang S, Chao YJ, Sutton MA. Higher-order Asymptotic Fields in a Power-law Hardening Material. *Engineering Fracture Mechanics*; 1993b;45:1-20.

Zhu XK, Jang SK, *J-R* Curves Corrected by Load-Independent Constraint Parameter in Ductile Crack Growth. *Engineering Fracture Mechanics*; 2001;68:285-301.

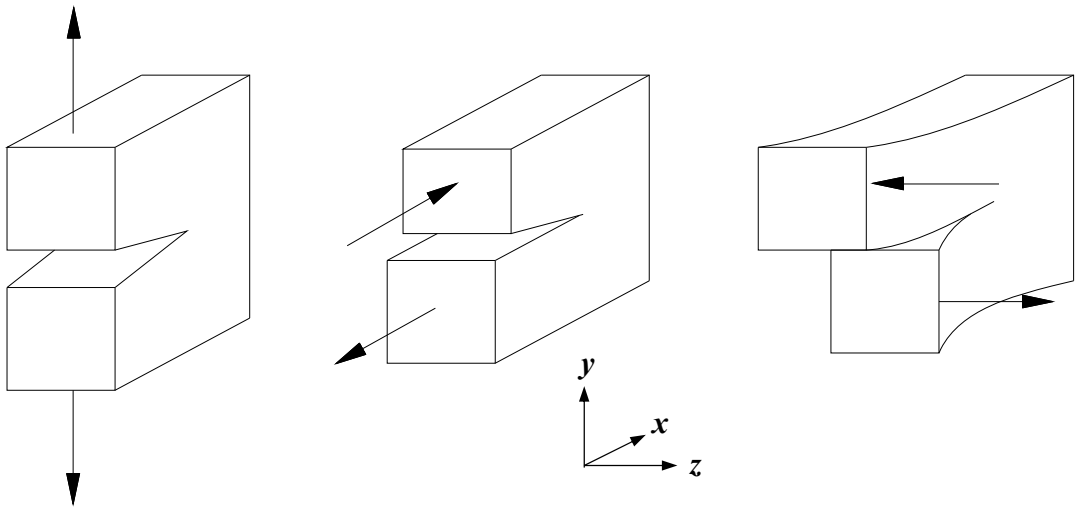

(a) Mode I: opening mode **(b) Mode II: in-plane shearing mode** **(c) Mode III: out-of-plane shearing mode**

Figure 1.1: Three typical loading modes in fracture mechanics

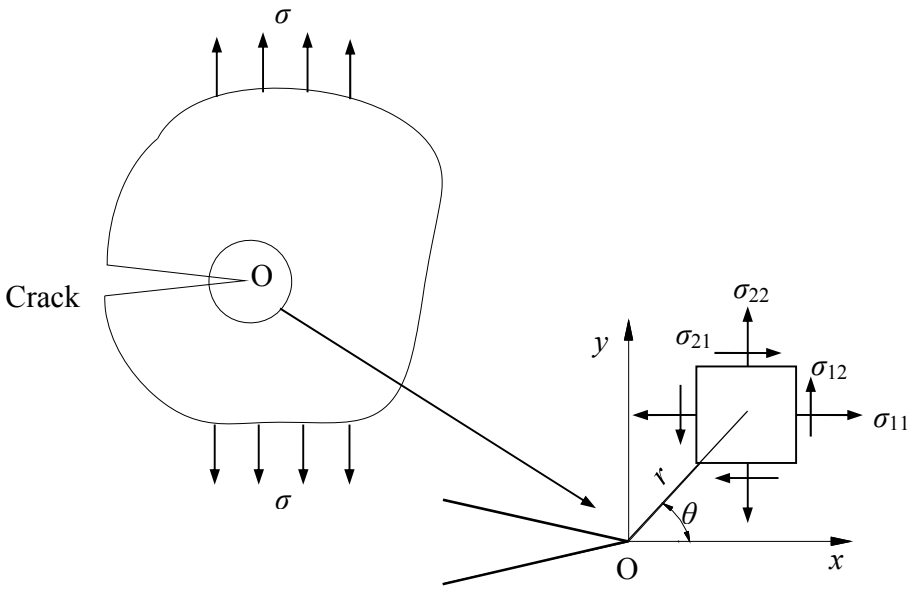

Figure 1.2: Stress field near the crack tip

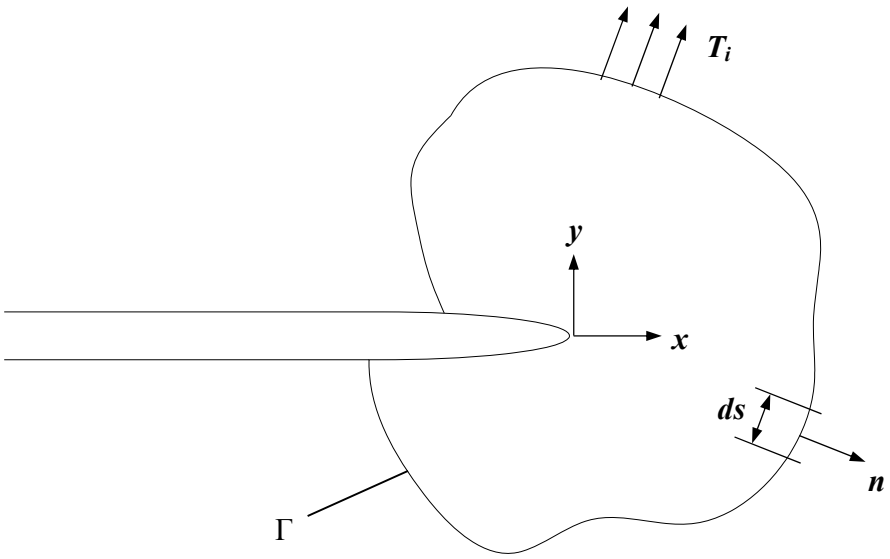

Figure 1.3: Schematic of *J*-integral

Chapter 2 Evaluation of Plastic η Factors for SE(B) Specimens Based on Three-dimensional Finite Element Analysis

2.1 Background and Objective

2.1.1 *J-R* Curve on Small-scale Specimens

The fracture toughness resistance curve, i.e. *J-R* or *CTOD-R* curve, is widely used in the integrity assessment and strain-based design of energy pipelines with respect to planar defects (i.e. cracks), where *J* and *CTOD* denote the *J*-integral and crack-tip opening displacement, respectively. There are two main components of a *J-R* curve, namely the crack growth, Δa, and the *J* value corresponding to this particular crack growth. Evaluation of the *J* value in the *J-R* curve based on plastic geometry factors is detailed in Section 2.1.2. The elastic unloading compliance method (Clarke et al., 1976) that is commonly used in the experimental evaluation of Δa in the *J-R* curve test is detailed in Appendix B. This section briefly describes the standardized specimens for the *J-R* curve test.

The *J-R* curve tests are commonly conducted on small-scale specimens such as the single-edge bend (SE(B)) and compact tension (C(T)) specimens, which are specified in standards such as ASTM E1820-11E2 (ASTM, 2013) and BS7448-97 (BSI, 1997). The evaluation of the load versus load line displacement (*P-LLD*) curve or load versus crack mouth opening displacement (*P-CMOD*) curve is key to the experimental evaluation of the *J-R* curve based on these specimens. Figure 2.1 shows a schematic of the plane-sided and side-grooved SE(B) and C(T) specimens as well as the corresponding *LLD* and *CMOD*, where dimensions B, B_N, S, W and a denote the specimen thickness, net thickness, specimen span, width and crack length, respectively. Note that the side-grooved specimen is often used in the *J-R* curve test to promote a straight crack front during the crack growth process (Anderson, 2005). The use of side-grooved SE(B) and C(T) specimens has been standardized; for example, ASTM E1820-11E2 specifies the side groove depth to be 10%B on each side of the SE(B) specimen and the angle between the

face of the side groove and the plane perpendicular to the side surface of the specimen to be less than 45 degrees.

2.1.2 Estimation of *J* Using Plastic Geometry Factors

Begley and Landes (1972) were among the first to evaluate *J* experimentally based on its interpretation as the energy release rate:

$$J = -\frac{dU}{Bda} \tag{2.1}$$

where *U* denotes the strain energy. This method requires testing multiple specimens with different crack lengths, which can be costly and time consuming. Subsequent work by Rice et al. (1973) introduced a more convenient way to evaluate *J* from a single test specimen. *J* can be evaluated in either the load controlled (Eq. 2.2) or displacement controlled (Eq. 2.3) condition as follows (see Figure 2.2):

$$J = \frac{1}{B}\int_0^P \frac{\partial \Delta}{\partial a} dP \tag{2.2}$$

or

$$J = -\frac{1}{B}\int_0^\Delta \frac{\partial P}{\partial a} d\Delta \tag{2.3}$$

where *P* denotes the applied load; Δ is the load-line displacement (*LLD*), and *U* is defined as the area under the load-displacement curve in Fig. 2.2. Based on the limit load analysis, Sumpter and Turner (1976) proposed an alternative form of Eq. (2.3):

$$J = \frac{\eta_{LLD}}{bB}\int_0^\Delta P d\Delta = \frac{\eta_{LLD} A_{LLD}}{bB} \tag{2.4}$$

where b is the length of the uncracked ligament, i.e. $b = W - a$; η_{LLD} is a dimensionless geometry factor relates J and the strain energy, and A_{LLD} represents the area under the load versus LLD curve. Figure 2.3 shows a typical load vs. displacement curve in the fracture toughness test. The total area under the loading path, A, is defined as the work done by external force during the test. As indicated in Fig. 2.3, A can be separated by an elastic unloading path into an elastic component, A_{el}, and a plastic component, A_{pl}, i.e. $A = A_{el} + A_{pl}$. Similarly, this unloading path separates Δ into an elastic component, Δ_{el}, and a plastic component, Δ_{pl}, i.e. $\Delta = \Delta_{el} + \Delta_{pl}$, and Eq. (2.3) can be accordingly rewritten as

$$J = -\frac{1}{B}\int_0^{\Delta_{el}} \frac{\partial P}{\partial a} d\Delta_{el} - \frac{1}{B}\int_0^{\Delta_{pl}} \frac{\partial P}{\partial a} d\Delta_{pl} = J_{el} + J_{pl} \tag{2.5}$$

where J_{el} and J_{pl} are the elastic and plastic components of J, respectively. J_{el} can be determined from the stress intensity factor K (Anderson, 2005):

$$J_{el} = \frac{K^2(1-\nu^2)}{E} \tag{2.6}$$

where E and ν are Young's modulus and Poisson's ratio respectively. Sumpter and Turner (1976) proposed the following equation to compute J_{pl}:

$$J_{pl} = \frac{\eta_{pl}^{LLD}}{bB}\int_0^{\Delta_{pl}} P d\Delta_{pl} = \frac{\eta_{pl}^{LLD} A_{pl}^{LLD}}{bB} \tag{2.7}$$

where η_{pl}^{LLD} and A_{pl}^{LLD} denote the plastic geometry factor and plastic area under the load versus load line displacement respectively. Alternatively, J can be evaluated from the crack mouth opening displacement ($CMOD$ or V) as opposed to LLD (Kirk and Dodds, 1993); therefore,

$$J_{pl} = \frac{\eta_{pl}^{CMOD}}{bB}\int_0^{V_{pl}} P dV_{pl} = \frac{\eta_{pl}^{CMOD} A_{pl}^{CMOD}}{bB} \tag{2.8}$$

where A_{pl}^{CMOD} represents the plastic area under the load versus *CMOD* curve, and η_{pl}^{CMOD} denotes the *CMOD*-based plastic geometry factor.

Equations (2.1) through (2.8) are limited to stationary cracks. The crack growth correction should be considered in the evaluation of *J* for growing cracks. Based on the deformation theory of plasticity, *J* is independent of the load path leading to the current *LLD* (or *CMOD*) and crack length *a*, given that the *J*-controlled crack growth conditions are satisfied (Sumpter and Turner, 1976). Accordingly, *J* is a function of two independent variables, *a* and Δ. Ernst et al. (1981) developed an incremental method to estimate *J* for growing cracks by deriving the total differential of J_{pl} as

$$dJ_{pl} = \frac{\eta_{pl} P}{bB} d\Delta_{pl} - \frac{\gamma}{b} J_{pl} da \tag{2.9}$$

with

$$\gamma = \left(\eta_{pl} - 1 - \frac{b}{W} \frac{1}{\eta_{pl}} \frac{\partial \eta_{pl}}{\partial (a/W)} \right) \tag{2.10}$$

Integrating both sides of Eq. (2.9) yields

$$J_{pl} = \int_0^{\Delta_{pl}} \frac{\eta_{pl} P}{bB} d\Delta_{pl} - \int_{a_0}^{a} \frac{\gamma}{b} J_{pl} da \tag{2.11}$$

where a_0 is the initial crack length. Equation (2.11) can be applied to any loading path leading to the current values of Δ_{pl} and *a*. Figure 2.4 shows a schematic of the estimation of J_{pl} for growing cracks. The figure includes a typical P-Δ_{pl} curve for a growing crack, and three deformation paths for the initial crack length, a_0, and two arbitrary crack lengths a_i and a_{i+1} respectively. The actual loading path AC in the figure can be replaced by the fictitious loading paths AB and BC. Integrating both sides of Eq. (2.9) along the loading path AB results in

$$J_{pl}^{B} = J_{pl}^{i} + \frac{\eta_{pl}^{i}}{b_i B} A_{pl}^{i,i+1} \tag{2.12}$$

where J_{pl}^{i} is the value of J_{pl} at A or step i; J_{pl}^{B} is the value of J_{pl} at B or the intermediate value of J_{pl} between step i and step i+1; $b_i = W - a_i$, and $A_{pl}^{i,i+1}$ equals the area of AB$\Delta_{pl}^{i}\Delta_{pl}^{i+1}$ but can be adequately approximated by the area under the actual loading path between Δ_{pl}^{i} and Δ_{pl}^{i+1} (i.e. the shaded area in Fig. 2.4), if $\Delta_{pl}^{i+1} - \Delta_{pl}^{i}$ is sufficiently small; $A_{pl}^{i,i+1}$ can be evaluated using the trapezoidal rule as $A_{pl}^{i,i+1} \cong \frac{1}{2}(P^{i} + P^{i+1})(\Delta_{pl}^{i+1} - \Delta_{pl}^{i})$. Integrating both sides of Eq. (2.9) again along the loading path BC results in

$$J_{pl}^{i+1} = J_{pl}^{B}\left[1 - \frac{\gamma_i}{b_i}\left(a_{i+1} - a_i\right)\right] \tag{2.13}$$

where J_{pl}^{i+1} is the value of J_{pl} at C or step i+1. Combining Eqs. (2.12) and (2.13) leads to the following general incremental expression for calculating J_{pl}:

$$J_{pl}^{i+1} = \left(J_{pl}^{i} + \frac{\eta_{pl}^{i}}{b_i B} A_{pl}^{i,i+1}\right)\left[1 - \frac{\gamma_i}{b_i}\left(a_{i+1} - a_i\right)\right] \tag{2.14}$$

Equation (2.14) is adopted by ASTM E1820-11E2 (ASTM, 2013) as the main procedure to experimentally evaluate the *J-R* curve. The crack length corresponding to each loading step can be determined using the unloading compliance method, which is described in Appendix B. Parameters η_{pl} and γ are called plastic geometry factors serving as key parameters to the experimental evaluation of the *J*-integral. The evaluation of the η_{pl} factors for the SE(B) specimens is the focus of the study reported in this chapter.

2.1.3 Literature Review of Studies on the Plastic Geometry Factors

Early studies (Begley and Landes, 1972; Rice et al., 1973) showed that the *J*-integral, interpreted as a nonlinear energy release rate, is related to the area under the *P-LLD* curve. The total *J*-integral can be separated into the elastic component J_{el} and the plastic component J_{pl}. It is straightforward to evaluate J_{el} based on the linear elastic stress intensity factor, the solution of which is well documented (e.g. Tada et al., 2000). Sumpter and Turner (1976) proposed the dimensionless plastic η factor (η_{pl}) to evaluate J_{pl} by relating J_{pl} to the plastic work that can be computed from the *P-LLD* or *P-CMOD* curve. At the limit load, the η factor is only a function of the configuration of the cracked body and independent of the loading (Kanninen and Popelar, 1985).

Due to its simplicity, the η_{pl}–based evaluation of *J*-integral is widely used and adopted in standards such as ASTM E1820-11E2 and BS7448-97. It follows that accurate η_{pl} factors are needed to ensure the accuracy of the experimentally-evaluated *J*. Wu et al. (1990) applied the slip line field solution to derive the analytic solution of η_{pl} factors. Sharobeam and Landes (1991) adopted the load separation analysis proposed by Paris et al. (1980) to develop an experimental procedure to determine η_{pl} factors. Based on the two-dimensional (2D) plane-strain finite element analysis (FEA), both *LLD*- and *CMOD*-based η_{pl} have been developed for the standard deeply-cracked (i.e. the relative crack length *a/W* greater than or equal to 0.45) SE(B) and C(T) specimen. For example, Kirk and Dodds (1993) and Donato and Ruggieri (2006) carried out 2D plane-strain FEA on SE(B) specimens to evaluate both *LLD*- and *CMOD*-based η_{pl} whereas the estimation of *LLD*- and *CMOD*-based η_{pl} for C(T) specimens was included in the study by Kim and Schwalbe (2001). The *LLD*-based η_{pl} is reported (Wu et al., 1990; Kim and Schwalbe, 2001) to be independent of *a/W* for deeply-cracked SE(B) and C(T), and the *CMOD*-based η_{pl} is found to be less dependent on the strain hardening exponent *n* than *LLD*-based η_{pl} for shallow-cracked SE(B) (Kirk and Dodds, 1993; Kim and Schwalbe, 2001; Donato and Ruggieri, 2006). Note that using the *P-CMOD* curve to evaluate *J* is more advantageous than using the *P-LLD* curve because *CMOD* can be more accurately and easily measured than *LLD* (Zhu et al., 2008).

It is well known that the *J-R* curve is dependent on the crack tip constraint (Yuan and Brocks, 1998). Recent studies on η_{pl} (e.g. Shen and Tyson, 2009; Petti et al., 2009) have focused on non-standard specimens with low levels of constraint including the single-edge tension (SE(T)) and shallow-cracked SE(B) specimens. Both *LLD*- and *CMOD*-based η_{pl} are observed to be a function of *a/W* for shallow-cracked SE(B) and SE(T) specimens (Kirk and Dodds, 1993; Link and Joyce, 1995; Cravero and Ruggieri, 2007).

With the rapid advancement of modern computers, three-dimensional (3D) FEA are being increasingly used to evaluate η_{pl}. Nevalainen and Dodds (1995) obtained values of η_{pl} for the SE(B) and C(T) specimens based on 3D FEA. Kim et al. (2004) evaluated η_{pl} for plane-sided SE(B), SE(T) and C(T) specimen using 3D FEA. In these studies, η_{pl} corresponding to both the average and maximum *J* values over the crack front, i.e. η_{ave} and η_{max}, were evaluated. In the study by Nikishkov et al. (1999), 3D SE(B) and C(T) specimens with curved crack fronts were analyzed to evaluate η_{pl} corresponding to the local *J* value at the mid-thickness of the crack front, η_{mid}. Work done by Kulka and Sherry (2012) was focused on the *LLD*-based η_{ave} for C(T) specimens with various *a/W* ratios and thickness-to-width (*B/W*) ratios. In the study by Ruggieri (2012), 3D FEA was carried out to evaluate η_{pl} for plane-sided SE(T) specimens with a wide range of *a/W* ratios (0.3 to 0.7) and two different specimens thicknesses. The η factors for side-grooved SE(B) and C(T) models with specific *a/W* ratios and *B/W* ratios have also been reported in the literature (Nikishkov et al., 1999; Nevalainen and Dodds, 1995).

2.1.4 Objective and Approach

Several observations of the previous studies on η_{pl} are in order. First, η_{pl} determined from 2D FEA may not be adequate given that the real specimens and cracks are three-dimensional. Second, although η_{pl} determined from 3D FEA has been reported in the literature, there is a lack of systematic investigations of η_{pl} that take into account the impact of *a/W*, *B/W*, side-grooves and strain hardening characteristics on η_{pl}. Finally, all of the 3D FEA reported in the literature are based on the small-strain formulation. The use of the small-strain analysis neglects the effect of crack-tip blunting along the crack

front (Dodds et al., 1990). For shallow-cracked specimens where the crack tip is near the crack month at which *CMOD* is measured, it is expected that using the large-strain analysis may lead to more accurate simulation and values of η_{pl}. To the best knowledge of the author of this thesis, the use of the large-strain 3D FEA to evaluate η_{pl} has not been explored in the literature.

Motivated by these observations, a systematic investigation of η_{pl} for SE(B) specimens using the large-displacement large-strain 3D FEA was carried out in this study. Both plane-sided and side-grooved SE(B) specimens with a wide range of *a/W* and *B/W* ratios were analyzed. The *LLD*- and *CMOD*-based η_{pl} corresponding to the average *J* value over the crack front as well as the local *J* at the mid-plane were evaluated. The impact of *a/W*, *B/W* and the strain hardening characteristics on the η factor was also investigated. The research outcome will improve the accuracy of the *J-R* curve obtained from the experiment and facilitate the evaluation of *J-R* curves using non-standard (e.g. shallow-cracked) SE(B) specimens.

The organization of this chapter is as follows. Section 2.2 describes the finite element analysis involved in the present study. The evaluation procedure of plastic η factor is presented in Section 2.3, accompanied by the analysis results and comparison with those reported in the literature. The conclusions of this chapter are summarized in Section 2.4.

2.2 Finite Element Analysis

2.2.1 Material Model

Evaluation of η_{pl} requires computation of *J* and the load-displacement response involving the plastic work effect. In the FEA carried out in this study, an elastic-plastic constitutive model based on the incremental theory of plasticity and large-displacement large-strain formulation (Anderson, 2005) was adopted. The commercial software ADINA 8.7.4 (ADINA, 2012) was used to carry out the FEA. The large-strain analysis employs the finite strain tensor, whereas the small-strain analysis employs the infinitesimal strain tensor and neglects the second and higher order terms of the displacement gradients

(Mase, 1970). The use of the small-displacement formulation basically ignores the difference between the spatial and material coordinate systems, whereas the large-displacement formulation takes this difference into account and the Lagrangian coordinate system was selected in this study (ADINA, 2012). In ADINA, the large-displacement large-strain formulation requires input of the Cauchy (true) stress-logarithmic (true) strain and outputs the Cauchy stress and deformation gradient. The von Mises yield criterion and isotropic hardening rule were adopted in the analysis. The von Mises yield criterion states that yielding starts once the second invariant of the deviatoric stress tensor, J_2, reaches a critical value (i.e. $\sigma_y^2/3$). The incremental theory of plasticity combined with the associate flow rule and von Mises yield criterion can be characterized by the following constitutive equation:

$$d\varepsilon_{ij}^{pl} = d\lambda \cdot s_{ij} \tag{2.15}$$

where ε_{ij}^{pl} and s_{ij} are the plastic strain tensor and the deviatoric stress tensor, respectively, and $d\lambda$ is a scalar factor of proportionality.

The Ramberg-Osgood stress-strain relationship as given by Eq. (1.7) was employed. In this study, materials with σ_0 = 550 MPa, E = 200 GPa, ν = 0.3 and α = 1 were selected to simulate the X80 (API, 2012) grade pipeline steel. Three values of the strain hardening exponent, namely n = 5, 10 and 15, were considered to investigate the effect of n on η_{pl}. Note that the cases with n = 10 were considered as the baseline cases, as n = 10 is representative of the strain hardening characteristics of the X80 pipeline steels.

2.2.2 Finite Element Model

The geometric configuration of a typical SE(B) specimen in the FEA is shown in Fig. 2.5 together with the fixation and loading conditions. All the specimens included in this study have a width (W) of 20 mm and a span (S) of $4W$. For the baseline cases (i.e. n = 10) and the sensitivity cases with n = 5, three specimen thicknesses (B) (i.e. B/W = 0.5, 1 and 2), and six crack lengths (a/W) (i.e. a/W = 0.3 to 0.7 with an increment of 0.1) were

considered. Both plane-sided (PS) and side-grooved (SG) specimens were modeled. For the latter, the side groove was modeled as a sharp V-notch of 45 degrees with a depth of 10%B on each side of the specimen, which is consistent with the recommendations in ASTM E1820-11E2 (ASTM, 2013). A side-grooved model with a/W = 0.5 and B/W = 0.5 is schematically shown in Fig. 2.6. For the sensitivity cases with n = 15, only plane-sided specimens with three crack lengths (i.e. a/W = 0.3, 0.5 and 0.7) and B/W = 0.5 were investigated. Due to symmetry, only a quarter of a given specimen was modeled in the FEA. The 8-node 3D brick elements with 2×2×2 integration were used; the accuracy of using such element to calculate J for SE(B) specimens has been shown to be adequate (Kulka and Sherry, 2012).

A blunt crack tip with a radius r_w = 0.003 mm (see Fig. 2.5) was modeled to facilitate the large-deformation calculation (Graba, 2007). Note that for the side-grooved specimens, the blunt crack tip is also prepared through the thickness of the side grooves as shown in Fig. 2.6 to mitigate the impact of the singularity caused by the sharp V-notch under tension on the finite strain analysis. A spider-web mesh around the crack tip was established with 40 concentric semicircles (i.e. rings) surrounding the crack tip. The in-plane size of the elements closest to the crack tip is around 0.003 mm, and about 1/100 of the in-plane size of the elements in the outermost ring. The aspect ratio of these elements is set to be less than 10. The model was divided into 8 and 15 layers along the thickness direction for PS and SG specimens, respectively. The mesh density increases from the mid plane to the free surface to capture the high stress gradients near the free surface. A sensitivity study of the meshing was carried out, and the results indicated that further increasing the number of layers along the thickness has little impact on the calculation of both the local J value at the midpoint of the crack front, J_{mid}, and the average J value over the entire crack front, J_{ave}. The total number of elements is approximately 15,000 in a typical plane-sided specimen, and 21,000 in a typical side-grooved specimen. Two contact rollers were defined to simulate the rollers supporting and loading the specimen. The elastic modulus of the contact element was set as ten times that of the specimen. Rigid links were created to connect the loading point and the roller surface. Using contact rollers in the FEA can reflect the real test condition such as the sliding occurred between the specimen and the rollers as well as large deformation in the contact surface.

2.2.3 Computational Procedure

Displacement-controlled loading was applied in all the models. For models with $a/W \geq 0.4$, the displacement was increased from 0 to 1.5 mm through 5000 steps, whereas it was increased from 0 to 2 ~ 2.5 mm through 15,000 steps for models with $a/W = 0.3$. The sparse matrix solver was selected for its high efficiency in numerical analysis (ADINA, 2012). The full Newton-Raphson iteration method was adopted to find the solution of nonlinear equations with the maximum number of iterations for each step being 50. The displacement convergence criterion was selected, in which the displacement tolerance equaled 0.0001 corresponding to a reference displacement of 1 mm (ADINA, 2012). Figure 2.7 shows the distribution of the effective stress in a typical specimen (i.e. $a/W = 0.5$ and $B/W = 1$) corresponding to the applied displacement of 1.5mm. The shaded area denotes the extent of the plastic zone where the effective stress is greater than or equal to the yield strength (i.e. 550 MPa). The magnitude of the total strain in the element around the crack tip is about 1 - 10%. The *J*-integral was computed by using the virtual crack extension method implemented in ADINA (Anderson, 2005; ADINA, 2012). A brief description of this method is included in Appendix A. To ensure the path-independence of the calculated *J* values, the two outermost semicircular rings surrounding the crack tip were used to define the virtual shifts. Both J_{mid} and J_{ave} were calculated and used to evaluate the corresponding η_{pl} factors. By subtracting the elastic component of *J* from the total *J* as described in Eqs. (2.5) and (2.6), the plastic component of *J*, J_{pl}, can be computed. The *P-LLD* and *P-CMOD* curves were also output from the FEA so that the corresponding plastic work A_{pl} can be determined.

2.3 Determination of Plastic Geometry Factors for SE(B) Specimens

2.3.1 Evaluation Procedure of Plastic Geometry Factors

The η_{pl} factors can be computed at a given loading level (i.e. J value) using the following expression (Ruggieri, 2012):

$$\eta_{pl} = \frac{J_{pl} b B_N}{A_{pl}} = \frac{\left(\frac{J_{pl}}{b\sigma_0}\right)}{\left(\frac{A_{pl}}{b^2 B_N \sigma_0}\right)} = \frac{\bar{J}_{pl}}{\bar{A}_{pl}} \tag{2.16}$$

where B_N denotes the net thickness of the specimen, i.e. $B_N = B$ for the plane-sided specimen and $B_N = 0.8B$ for the side-grooved specimen with the side-groove depth equal to $0.1B$ at each side, and $\bar{J}_{pl}$ and $\bar{A}_{pl}$ are non-dimensionalized J and plastic area, respectively. Depending on the load-displacement curve (i.e. the *P-LLD* or *P-CMOD* curve) and J_{pl} value (i.e. J_{pl} evaluated from J_{mid} or J_{ave}) used in Eq. (2.16), four different η_{pl} factors can be evaluated, namely η_{mid}^{LLD}, η_{ave}^{LLD}, η_{mid}^{CMOD} and η_{ave}^{CMOD}, where the subscript "*pl*" is omitted to reduce clutter. Figure 2.8 shows the variation of η_{pl} with $\bar{J}_{pl}$ for a representative specimen (plane-sided, $a/W = 0.7$, $B/W = 1$ and $n = 10$). The figure suggests that η_{pl} is load-dependent for $P \leq 1.7P_l$, where P_l is the reference load and defined as $B_N b^2 \sigma_0 / S$ (Nevalainen and Dodds, 1995), and becomes approximately independent of the load for $P > 1.7P_l$. Figures 2.9(a) and 2.9(b) depict the relationships between $\bar{J}_{pl}$ and *CMOD*-based $\bar{A}_{pl}$ as well as between $\bar{J}_{pl}$ and *LLD*-based $\bar{A}_{pl}$ for four specimens (two plane-sided and two side-grooved) with $a/W = 0.3$ and 0.7 and $n = 10$. The η_{pl} factor can be evaluated as the slope of the linear fit of $\bar{J}_{pl}$ vs. $\bar{A}_{pl}$. Note that in a number of previous studies, η_{pl} for SE(B) specimens was evaluated by fitting the $\bar{J}_{pl}$ vs. $\bar{A}_{pl}$ data corresponding to high levels of applied load. For example, Kirk and Dodds (1993) calculated the slope of $\bar{J}_{pl}$ vs. $\bar{A}_{pl}$ by fitting data from the final three load steps in which the last load step corresponds to *CTOD* reaching 5% of the crack length; Donato and Ruggieri (2006) evaluated η_{pl} based on data within the range of $A_{pl} \geq 0.1(A_{pl} + A_{el})$ and

$\bar{J}_{pl} \leq 0.25$ (approximately equivalent to $1.1P_l \leq P \leq 2.5P_l$); Petti et al. (2009) evaluated η_{pl} by fitting data starting from $b\sigma_0/J_{ave} = 50$ (approximately equivalent to $P \geq 1.6P_l$). As such, evaluating η_{pl} at high loading levels minimizes the load-dependency of η_{pl} as indicated in Fig. 2.8.

In the present study, it is found that the range of the data used in the fitting has a non-negligible impact on the value of η_{pl}. For instance, η_{pl} determined based on data within the range of $1.0P_l \leq P \leq 1.7P_l$ is approximately 10% larger then that based on data within the range of $1.0P_l \leq P \leq 2.0P_l$ for deeply cracked (e.g. $a/W = 0.7$) specimens with $n = 5$. The *J-R* curve tests involving SE(B) specimens carried out in a previous study (Wang et al., 2012) indicate that the maximum loading level is typically less than $2.2P_l$ for materials with $n = 10$. On the other hand, because of the use of the large-strain formulation, the *J* value for shallow cracked specimens calculated in the present study was observed to be path-dependent once the loading level exceeds $1.7P_l$.

Based on these considerations, in this study, the η_{pl} factors for specimens with $a/W \geq 0.4$ were evaluated by linearly fitting the $\bar{J}_{pl}$ vs. $\bar{A}_{pl}$ data corresponding to $1.0P_l \leq P \leq 2.0P_l$. The η_{pl} factors for specimens with $a/W = 0.3$ were evaluated based on data within the range of $1.0P_l \leq P \leq 1.7P_l$.

2.3.2 Results and Discussions

Both *CMOD*- and *LLD*-based η_{pl} values corresponding to $n = 10$ are calculated and listed in Table 2.1. Figure 2.10 shows the calculated *CMOD*- and *LLD*-based η_{pl} values plotted against a/W for both PS and SG specimens with $n = 10$ and different B/W ratios. Figures. 2.10a and 2.10b indicate that the *LLD*-based η_{pl} generally increases with the a/W ratio, whereas Figs. 2.10c and 2.10d indicate that the *CMOD*-based η_{pl} generally decreases as a/W increases. From Figs. 2.10a and 2.10c, it can be seen that the B/W ratio has a significant impact on η_{mid}^{LLD} and η_{mid}^{CMOD}, which decrease as B/W increases. On the other hand, the B/W ratio has a relatively small impact on η_{ave}^{LLD} and η_{ave}^{CMOD} as shown in Figs. 2.10b and 2.10d: the largest difference between η_{ave}^{LLD} (η_{ave}^{CMOD}) corresponding to different

B/W ratios is approximately 9.5%. The values of η_{mid}^{LLD} and η_{mid}^{CMOD} for the SG models are generally 2-25% lower than those for the PS models with the same *a/W*, *B/W* and *n* values, whereas η_{ave}^{LLD} and η_{ave}^{CMOD} for the SG models are 1-6% higher than those for the corresponding PS models.

The η_{pl} values obtained in this study are compared with those reported by Nevalainen and Dodds (1995) (N&D, 1995) and Kim et al. (2004) in Fig. 2.10, which are obtained from 3D FEA using the small-strain formulation. Both studies are focused on the PS models; therefore, only the η_{pl} values corresponding to their PS models are shown for comparison. The η_{pl} values obtained in this study are generally lower than those reported by Kim et al. and Nevalainen and Dodds with the relative difference ranging from 4% to 11%. These differences may be due to the fact that the η_{pl} values obtained in this study are based on the large strain formulation adopted in the FEA.

Zhu et al. (2008) proposed the following expressions of *LLD*- and *CMOD*-based η_{pl} for SE(B) specimens by fitting the results from both 2D plane strain (PE) and 3D FEA with the small-strain formulation reported in the literature:

$$\eta_{pl}^{LLD} = 1.620 + 0.850\left(a/W\right) - 0.651\left(a/W\right)^2, \quad 0.25 \le a/W \le 0.7 \tag{2.17}$$

$$\eta_{pl}^{CMOD} = 3.667 - 2.199\left(a/W\right) + 0.437\left(a/W\right)^2, \quad 0.05 \le a/W \le 0.7 \tag{2.18}$$

It is worth pointing out that Eq. (2.18) has been adopted by ASTM E1820-11E2 (ASTM, 2013) for *CMOD*-based evaluation of *J* in the *J-R* curve test. As for *LLD*-based evaluation of *J,* ASTM E1820-11E2 suggests η_{pl}^{LLD} = 1.9 for deeply cracked (i.e. 0.45 ≤ *a/W* ≤ 0.7) specimens. The η_{mid}^{CMOD} values obtained in this study corresponding to the PS specimens with *a/W* ≥ 0.4 and *B/W* = 2 agree very well with Eq. (2.18). The η_{ave}^{LLD} values obtained in this study are generally lower than those evaluated from Eq. (2.17) as well as 1.9 as suggested in ASTM E1820-11E2, except for deeply cracked (*a/W* = 0.6 and 0.7) SG specimens; the η_{ave}^{CMOD} values obtained in this study corresponding to the PS and SG specimens with *a/W* ≥ 0.4 are generally lower and higher than those evaluated from Eq.

(2.18), respectively, and for both the PS and SG specimens with a/W = 0.3, the η_{ave}^{CMOD} values obtained in this study are somewhat higher than those from Eq. (2.18).

Both *CMOD*- and *LLD*-based η_{pl} values corresponding to n = 5 are calculated and listed in Table 2.2. Figure 2.11 shows the calculated *CMOD*- and *LLD*-based η_{pl} values plotted against the relative crack length a/W for both PS and SG specimens with n = 5 and different B/W ratios. The key observations of the η_{pl} vs. a/W relationship for n = 5 are similar to those for n = 10. The η_{mid}^{LLD} and η_{ave}^{LLD} values obtained in this study agree well with those from Kim et al. and N&D with the relative difference ranging from 2% to 5%. The η_{mid}^{CMOD} and η_{ave}^{CMOD}, values reported by Kim et al and N&D are generally 0.3% to 9% lower than those obtained in this study.

The impact of the strain hardening exponent on η_{pl} was investigated based on the values of η_{pl} for the PS specimens with a/W = 0.3, 0.5 and 0.7 and B/W = 0.5. The η_{pl} values corresponding to the three values of n, namely 5, 10 and 15, for the considered specimens are compared in Table 2.3. The results in Table 2.3 suggest that both *LLD*- and *CMOD*-based η_{pl} for specimens with B/W = 0.5 are insensitive to n for n = 10 and 15, and a/W = 0.5 and 0.7 as indicated in the last column of Table 2.3. On the other hand, for a/W = 0.3, the difference between the η_{pl} values corresponding to n = 10 and n = 15 is relatively large. For example, the values of η_{mid}^{CMOD} corresponding to n = 10 and n = 15 differ by 6.3% for a/W = 0.3, and the values of η_{ave}^{LLD} corresponding to n = 10 and n = 15 differ by 5.1% for a/W = 0.3. The results in Table 2.3 also indicate that values of η_{pl} are sensitive to n for $n \leq 10$ and a/W = 0.5 and 0.7. For example, the values of η_{mid}^{CMOD} corresponding to n = 5 and n = 10 differ by as much as 7.8% for a/W = 0.7.

2.4 Conclusions

A systematic investigation of the plastic η factor (η_{pl}) for both plane-sided and side-grooved SE(B) specimens based on the incremental-plasticity large-displacement/large-strain 3D FEA has been performed and is reported in this chapter. The *LLD*- and *CMOD*-based η_{pl} factors corresponding to the average J value over the crack front as well

as the local J value at the mid-plane were evaluated and tabulated. The impact of a/W, B/W, side-grooves and strain hardening characteristics on η_{pl} was investigated.

Three values of the strain hardening exponent, namely n = 5, 10 and 15, were considered to investigate the effect of n on η_{pl}. The cases with n = 10 were considered as the baseline cases. For cases with n = 5 and 10, both plane-sided and side-grooved specimens were studied considering three specimen thicknesses (B) (i.e. B/W = 0.5, 1 and 2), and six crack lengths (a/W) (i.e. a/W = 0.3 to 0.7 with an increment of 0.1). For cases with n = 15 materials, only $B\times 2B$ plane-sided specimens with three crack lengths (i.e. a/W = 0.3, 0.5, and 0.7) were investigated. The 8-node 3D brick elements with 2×2×2 integration were used. The displacement-controlled loading was applied in the FEA. A blunt crack tip with a radius r_w = 0.003 mm was modeled to facilitate the large-deformation calculation. Two contact rollers were defined to simulate the rollers supporting and loading the specimen. For materials with n = 5 and 10, the η_{pl} factors for specimens with $a/W \geq 0.4$ were evaluated by linearly fitting the $\bar{J}_{pl}$ vs. $\bar{A}_{pl}$ data corresponding to $1.0P_l \leq P \leq 2.0P_l$. The η_{pl} factors for specimens with a/W = 0.3 were evaluated based on data within the range of $1.0P_l \leq P \leq 1.7P_l$. For n =15 materials, η_{pl} was evaluated based on data within the range of $1.0P_l \leq P \leq 1.7P_l$ for specimens with $a/W \geq 0.4$, and $1.0P_l \leq P \leq 1.5P_l$ for specimens with $a/W = 0.3$.

For n = 10, it is observed that the B/W ratio and side-grooves have a greater impact on η_{mid} than on η_{ave}. Values of η_{mid} generally decrease with the increase of the B/W ratio. Except for the SG specimens with a/W = 0.6 and 0.7, the η_{ave}^{LLD} values obtained in this study are generally lower than 1.9 that is suggested in ASTM E1820-11E2 for SE(B) specimens with $0.45 \leq a/W \leq 0.7$; the η_{ave}^{CMOD} values obtained in this study corresponding to the PS and SG specimens with $a/W \geq 0.4$ are generally lower and higher than those evaluated from the equation suggested in ASTM E1820-11E2, respectively, and for both the PS and SG specimens with a/W = 0.3, the η_{ave}^{CMOD} values obtained in this study are somewhat higher than those evaluated from the ASTM E1820-11E2 equation. Both *LLD*- and *CMOD*-based η_{pl} for specimens with B/W = 0.5 are found to be insensitive to the strain hardening exponent n in the range of n = 10 to 15 and a/W = 0.5 and 0.7,

whereas the η_{pl} for the same specimens with B/W = 0.5 are found to be sensitive to n in the range n = 5 to 10.

The evaluation of the η_{pl} factor based on 3D FEA is a more realistic approach compared with the use of conventional 2D plane strain FEA, because the real specimens and cracks are three-dimensional. The results of the present study can potentially improve the accuracy of the *J*-*R* curve obtained from the experiment and facilitate the evaluation of *J*-*R* curves using non-standard (e.g. shallow-cracked) SE(B) specimens.

References

ADINA. *Theory and Modeling Guide*, ADINA R. & D. Inc., Watertown, USA; 2012.

Anderson TL. *Fracture Mechanics—Fundamentals and Applications*, Third edition. CRC Press, Boca Raton; 2005.

API. *API Specification 5L: Specification for Line Pipe*, Ed. 45, American Petroleum Institute, Washington, D.C.; 2012.

ASTM. *ASTM E1820-11E2*: *Standard Test Method for Measurement of Fracture Toughness*, ASTM, West Conshohocken, PA; 2013.

Begley JA, Landes JD. The *J*-integral as a Fracture Criterion. *Fracture Mechanics*, *ASTM STP 514*, ASTM International, West Conshohocken, PA; 1972;515:1-23.

BSI. *BS 7448: Fracture Mechanics Toughness Tests*, British Standard Institution, London; 1997.

Clarke GA, Andrews WR, Paris PC, Schmidt DW. Single Specimen Tests for J_{Ic} Determination. *Mechanics of Crack Growth, ASTM STP 590, American Society for Testing and Materials*, Philadelphia; 1976;27-42.

Cravero S, Ruggieri C. Estimation Procedure of *J-R*esistance Curves for SE(T) Fracture Specimens Using Unloading Compliance. *Engineering Fracture Mechanics*; 2007;74:2735-57.

Dodds RH, Read DT. Experimental and Numerical Studies of the *J*-integral for a Surface Flaw. *International Journal of Fracture*; 1990;43:47-67.

Donato GHB, Ruggieri C. Estimation Procedures for *J* and *CTOD* Fracture Parameters Using Three-Point Bend Specimens. *2006 International Pipeline Conference* (IPC2006) September 25–29th, 2006, Calgary, Alberta, Canada; 2006. p. IPC2006-10165.

Ernst HA, Paris PC, Landes JD. Estimations on *J*-integral and Tearing Modulus *T* from a Single Specimen Test Record, *Fracture Mechanics: Thirteenth Conference*, *ASTM STP 743*, American Society for Testing and Materials, 1981;476-502.

Graba M, Gałkiewicz J. Influence of the Crack Tip Model on Results of the Finite Elements Method. *Journal of Theoretical and Applied Mechanics*; 2007;45(2):225-37.

Huang Y, Zhou W, Wang E, Shen G. Evaluation of Plastic η Factors for SE(B) Specimens Based on Three-dimensional Finite Element Analysis. *Proc 23rd Int Offshore and Polar Eng Conf*, June 30 - July 5, Anchorage, ISOPE; 2013;591-7.

Kanninen MF, Popelar CH. *Advanced Fracture Mechanics*, Oxford University Press, New York; 1985.

Kim YJ, Kim JS, Cho SM, Kim YJ. 3-D Constraint Effects on *J* Testing and Crack Tip Constraint in M(T), SE(B), SE(T) and C(T) Specimens: Numerical Study. *Engineering Fracture Mechanics*; 2004;71:1203-18.

Kim YJ, Schwalbe KH. On the Sensitivity of *J* Estimation to Materials' Stress-strain Curves in Fracture Toughness Testing Using the Finite Element Method. *Journal of Testing and Evaluation*; 2001;29(1):18-30.

Kirk MT, Dodds RH. *J* and *CTOD* Estimation Equations for Shallow Cracks in Single Edge Notch Bend Specimens. *Journal of Testing and Evaluation*; 1993;21(4):228-38.

Kulka RS, Sherry AH. Fracture Toughness Evaluation in C(T) Specimens with Reduced Out-of-plane Constraint. *ASME 2012 Pressure Vessels & Piping Conference* (PVP-2012). July 15–19th, 2012, Toronto, Canada; 2012. p. PVP2012-78751.

Link RE, Joyce JA. Experimental Investigation of Fracture Toughness Scaling Models. *Constraint Effects in Fracture Theory and Applications*, *ASTM STP 1244*, ASTM, West Conshohocken, PA; 1995;2:286-315.

Mase GE. *Schaum's Outline of Continuum Mechanics*. McGraw-Hill; 1970.

Nevalainen M, Dodds RH. Numerical Investigation of 3-D Constraint Effects in Brittle Fracture in SE(B) and C(T) Specimens. *International Journal of Fracture*; 1995;74:131-61.

Nikishkov GP, Heerens J, Hellmann D. Effect of Crack Front Curvature and Side Grooving on *CTOD* δ_5 and *J*-integral in CT and 3PB Specimens. *Journal of Testing and Evaluation*; 1999;27(5):312-9.

Paris PC, Ernst H, Turner CE. A *J*-integral Approach to Development η-Factors. *Fracture Mechanics: twelfth conference, ASTM STP 700*, ASTM; 1980:338-51.

Petti JP, Dodds RH, Link RE. Crack Mouth Opening Displacement-based η Factors for SE(B) Specimens. *Journal of Testing and Evaluation*; 2009;37(4):383-6.

Rice JR, Paris PC, Merkle JG. Some Further Results of *J*-integral Analysis and Estimates. *Progress in flaws growth and fracture toughness testing*, *ASTM STP 536*. ASTM; 1973:231-45.

Ruggieri C. Further Results in *J* and *CTOD* Estimation Procedures for SE(T) Fracture Specimens – Part I: Homogeneous Materials. *Engineering Fracture Mechanics*; 2012;79:245-65.

Sharobeam M, Landes JD. The Load Separation Criterion and Methodology in Ductile Fracture Mechanics. *International Journal of Fracture*; 1991;41:81-104.

Shen G, Tyson WR. Crack Size Evaluation Using Unloading Compliance in Single-specimen Single-edge-notched Tension Fracture Toughness Testing. *Journal of Testing and Evaluation*; 2009;37(4):347-57.

Sumpter JDG, Turner CE. Method for Laboratory Determination of J_c (Contour Integral for Fracture Analysis). *Cracks and Fracture*, *ASTM STP 601*, ASTM, West Conshohocken, PA; 1976:3-18.

Tada H, Paris PC, Irwin GR. *The Stress Analysis of Cracks Handbook*, Third edition. ASME Press, New York; 2000.

Wang E, Zhou W, Shen G, Duan D. An Experimental Study on *J*(*CTOD*)-*R* Curves of Single Edge Tension Specimens for X80 Steel. *Proceedings of the 2012 9th International Pipeline Conference*, September 24-28, Calgary, Canada; 2012. p. IPC2012-90323.

Wu SX, Mai YW, Cotterell B. Plastic η-factor of Fracture Specimens with Deep and Shallow Cracks. *International Journal of Fracture*; 1990;45:1-18.

Yuan H, Brocks W. Quantification of Constraint Effects in Elastic-plastic Crack Front Fields. *Journal of the Mechanics and Physics of Solids*; 1998;46(2):219-41.

Zhu XK, Leis BN, Joyce JA. Experimental Estimation of *J-R* Curves From Load-*CMOD* Record for SE(B) Specimens. *Journal of ASTM International*; 2008;5:231-45.

Table 2.1a: The *LLD*-based η_{pl} obtained from varieties of 3D FE models for n = 10 materials

a/W	Plane-sided						Side-grooved					
	B/W						*B/W*					
	0.5		1		2		0.5		1		2	
	η_{mid}	η_{ave}	η_{mid}	η_{ave}	η_{mid}	η_{ave}	η_{mid}	η_{ave}	η_{mid}	η_{ave}	η_{mid}	η_{ave}
0.3	2.25	1.77	2.02	1.68	1.67	1.65	1.69	1.63	1.52	1.65	1.45	1.68
0.4	2.18	1.70	2.05	1.73	1.76	1.74	1.88	1.72	1.69	1.76	1.65	1.82
0.5	2.28	1.77	2.06	1.80	1.86	1.82	1.91	1.80	1.79	1.89	1.79	1.92
0.6	2.30	1.82	2.03	1.86	1.87	1.85	1.96	1.91	1.88	1.99	1.91	2.01
0.7	2.27	1.88	2.04	1.94	1.96	1.94	2.07	2.09	2.00	2.10	2.00	2.07

Table 2.2b: The *CMOD*-based η_{pl} obtained from varieties of 3D FE models for n = 10 materials

a/W	Plane-sided						Side-grooved					
	B/W						*B/W*					
	0.5		1		2		0.5		1		2	
	η_{mid}	η_{ave}	η_{mid}	η_{ave}	η_{mid}	η_{ave}	η_{mid}	η_{ave}	η_{mid}	η_{ave}	η_{mid}	η_{ave}
0.3	3.98	3.12	3.89	3.25	3.36	3.31	3.45	3.31	3.31	3.58	2.86	3.31
0.4	3.31	2.58	3.29	2.79	2.88	2.85	3.08	2.82	2.89	3.02	2.64	2.90
0.5	3.17	2.46	2.96	2.59	2.69	2.63	2.75	2.58	2.61	2.75	2.61	2.80
0.6	2.93	2.32	2.61	2.39	2.43	2.39	2.53	2.46	2.43	2.57	2.46	2.59
0.7	2.67	2.21	2.40	2.28	2.34	2.31	2.35	2.38	2.18	2.29	2.35	2.43

Table 2.3a: The *LLD*-based η_{pl} obtained from varieties of 3D FE models for n = 5 materials

a/W	Plane-sided						Side-grooved					
	B/W						*B/W*					
	0.5		1		2		0.5		1		2	
	η_{mid}	η_{ave}	η_{mid}	η_{ave}	η_{mid}	η_{ave}	η_{mid}	η_{ave}	η_{mid}	η_{ave}	η_{mid}	η_{ave}
0.3	2.18	1.73	1.98	1.67	1.65	1.62	1.76	1.71	1.61	1.73	1.54	1.77
0.4	2.34	1.83	2.14	1.81	1.87	1.81	1.87	1.74	1.84	1.88	1.64	1.80
0.5	2.35	1.84	2.13	1.84	1.91	1.85	1.87	1.76	1.90	1.97	1.77	1.90
0.6	2.36	1.87	2.12	1.89	1.91	1.85	1.98	1.89	1.92	2.03	1.88	1.98
0.7	2.37	1.96	2.13	1.97	1.95	1.89	1.95	1.94	1.97	2.08	1.94	2.01

Table 2.4b: The *CMOD*-based η_{pl} obtained from varieties of 3D FE models for n = 5 materials

a/W	Plane-sided						Side-grooved					
	B/W						*B/W*					
	0.5		1		2		0.5		1		2	
	η_{mid}	η_{ave}	η_{mid}	η_{ave}	η_{mid}	η_{ave}	η_{mid}	η_{ave}	η_{mid}	η_{ave}	η_{mid}	η_{ave}
0.3	4.15	3.30	3.97	3.35	3.44	3.38	3.45	3.37	3.30	3.54	3.14	3.61
0.4	3.78	2.96	3.53	2.98	3.15	3.05	2.91	2.71	2.92	2.98	2.78	3.06
0.5	3.44	2.69	3.11	2.69	2.81	2.72	2.68	2.51	2.71	2.81	2.59	2.78
0.6	3.11	2.47	2.76	2.46	2.50	2.42	2.54	2.43	2.48	2.62	2.39	2.52
0.7	2.90	2.40	2.53	2.33	2.32	2.24	2.24	2.23	2.31	2.43	2.25	2.33

Table 2.5: Variation of η_{pl} with strain hardening exponent for plane-sided model with $B/W = 0.5$

			$n = 5$ (I)	$n = 10$ (II)	$n = 15$[2] (III)	|II – I|/II (%)	|II – III|/II (%)
$a/W = 0.3$	*LLD*-based	η_{mid}	2.18	2.25	2.21	3.1	1.8
		η_{ave}	1.73	1.77	1.68	2.3	5.1
	CMOD-based	η_{mid}	4.15	3.98	4.23	4.3	6.3
		η_{ave}	3.30	3.12	3.21	5.8	2.9
$a/W = 0.5$	*LLD*-based	η_{mid}	2.35	2.35	2.33	0	0.9
		η_{ave}	1.84	1.80	1.77	2.2	1.7
	CMOD-based	η_{mid}	3.44	3.34	3.34	3.0	0
		η_{ave}	2.69	2.55	2.53	5.5	0.8
$a/W = 0.7$	*LLD*-based	η_{mid}	2.37	2.27	2.28	4.4	0.4
		η_{ave}	1.96	1.88	1.90	4.3	1.1
	CMOD-based	η_{mid}	2.90	2.69	2.70	7.8	0.4
		η_{ave}	2.40	2.23	2.25	7.6	0.9

[2] For n =15 materials, η_{pl} was evaluated based on data within the range of: (a) $1.0P_l \le P \le 1.7P_l$ for specimens with $a/W \ge 0.4$; (b) $1.0P_l \le P \le 1.5P_l$ for specimens with $a/W = 0.3$.

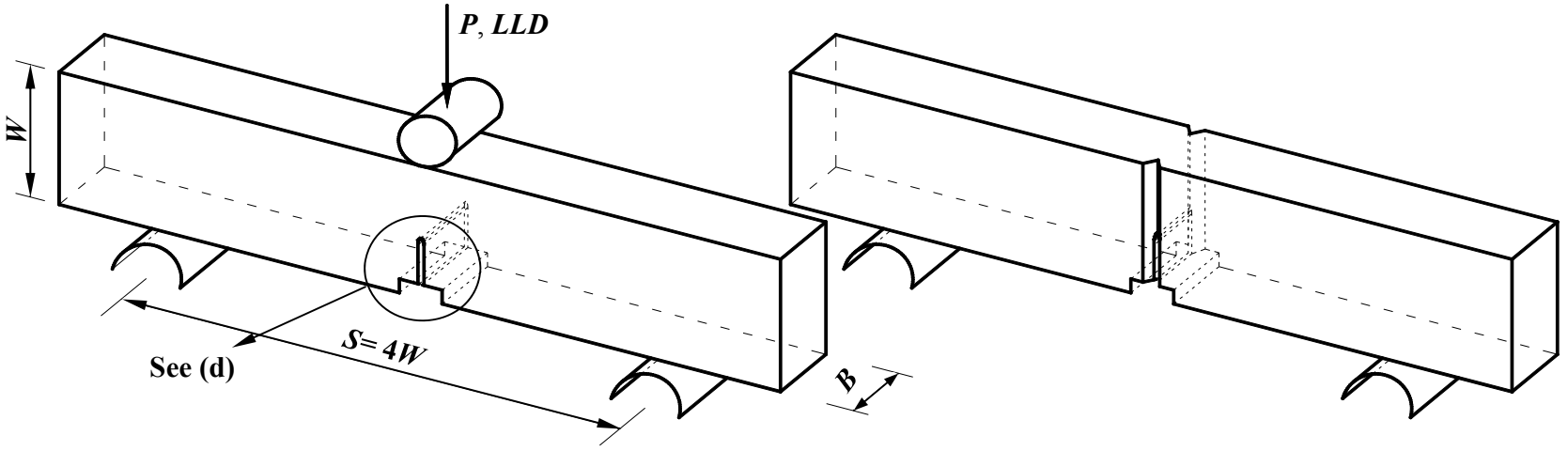

(a) PS (left) and SG (right) SE(B) specimens

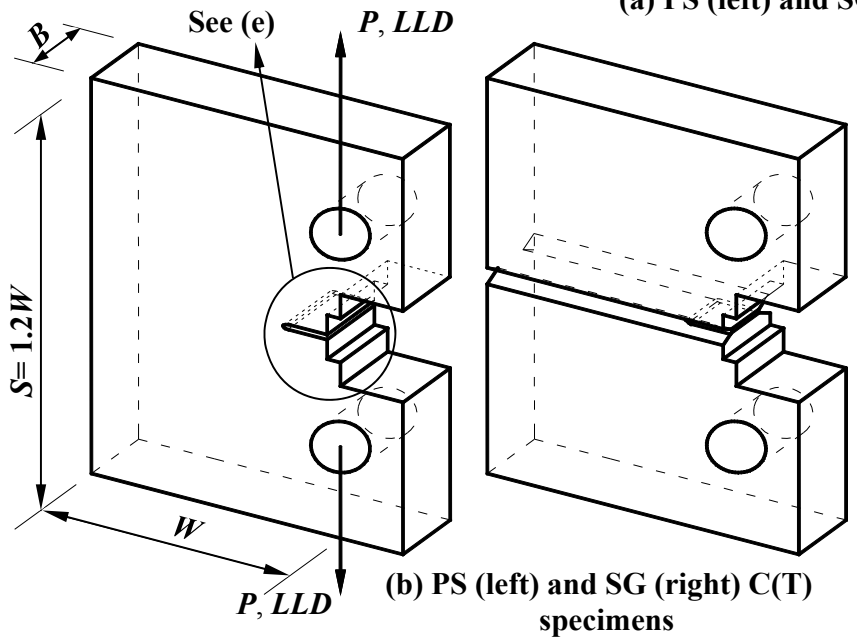

(b) PS (left) and SG (right) C(T) specimens

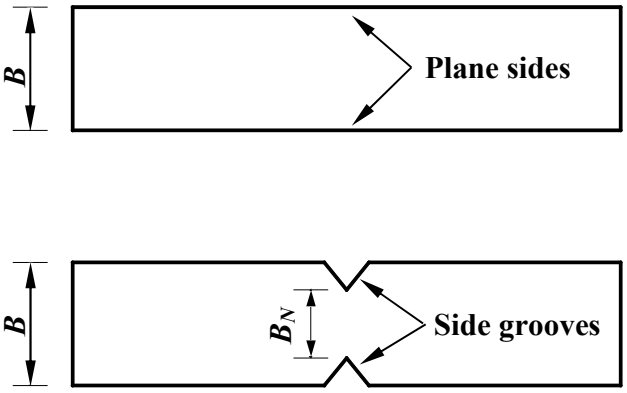

(c) Schematic of side grooves

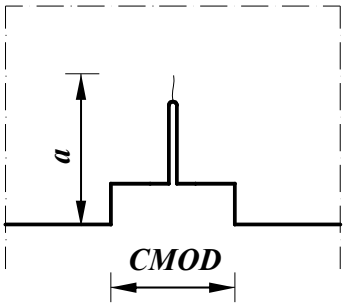

(d) Definition of crack length and *CMOD* in SE(B) specimens

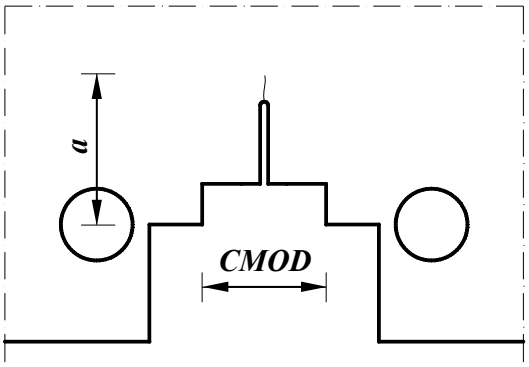

(e) Definition of crack length and *CMOD* in C(T) specimens

Figure 2.1: Schematic of the plane-sided (PS) and side-grooved (SG) specimens

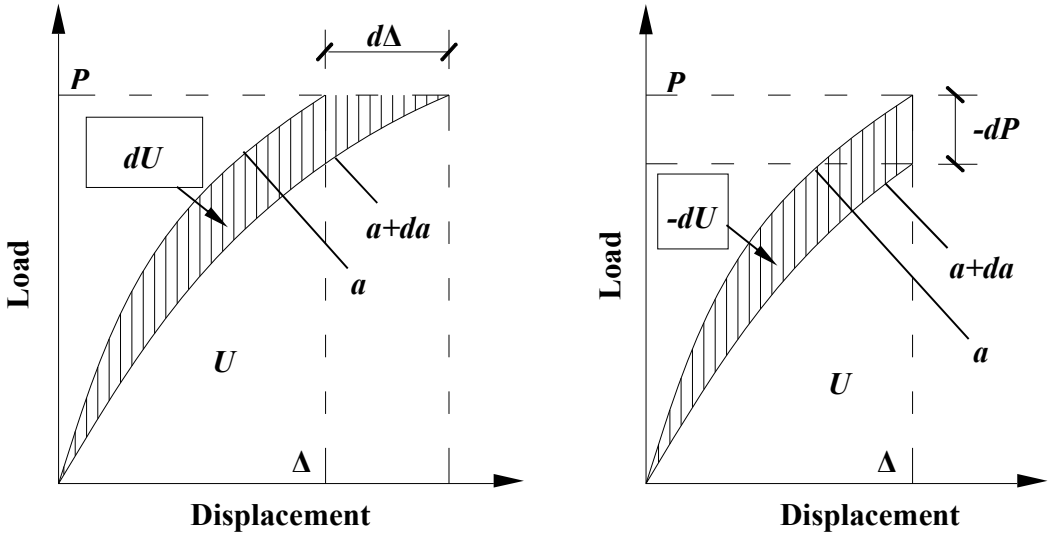

(a) load-control condition **(b) displacement-control condition**

Figure 2.2: Determination of the potential energy

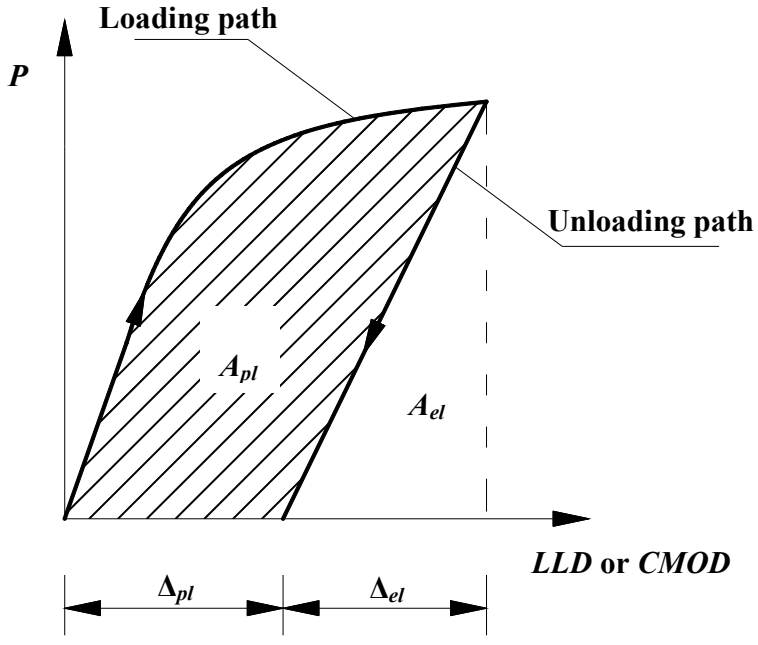

Figure 2.3: Plastic area under the load-displacement curve

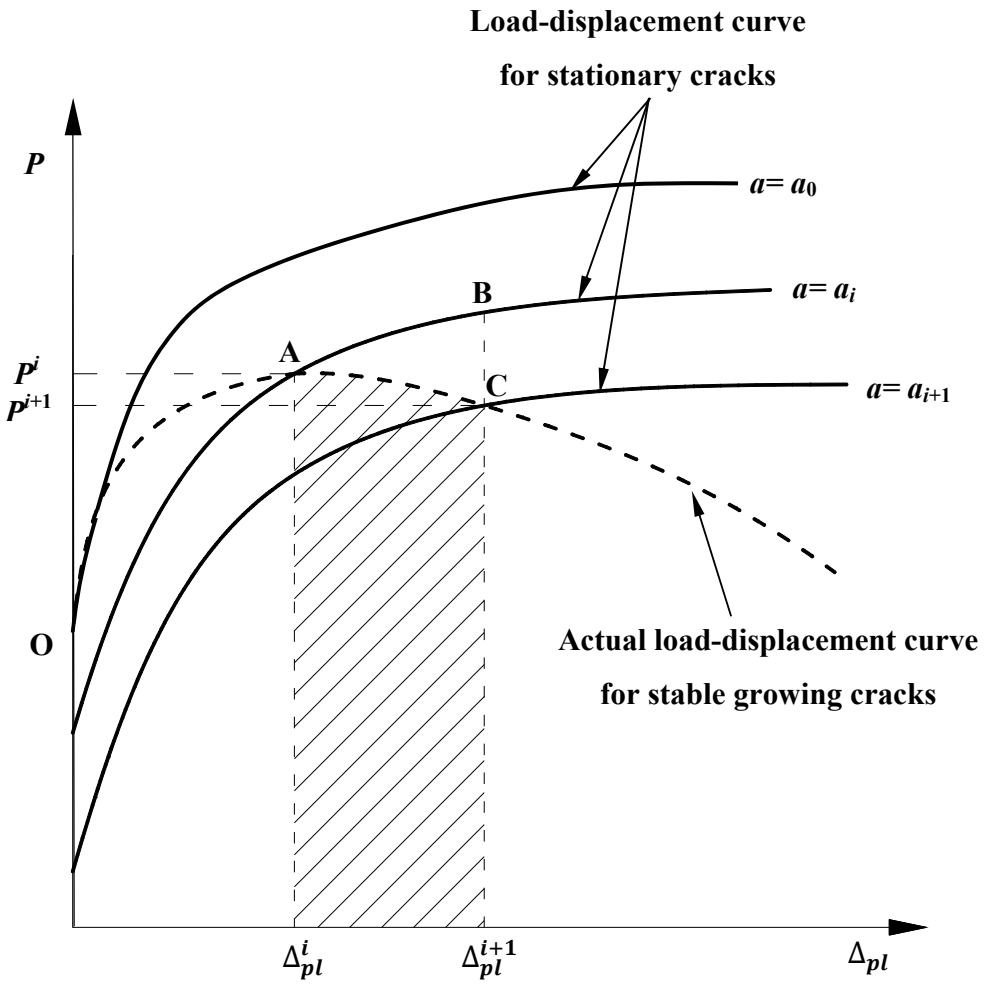

Figure 2.4: Schematic of the estimation of J_{pl} for growing cracks

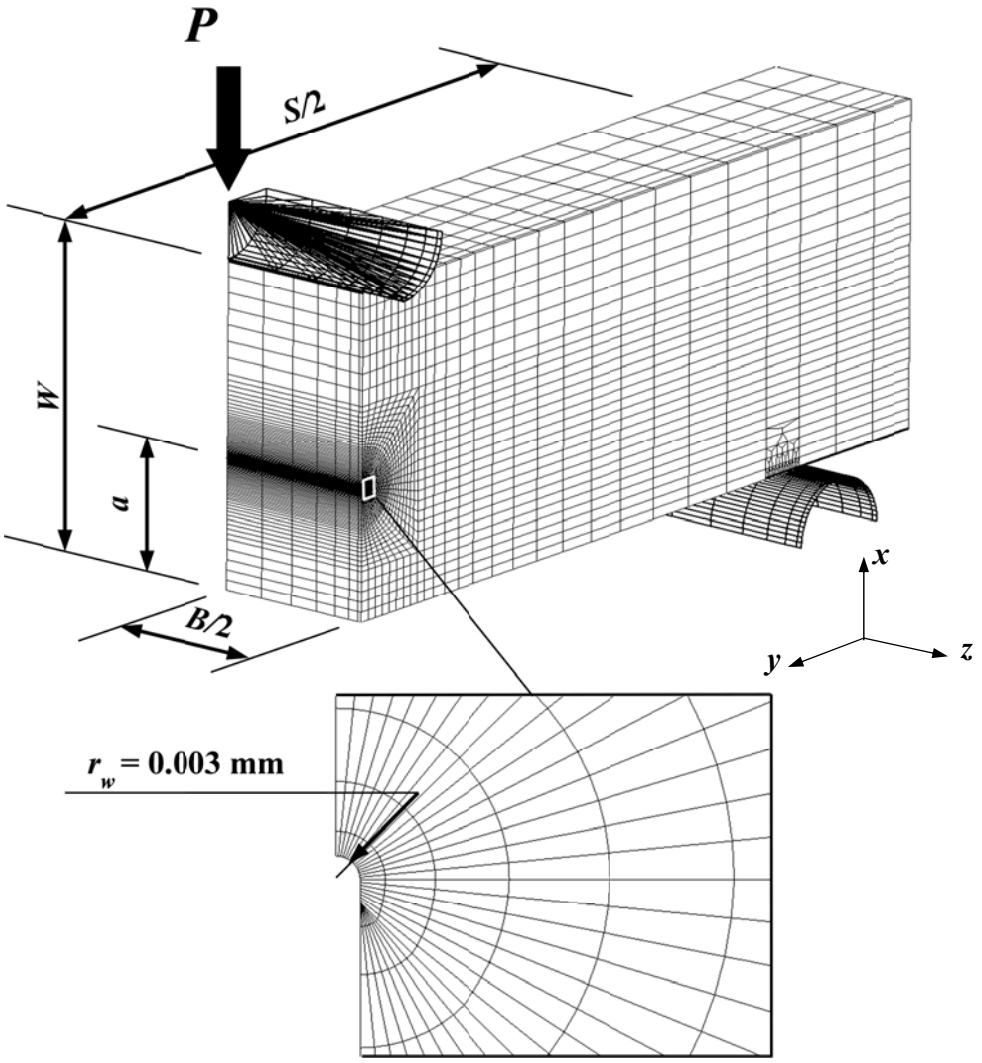

Figure 2.5: Configuration of the finite element model

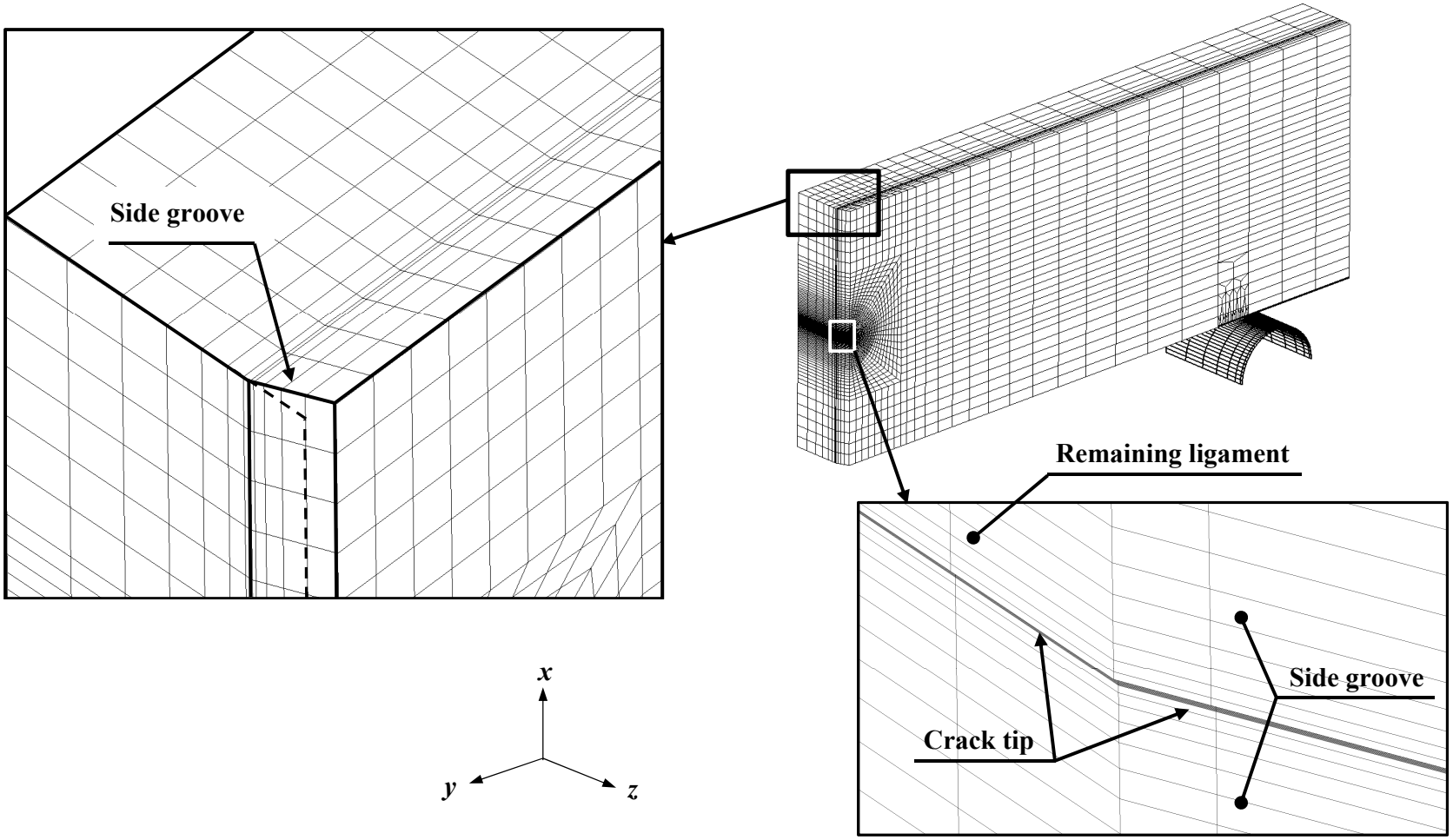

Figure 2.6: Schematics of side-grooved finite element model with *a/W* = 0.5 and *B/W* = 0.5

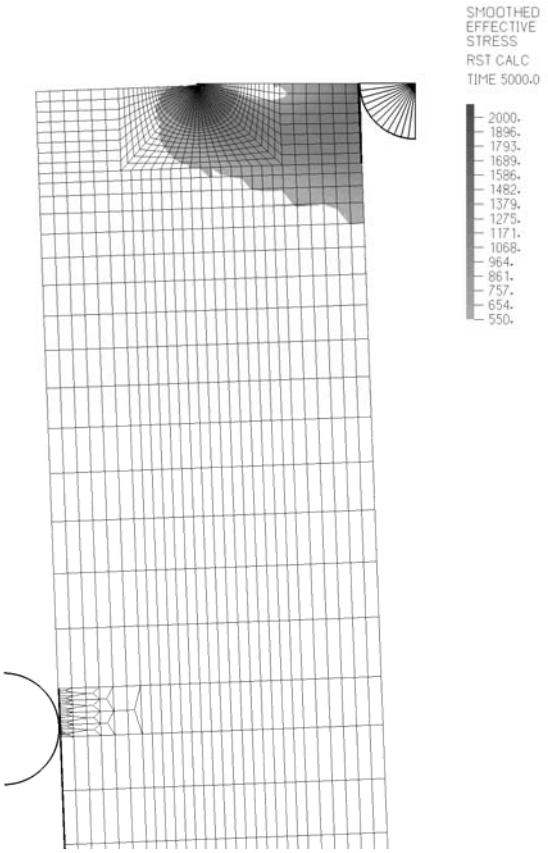

Figure 2.7: Distribution of the effective stress at mid plane in a typical FE model (*a/W* = 0.5 and *B/W* = 1) corresponding to the applied displacement of 1.5mm

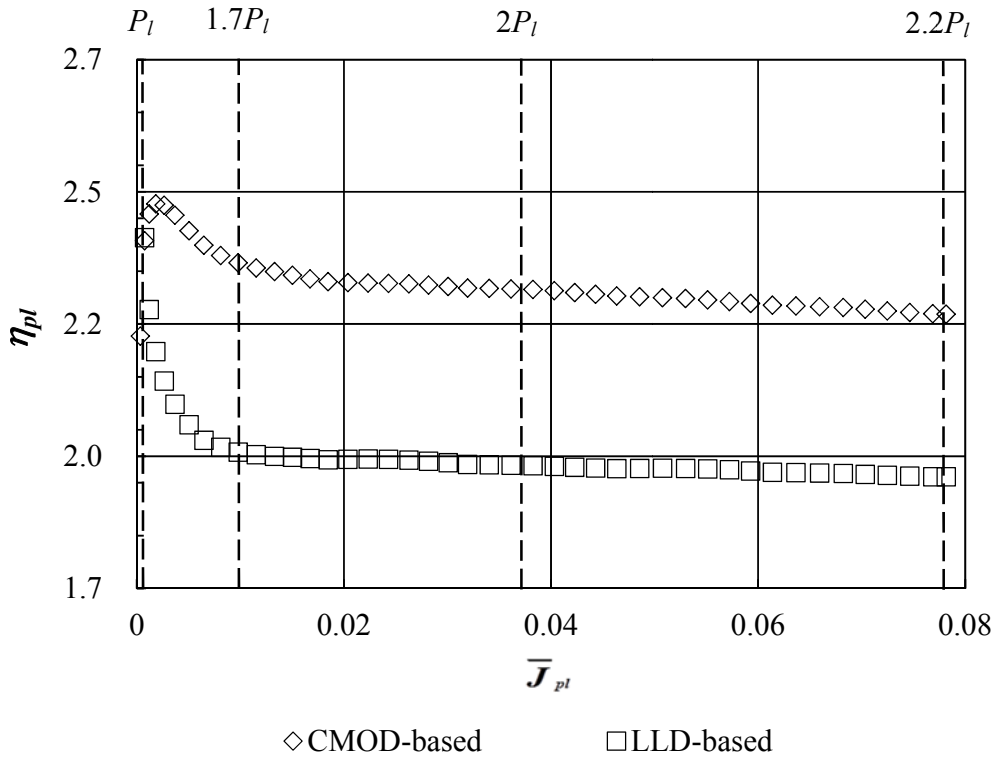

Figure 2.8: Variation of η_{pl} factor corresponding to J_{ave} with normalized J_{pl} for a representative specimen (plane-sided, a/W = 0.7, B/W = 1 and n = 10)

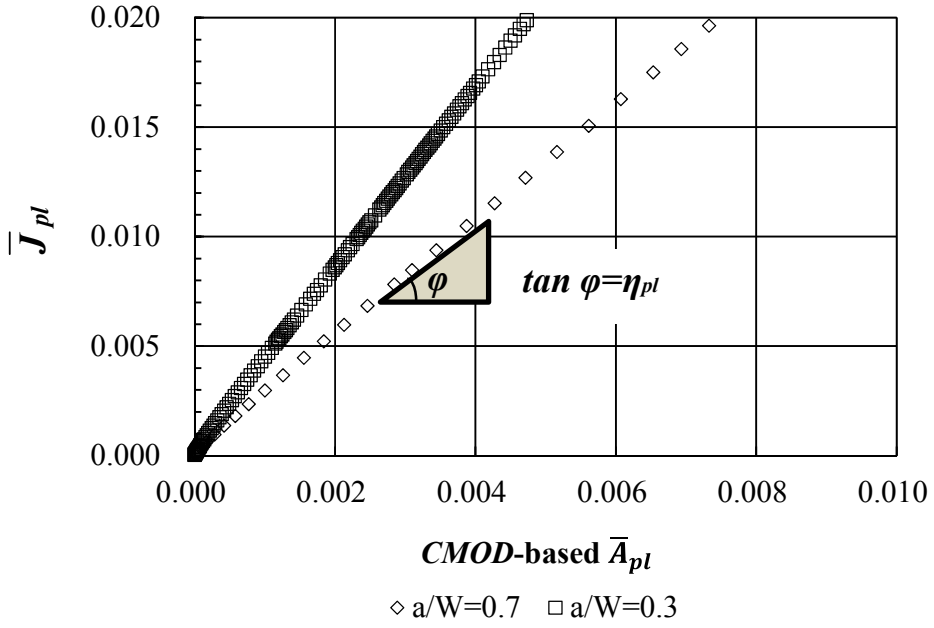

(a) Plane-sided model with B/W = 0.5, n = 10, and J_{mid}

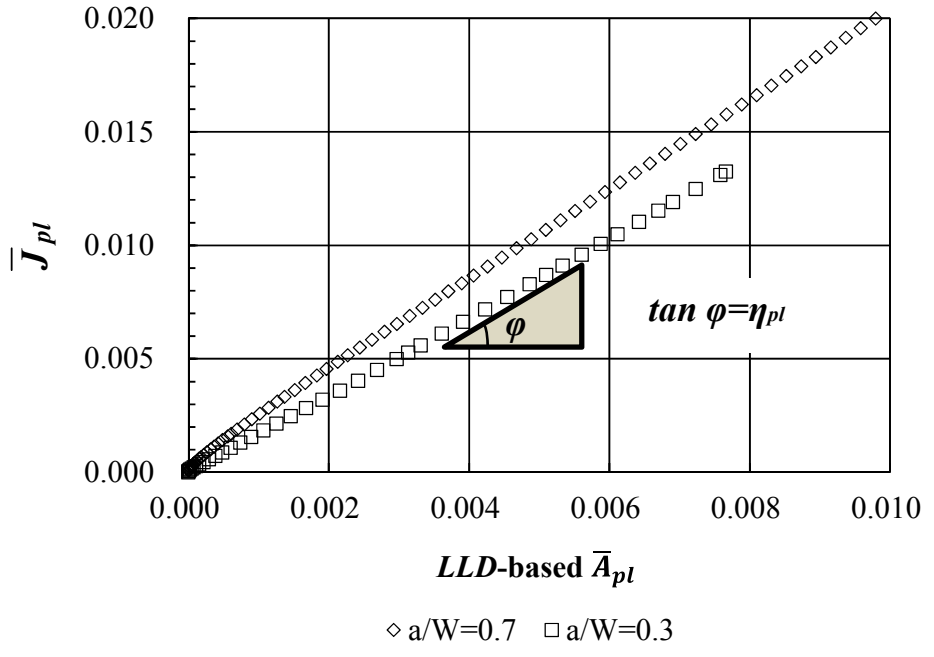

(b) Side-grooved model with B/W = 2, n = 10, and J_{ave}

Figure 2.9: Variation of the normalized plastic J with normalized plastic area

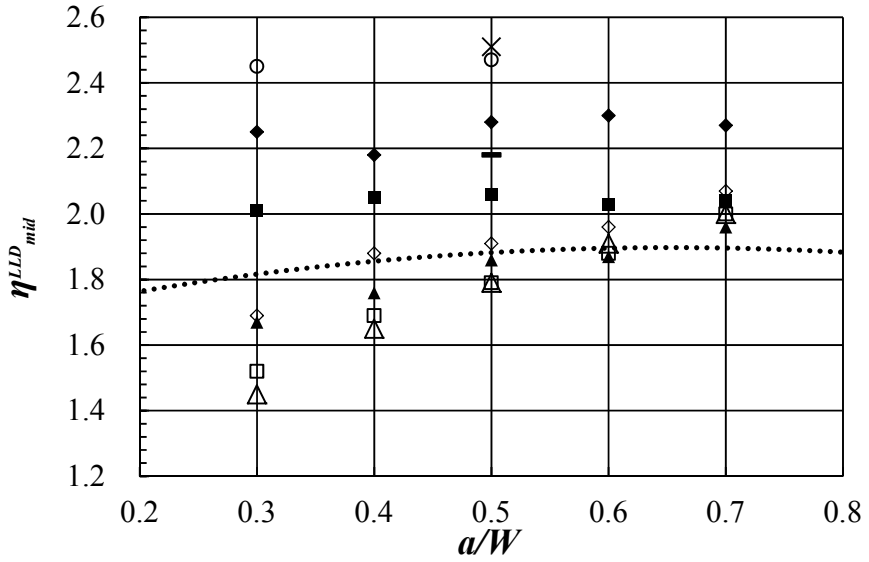

(a) *LLD*-based η_{mid} vs. *a/W*

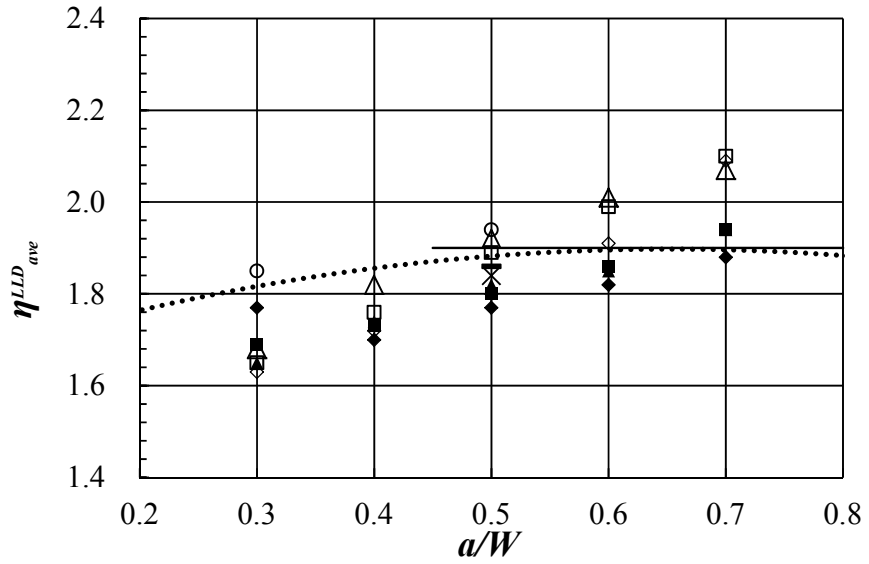

(b) *LLD*-based η_{ave} vs. *a/W*

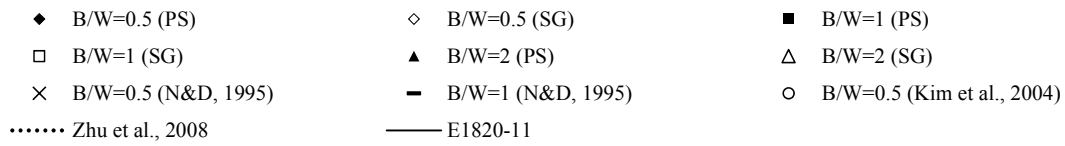

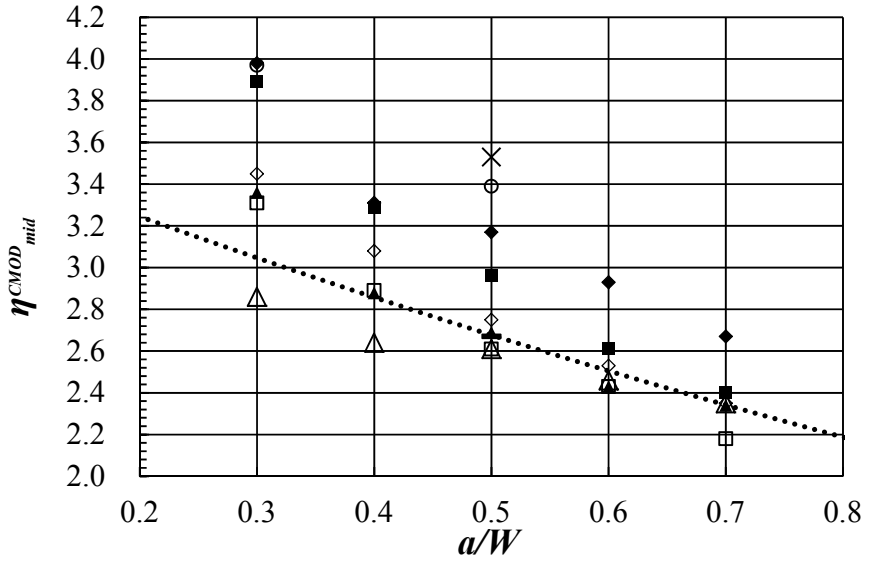

(c) *CMOD*-based η_{mid} vs. *a/W*

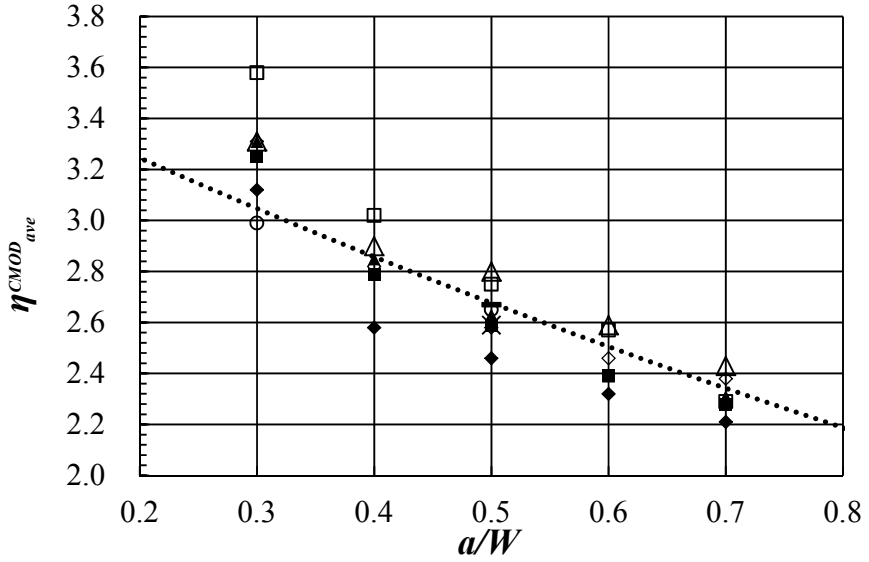

(d) *CMOD*-based η_{ave} vs. *a/W*

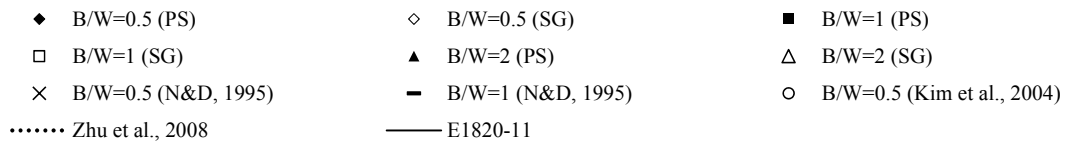

Figure 2.10: Variation of η_{pl} with *a/W* for *n* = 10

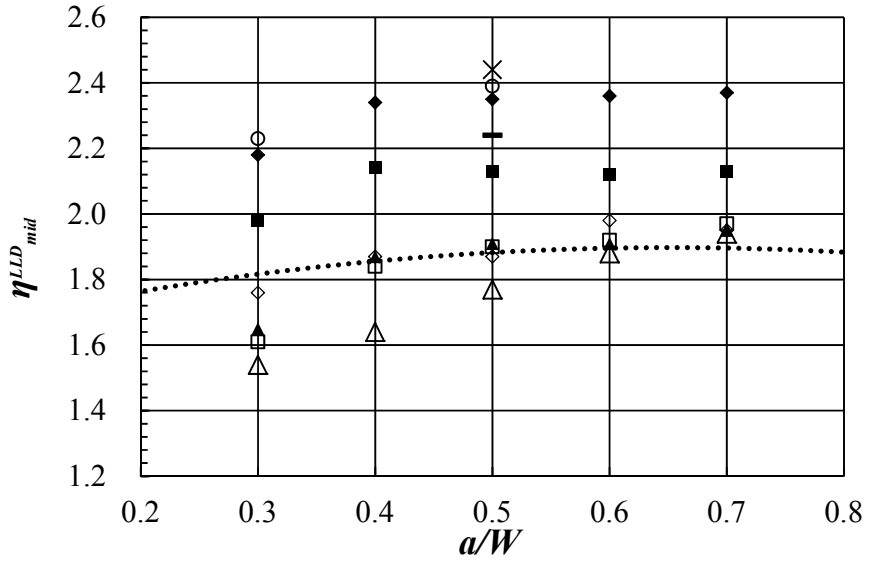

(a) *LLD*-based η_{mid} vs. *a/W*.

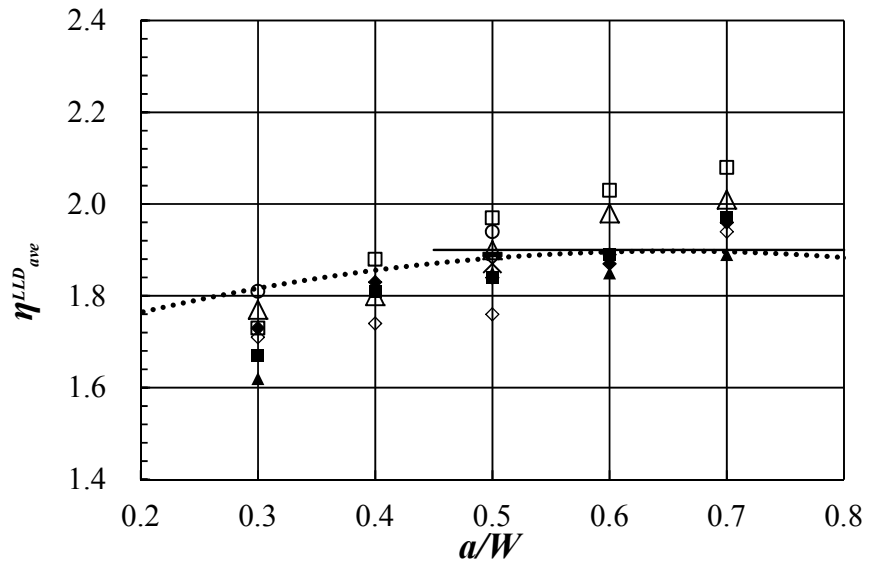

(b) *LLD*-based η_{ave} vs. *a/W*.

◆ B/W=0.5 (PS) ◇ B/W=0.5 (SG) ■ B/W=1 (PS)
□ B/W=1 (SG) ▲ B/W=2 (PS) △ B/W=2 (SG)
× B/W=0.5 (N&D, 1995) ━ B/W=1 (N&D, 1995) ○ B/W=0.5 (Kim et al., 2004)
····· Zhu et al., 2008 —— E1820-11

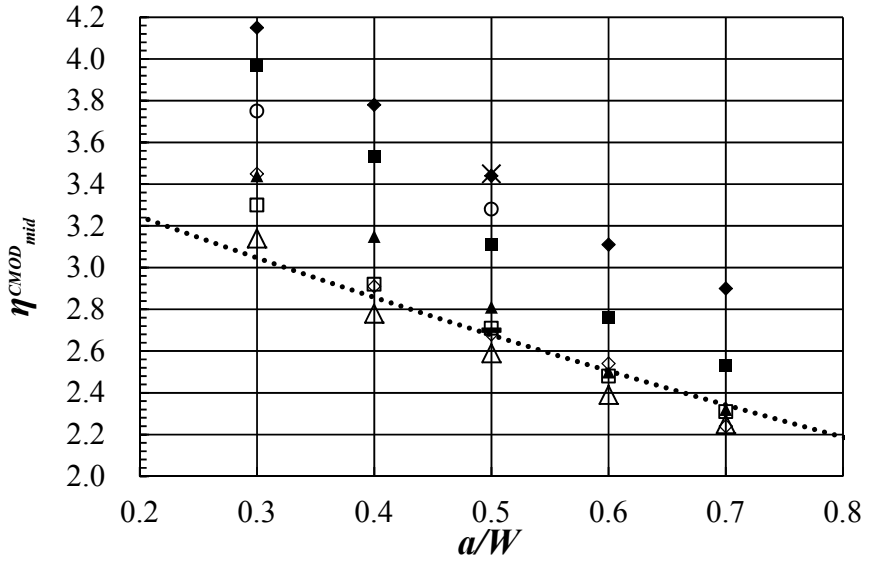

(c) *CMOD*-based η_{mid} vs. *a/W*.

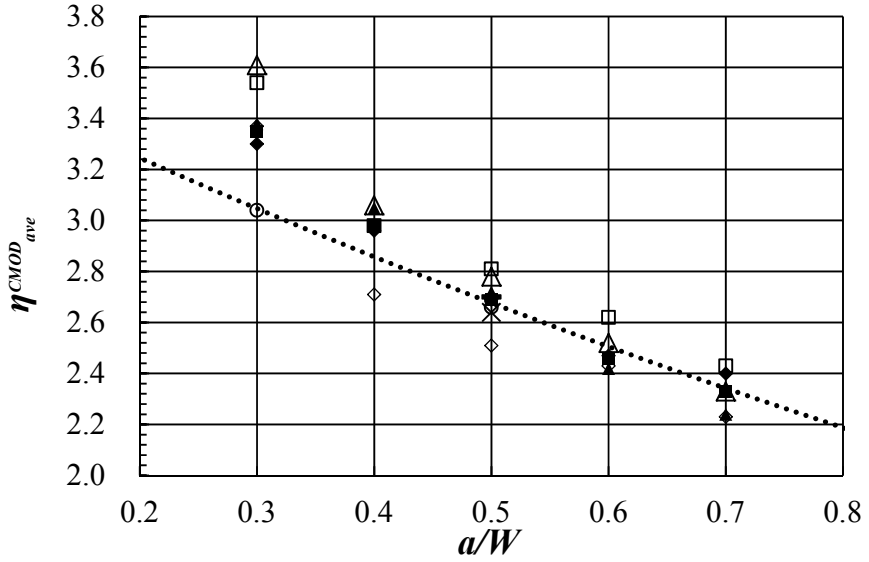

(d) *CMOD*-based η_{ave} vs. *a/W*.

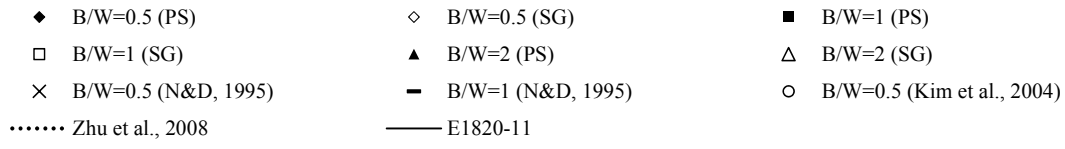

Figure 2.11: Variation of η_{pl} with *a/W* for $n = 5$

Chapter 3 Constraint-corrected *J-R* Curves for Pipeline Steels

3.1 Background and Objective

3.1.1 Constraint Effect

It has been observed that testing specimens made of the same material but with different geometric configurations and/or subjected to different types of loading (e.g. bending and tension) will lead to different *J-R* curves (Brocks and Schmitt, 1995). This phenomenon is attributed to the so-called constraint effect, which is defined as a structural obstacle against plastic deformation and is dependent on the loading and geometry conditions of the specimens (Brocks and Schmitt, 1995). Basically, a high level of constraint leads to a low *J-R* curve because a high level of constraint restricts the plastic deformation and associated energy dissipation in the vicinity of the crack tip and therefore lowers the resistance to fracture. A high level of constraint is equivalent to a high degree of stress triaxiality, which can drive the crack growth more easily (Brocks and Schmitt, 1995; Kim et al., 2004). Figure 3.1 schematically shows five typical *J-R* curves obtained from fracture toughness tests on different types of specimens including the pipe segment under tension, single-edge tension (SE(T)), deeply- (i.e. $a/W \geq 0.45$) and shallow-cracked (i.e. $a/W \leq 0.45$) single-edge bend (SE(B)), and deeply-cracked compact tension (C(T)) specimens. It can be seen that the pipe segment under tension leads to the highest *J-R* curves, followed by the SE(T) specimen. The shallow-cracked SE(B) specimen results in a higher *J-R* curve than that from the deeply-cracked SE(B) specimen. The lowest *J-R* curve results from the deeply-cracked C(T) specimen, which has the highest constraint level among all the specimens shown in the figure. Brocks and Schmitt (1995) pointed out that the use of bend type specimens and deeply-cracked geometry guarantees a high level of the in-plane constraint. The figure indicates that using the small-scale specimens generally leads to conservative *J-R* curves. The non-standard specimens such as the SE(T) and shallow-cracked SE(B) specimens result in less conservative *J-R* curves than those obtained from the deeply cracked SE(B) and C(T) specimens as specified in ASTM E1820-11E2 (ASTM, 2013).

There are two types of constraint effects, namely the in-plane and out-of-plane constraints (Brocks and Schmitt, 1995). The in-plane constraint depends on the loading configuration (i.e. bending or tension) as well as the in-plane dimensions (e.g. width and span of the specimen, and crack length). The out-of-plane constraint depends on the out-of-plane dimension (i.e. thickness) of the specimen (Guo, 1993a, 1993b, 1995). Two parameters, namely Q and A_2, are commonly used in the literature to quantify the in-plane constraint effects (e.g. O'Dowd and Shih, 1991; Chao et al., 1994). Two other parameters, namely h and T_z (Brocks and Schmitt, 1995; Guo, 1993a, 1993b, 1995) have been used to quantify the degree of stress triaxiality at the crack tip, which is directly related to the constraint level. These four parameters are described in the following.

O'Dowd and Shih (1991, 1992, 1994) proposed the Q parameter to describe the difference between the actual stress field and the reference stress field ahead of the crack tip:

$$\sigma_{ij} \approx (\sigma_{ij})_{ref} + Q\sigma_0\delta_{ij} \qquad \text{for } |\theta| \le \frac{\pi}{2} \text{ and } 1 \le \frac{r\sigma_0}{J} \le 5 \tag{3.1}$$

where δ_{ij} is the Kronecker delta; θ and r are defined in Fig. 1.2; σ_0 is the reference stress and typically set equal to the yield strength, and $r\sigma_0/J$ is the (dimensionless) normalized crack tip distance. The reference stress state $(\sigma_{ij})_{ref}$ can be chosen as either the HRR (plane-strain) solution $(\sigma_{ij})_{HRR}$ (O'Dowd and Shih, 1991, 1992), or the stress field corresponding to the small-scale yielding solution $(\sigma_{ij})_{SSY}$ (O'Dowd and Shih, 1994), which is typically obtained from a modified boundary layer (MBL) analysis (Anderson, 2005). Note that $(\sigma_{ij})_{SSY}$ is the more appropriate choice for $(\sigma_{ij})_{ref}$ if the material cannot be characterized by a Ramberg-Osgood stress-strain relationship on which $(\sigma_{ij})_{HRR}$ is based. In the literature, the Q parameter is commonly evaluated from the opening stress in the crack plane at $r\sigma_0/J = 2$ (e.g. O'Dowd and Shih, 1991, 1992; Brocks and Schmitt, 1995), that is, Q is calculated from

$$Q_{HRR} = \frac{\sigma_{22} - (\sigma_{22})_{HRR}}{\sigma_0} \qquad \text{for } \theta = 0 \text{ and } \frac{r\sigma_0}{J} = 2 \tag{3.2}$$

$$Q_{SSY} = \frac{\sigma_{22} - (\sigma_{22})_{SSY}}{\sigma_0} \qquad \text{for } \theta = 0 \text{ and } \frac{r\sigma_0}{J} \geq 1 \tag{3.3}$$

where Q_{HRR} or Q_{SSY} characterizes the level of stress triaxiality, i.e. the degree of constraint, near the crack tip; σ_{22} is the opening stress, i.e. the component of the stress tensor acting in the direction that opens up the crack face, and the actual stress field σ_{ij} can be obtained from the finite element analysis. Values of Q_{HRR} typically range from -2.0 to 0.2 in general two-dimensional plane strain analysis (O'Dowd and Shih, 1991), with the low values representing low levels of constraint.

Zhu and Jang (2001) pointed out that the Q parameters evaluated from Eqs. (3.2) and (3.3) are dependent on load; therefore, the value of Q varies along the J-R curve. To make Q independent of the load, Zhu and Jang (2001) proposed the following modified Q parameter, Q_m:

$$Q_m = \left[\frac{J}{\alpha \varepsilon_0 \sigma_0 I_n L} \right]^{-\frac{1}{n+1}} Q_{HRR} \tag{3.4}$$

where $\varepsilon_0 = \sigma_0/E$; α and n are parameters of the Ramberg-Osgood relationship with n commonly known as the strain hardening exponent; I_n is an integration constant that depends on n, and L is a characteristic length that can be simply set equal to 1 mm. Zhu and Jang (2001) indicated that Q_m as defined in Eq. (3.4) is load-independent for tensile specimens under large loading and for bending specimens under moderate loading based on theoretic and numerical analyses.

Zhu and Leis (2006b) stated that the modified Q_m parameter in Eq. (3.4) may be distance-dependent and may fail to describe the stress field at the crack-tip correctly for bending specimens under large loading. Considering the influence of the global bending stress on the crack-tip stress field in SE(B) specimens and following the bending modification of J-A_2 theory proposed by Chao et al. (2004), Zhu and Leis (2006b) proposed the similar bending modified J-Q solution as

$$Q_{BM} = \left[\left(\frac{J}{\alpha\varepsilon_0\sigma_0 I_n L}\right)\right]^{-\frac{1}{n+1}} \times \left(\frac{\sigma_{22}^{FEA}(r,0) - \sigma_{22}^{HRR}(r,0)}{\sigma_0} + \frac{CMr}{\sigma_0 b^3}\right) \tag{3.5}$$

for $\theta = 0$ and $\frac{r\sigma_0}{J} \geq 1$

where C is a linearization factor; M is the moment per unit thickness acting at the center of the span and equals $PS/4B$ (P is the applied load, and S and B are respectively the span and thickness of the specimen as illustrated in Fig. 2.1) for the SE(B) specimen. σ_{22}^{FEA} and σ_{22}^{HRR} are the opening stress ahead of the crack tip obtained from the finite element analysis (FEA) (i.e. the actual opening stress) and HRR solution respectively.

By assuming a plastic hinge located at the neutral axis in the mid-span of a bending beam and the linear distribution of the elastic stress along the uncracked ligament, Chao et al. (2004) showed that the factor C in Eq. (3.5) for the SE(B) specimen approximately equals six. Alternatively, the so-called two-point matching method (Chao et al., 2004; Zhu and Leis, 2006b) can be used to determine C. Let $\sigma_{22}^{FEA}(r_1,0)$ and $\sigma_{22}^{FEA}(r_2,0)$ denote two opening stresses directly ahead of crack tip (i.e. $r = r_1$ and $r = r_2$, $\theta = 0$) within the region of interest such as $1 \leq r/(J/\sigma_0) \leq 5$ obtained from FEA. The constant C in Eq. (3.5) can be determined by using Eq. (3.6) based on the assumptions that Q_{BM} are distance-independent within the region of interest:

$$C = \frac{\sigma_0 b^3}{M(r_2 - r_1)}\left\{\left[\left(\frac{J}{\alpha\varepsilon_0\sigma_0 I_n L}\right)\right]^{-\frac{1}{n+1}} \times \left[\left(\frac{L}{r_2}\right)^{\frac{1}{n+1}} - \left(\frac{L}{r_1}\right)^{\frac{1}{n+1}}\right]\tilde{\sigma}_{22}(0,n) - \left(\frac{\sigma_{22}^{FEA}(r_2,0) - \sigma_{22}^{FEA}(r_1,0)}{\sigma_0}\right)\right\} \tag{3.6}$$

where r_1 and r_2 are typically selected as $r_1/(J/\sigma_0) = 1$ and $r_2/(J/\sigma_0) = 5$ (Chao et al., 2004). Once C is determined from Eq. (3.6), Q_{BM} can be determined from Eq. (3.5) at a specific location ahead of the crack, e.g. $r/(J/\sigma_0) = 2$ and $\theta = 0$.

Based on the rigorous asymptotic analysis of a plane-strain crack in a power-law hardening material, Chao and his coworkers (Chao et al., 1994; Yang et al., 1993a and 1993b) proposed the *J*-A_2 three-term solution for the crack-tip stress field:

$$\frac{\sigma_{ij}}{\sigma_0} = A_1\left[\left(\frac{r}{L}\right)^{s_1}\tilde{\sigma}_{ij}^{(1)}(\theta,n) + A_2\left(\frac{r}{L}\right)^{s_2}\tilde{\sigma}_{ij}^{(2)}(\theta,n) + A_2^2\left(\frac{r}{L}\right)^{s_3}\tilde{\sigma}_{ij}^{(3)}(\theta,n)\right] \tag{3.7}$$

where A_1 and s_1 are given by the HRR fields:

$$A_1 = \left(\frac{J}{\alpha\varepsilon_0\sigma_0 I_n L}\right)^{-s_1}, \qquad s_1 = -\frac{1}{n+1} \tag{3.8}$$

the angular functions $\tilde{\sigma}_{ij}^{(k)}$ (k = 1, 2 and 3), the stress power exponents (s_1, s_2 and s_3) and the dimensionless integration constant I_n are functions of the hardening exponent n only and tabulated by Chao and Zhang (1997). The first term of the right hand side of Eq. (3.7) is the HRR solution, as the equation simplifies to the following for A_2 = 0:

$$\frac{\sigma_{ij}}{\sigma_0} = A_1\left(\frac{r}{L}\right)^{s_1}\tilde{\sigma}_{ij}^{(1)}(\theta,n) = \left(\frac{J}{\alpha\sigma_0\varepsilon_0 I_n r}\right)^{\frac{1}{n+1}}\tilde{\sigma}_{ij}^{(1)}(\theta,n) = \frac{(\sigma_{ij})_{HRR}}{\sigma_0} \tag{3.9}$$

The second and third terms in Eq. (3.7) represent the difference between the full-field solution and HRR solution, and include an undetermined scaling factor A_2. The value of A_2 can be determined by setting σ_{ij} in Eq. (3.7) to σ_{22} at a given point (e.g. $r\sigma_0/J$ = 2 and θ = 0) obtained from FEA and solving the equation for A_2. Note that Eq. (3.7) is essentially a quadratic equation of A_2 that includes two roots of A_2. Both roots are acceptable, but typically the negative root is used in the literature (Chao et al., 2004; Zhu and Leis, 2006a). A higher value of A_2 represents a higher level of the constraint.

It is well known that the stress triaxiality at the crack tip directly affects the main micromechanisms of fracture (Shen et al., 2004). The stress triaxiality, h, can be defined as (Brocks and Schmitt, 1995):

$$h = \frac{\sigma_h}{\sigma_e} = \frac{(\sigma_{11} + \sigma_{22} + \sigma_{33})}{3\sqrt{\frac{3}{2} s_{ij} s_{ij}}} \qquad \text{for } \theta = 0 \text{ and } \frac{r\sigma_0}{J} = 2 \tag{3.10}$$

where the hydrostatic stress, σ_h, equals $(\sigma_{11}+\sigma_{22}+\sigma_{33})/3$, i.e. the first invariant of the stress tensor, and does not cause any plastic deformation; $\sigma_e = \sqrt{\frac{3}{2} s_{ij} s_{ij}}$ is the von Mises effective stress, and s_{ij} is the deviatoric stress tensor ($s_{ij} = \sigma_{ij} - \sigma_h$), which is responsible for the plastic flow (Brocks and Schmitt, 1995).

Another commonly used parameter to describe the state of triaxiality as well as the so called out-of-plane constraint is T_z, suggested by Guo (1993a, 1993b, 1995):

$$T_z = \frac{\sigma_{33}}{\sigma_{11} + \sigma_{22}} \qquad \text{for } \theta = 0 \text{ and } \frac{r\sigma_0}{J} = 2 \tag{3.11}$$

where σ_{11} is the stress acting in the direction of the crack propagation, and σ_{33} is the stress parallel to the crack front.

The advantage of using h and T_z is that they do not require a reference stress state such as the HRR solution and can be easily calculated from the actual stress state obtained from FEA.

3.1.2 Constraint-corrected *J-R* Curve

As described in Section 3.1.1, the application of *J-R* curves determined from small-scale specimens in real flawed structures generally leads to conservative, sometimes excessive, design and assessment of the structure. This is known as the fracture toughness

transferability issue (Zhu, 2006a). Extensive research has been carried out to deal with the transferability issue (e.g. Minami et al., 1997; Ruggieri et al., 2000; Laukkanen et al., 2003; Scibetta et al., 2009). One of the approaches adopted in such research is to develop constraint-corrected *J-R* curves (Zhu and Jang, 2001) based on the *J-Q* and *J-A*$_2$ theories.

The idea of constraint-corrected *J-R* curves is described as follows. As specified in ASTM E1820-11E2 (ASTM, 2013), a given *J-R* curve can be approximated by a power-law relationship between *J* and the crack extension, Δa:

$$J\left(\Delta a\right) = C_1\left(\frac{\Delta a}{k}\right)^{C_2} \tag{3.12}$$

where k = 1 mm, and C_1 and C_2 are the power-law coefficients. The basic premise of constraint-corrected *J-R* curves is that a given *J-R* curve is associated with a given value of the constraint parameter, denoted by *Y*. Therefore, a suite of *J-R* curves, each associated with a different value of the constraint parameter, can be expressed in the following general form:

$$J\left(\Delta a, Y\right) = C_1\left(Y\right)\left(\frac{\Delta a}{k}\right)^{C_2(Y)} \tag{3.13}$$

where $C_1(Y)$ and $C_2(Y)$ are the power-law coefficients that are functions of *Y*. Given the value of the constraint parameter *Y*, the corresponding *J-R* curve can then be determined.

Zhu and Leis (2005, 2006a) developed a general approach to determine $C_1(Y)$ and $C_2(Y)$, as schematically illustrated in Figure 3.2. For a given *J-R* curve, the *J* values corresponding to two crack extensions, Δa_1 and Δa_2, are denoted by

$$\begin{aligned} J\left(\Delta a = \Delta a_1\right) &= J_{\Delta a_1} \\ J\left(\Delta a = \Delta a_2\right) &= J_{\Delta a_2} \end{aligned} \tag{3.14}$$

Based on at least three experimentally-determined *J-R* curves and their corresponding values of the constraint parameter *Y*, one can develop $J_{\Delta a_1}$ and $J_{\Delta a_2}$ as functions of *Y* from curve fitting as illustrated in Figs. 3.2(a) and 3.2 (b). Zhu and Leis (2005, 2006a)

suggested choosing Δa_1 = 0.2 mm, which is generally considered to correspond to the initiation of crack growth ($\Delta a \leq 0.2$ mm is typically attributed to the crack tip blunting as opposed to growth (Zhu and Joyce, 2012)), and Δa_2 = 1.0 mm. Given $J_{0.2}(Y)$ and $J_{1.0}(Y)$, the power-law coefficients, $C_1(Y)$ and $C_2(Y)$, can be determined as follows:

$$C_1(Y) = J_{1.0}(Y) \tag{3.15a}$$

$$C_2(Y) = \frac{\ln J_{0.2}(Y) - \ln J_{1.0}(Y)}{\ln 0.2} \tag{3.15b}$$

The constraint parameters indicated in Eqs (3.13)-(3.15) can be either Q or A_2 evaluated from FEA at $J = J_{0.2}$, assuming a stationary crack (i.e. no crack growth) in the analysis given that $\Delta a \leq 0.2$ mm is due to the crack blunting. Chao and Zhu (2000) as well as Zhu and Jang (2001) developed the constraint-corrected *J-R* curve associated with experimentally-determined *J-R* curves from a set of SE(B), C(T) and SE(T) specimens tested by Joyce and Link (1995, 1997), whereas Zhu and Leis (2005, 2006a) developed the constraint-corrected *J-R* curve based on six SE(B) specimens with different crack lengths (i.e. a/W = 0.24, 0.25, 0.42, 0.43, 0.63 and 0.64) and the same thickness (i.e. B/W = 0.5) (Shen et al., 2004). In terms of the constraint parameter Q, Zhu and Jang (2001) and Zhu and Leis (2006a) determined the constraint-corrected *J-R* curves for different ductile metals, whereas Chao and Zhu (2000), Lam et al. (2003), Zhu and Leis (2005) and Wang et al. (2009) constructed the constraint-corrected *J-R* curves in reference to the constraint parameter A_2.

It is noted that the aforementioned studies to develop constraint-corrected *J-R* curves are all based on the two-dimensional (2D) small-strain FEA. That is, the constraint parameter Y (i.e. Q or A_2) associated with a given *J-R* curve is evaluated from 2D small-strain FEA. In reality, the test specimen (e.g. SE(B) and C(T)) from which the *J-R* curve is experimentally obtained are three-dimensional (3D). The use of 2D FEA to simulate 3D specimens may not be adequate, for example, if the specimens are side-grooved. Furthermore, the large displacement/large strain-based analysis is more representative of the actual kinematics of the specimens during the *J-R* curve test than the small strain-

based analysis. Finally, all of the previous studies employ either Q or A_2 as the constraint parameter. The use of other constraint parameters, such as h and T_z, to develop constraint-corrected *J-R* curves has not been reported in the literature.

3.1.3 Objective and Approach

The main objective of the work reported in this chapter was to develop the constraint-corrected *J-R* curve based on 3D FEA. The constraint parameters for a set of SE(B) specimens reported in the literature were evaluated using 3D large displacement/large strain FEA. The constraint parameters were then combined with the experimentally determined *J-R* curves corresponding to medium- and deeply cracked SE(B) specimens to develop a constraint corrected *J-R* curve. The constraint parameters considered in this study include Q, A_2, h and T_z. The developed constraint-corrected *J-R* curve was validated using the *J-R* curve obtained from shallow-cracked SE(B) specimens.

Based on the approach proposed by Zhu and Leis (2005, 2006a), the experimentally determined *J-R* curve corresponding to a given SE(B) specimen was fitted by a power-law relationship between J and Δa. The constraint parameter Y associated with the *J-R* curve was set to be either Q, A_2, h or T_z evaluated from 3D FEA at the mid-plane of the specimen corresponding to $J_{0.2}$. All the specimens in FEA have stationary cracks with the crack length equal to the corresponding initial crack length. The power law coefficients, $C_1(Y)$ and $C_2(Y)$, were then expressed as functions of the constraint parameter Y based on Eqs. (3.15a) and (3.15b). The adequacy of different constraint parameters (i.e. Q, A_2, h and T_z) in terms of characterizing the constraint-corrected *J-R* curve was investigated.

This chapter is organized as follows. Section 3.2 presents the experimentally-determined *J-R* curves that were employed in this study. The finite element analysis and determination of the constraint parameters are described in Section 3.3. The construction and validation of the constraint-corrected *J-R* curve based on the experimentally-

determined *J-R* curves and constraint parameters are presented in Section 3.4. The conclusions of the study are presented in Section 3.5.

3.2 Experimentally-determined *J-R* curves

The *J-R* curves used in this study are from six SE(B) specimens tested and reported by Shen et al. (2004). All the specimens were fabricated from the based metal of a pipe segment that has an outside diameter of 1219 mm (48 in.) and a wall thickness of 12.7 mm (0.5 in.), and is made of the API X80 (API, 2012) steel with a minimum specified yield strength (SMYS) of 550 MPa (80 ksi). The mechanical properties of the steel were measured by Shen et al. (2004) using flattened coupons extracted along the longitudinal direction of the pipe segment (see Fig. 3.3). The average values of Young's modulus E, yield strength σ_y, and ultimate tensile stress σ_{UTS} were reported to be 207 GPa, 568 MPa, and 675 MPa, respectively. The Cauchy (true) stress-logarithmic (true) strain relationship of the steel was found to be well represented by the following Ramberg-Osgood equation:

$$\frac{\varepsilon}{\varepsilon_0} = \frac{\sigma}{\sigma_0} + \alpha\left(\frac{\sigma}{\sigma_0}\right)^n \tag{3.16}$$

where $\alpha = 1.07$, $n = 13.3$, $\sigma_0 = \sigma_y = 568$MPa, and $\varepsilon_0 = \sigma_0/E$.

The crack planes in the SE(B) specimens are orientated in the L-C direction; that is, the specimen is in the pipe longitudinal direction, and the crack propagates in the circumferential direction (see Fig. 3.3), following the specifications in ASTM E399-12E1 (ASTM, 2013).

All six specimens have the same width (W = 23 mm), thickness (B/W = 0.5) and span length (S/W = 4). All specimens are side-grooved with the depth of the side groove equal to 10%B on each side (see Fig. 2.6 for a schematic side-grooved specimen) as recommended by ASTM E1820-11E2 (2013). The initial crack lengths (a/W) in the six

specimens are 0.24, 0.25, 0.42, 0.43, 0.63 and 0.64 respectively. Therefore, two specimens are shallow-cracked; two are medium-cracked; and two are deeply-cracked. The six specimens are designated as SEB24, SEB25, SEB42, SEB43, SEB63 and SEB64, respectively, based on their corresponding initial crack lengths.

All the tests on SE(B) specimens were conducted at room temperature (about 20℃) using a servo-hydraulic test system. The unloading compliance method was used to evaluate the *J*-*R* curves corresponding to these specimens based on the compliance equations given in Appendix B. Figure 3.4 depicts the *J*-*R* curves experimentally determined from the six SE(B) specimens. It can be seen that some data points corresponding to $\Delta a \leq 0.2$ mm show a trend of reverse crack growth, which is due to the inadequate accuracy of the unloading compliance method in the range of small crack growths. The figure shows that as *a*/*W* decreases (i.e. the constraint level decreases), the *J*-*R* curve becomes higher. This is consistent with other *J*-*R* test results reported in the literature. The test data associated with each of the specimens were then used to fit a power-law relationship between *J* and Δa, as given by Eq. (3.12), using the least squares method. The values of C_1, C_2, $J_{0.2}$ and $J_{1.0}$ associated with the six *J*-*R* curves are listed in Table 3.1.

3.3 Finite Element Analysis

3.3.1 Finite Element Model

The commercial software ADINA 8.7.4 (ADINA, 2012) was used to carry out the finite element analysis of the six SE(B) specimens described in Section 3.2 to evaluate *J* and the constraint parameters. An elastic-plastic constitutive model employing the incremental plasticity and large displacement/large strain formulation was adopted. The von Mises yield criterion and isotropic hardening elements was selected in the analysis. The geometric configuration of a typical SE(B) specimen in the FEA is shown in Fig. 3.5 together with the fixation and loading conditions. The 8-node 3D brick isoparametric elements with 2×2×2 integration were used; the accuracy of using such elements to calculate *J* for SE(B) specimens has been shown to be adequate (Kulka and Sherry, 2012).

The analysis was carried out for a stationary crack, with the crack length in a given specimen equal to its initial crack length. Due to symmetry, only a quarter of a given specimen was modeled in the FEA. A blunt crack tip with a radius r_w = 0.003 mm (see Fig. 2.5) was modeled to facilitate the large-deformation calculation (Graba, 2011). A sharp V-notch (i.e. the radius of the notch was not considered) with a total thickness reduction of 20%B (10%B on each side) was used to simulate the side-grooves in the specimens. Note that the blunt crack tip is also prepared through the thickness of the side grooves as shown in Fig. 2.6 to mitigate the impact of the singularity caused by the sharp V-notch under tension on the large-strain analysis.

A spider-web mesh around the crack tip was established with 45 concentric semicircles (i.e. rings) surrounding the crack tip. The in-plane size of the elements closest to the crack tip is around 0.003 mm, and about 1/100 of the in-plane size of the elements in the outermost ring. The model was divided into 25 layers along the thickness direction (17 layers between the symmetric plane and the root of the side groove, and 8 layers between the root of the side groove and free surface). The mesh density increases from the mid plane to the free surface to capture the high stress gradients near the free surface. The total number of elements is approximately 22,900 in a typical specimen. Two contact rollers were defined to simulate the rollers supporting and loading the specimen. The elastic modulus of the contact element was set as ten times that of the specimen. Rigid links were created to connect the loading point and the roller surface. Using contact rollers in the FEA can reflect the real test condition such as the sliding occurring between the specimen and the rollers as well as the large deformation in the contact surface.

The J-integral was computed using the virtual crack extension method implemented in ADINA (Anderson, 2005; ADINA, 2012, see Appendix A). To ensure the path-independence of the calculated J values, the two outmost semicircular rings surrounding the crack tip were used to define the virtual shifts. Displacement-controlled loading was applied in all the models. For models with $a/W \geq 0.4$, the displacement was increased from 0 to 4.5 mm through 15,000 steps, whereas it was increased from 0 to 2 ~ 2.5 mm through 20,000 steps for models with $a/W < 0.4$.

3.3.2 Analysis Results

The local J value at each layer, J_{loc}, and the average J value over the entire crack front, J_{ave}, were output from the FEA. The J_{loc} at the mid-plane (i.e. $z = 0$) of the crack front is denoted as J_{mid}. Figure 3.6 shows the distributions of J_{loc} along the crack front at different loading levels (characterized by the non-dimensional quantity $J_{ave}/b\sigma_0$) for the SE(B) specimens with a/W = 0.24, 0.42 and 0.64. This figure indicates that the distribution of J_{loc} along the crack front depends on a/W and the loading level. For similar loading levels the distribution of J_{loc} along the crack front tends to be more uniform as a/W increases. For a given a/W ratio, the distribution of J_{loc} becomes less uniform as the loading level increases.

Figure 3.7 shows the distribution of σ_{22} obtained at the mid-plane of the crack front at different loading levels (characterized by $J_{mid}/b\sigma_0$) as a function of the normalized distance from the crack tip, $r/(J_{mid}/\sigma_0)$, for SEB24, SEB42 and SEB64 respectively. Also shown in the figure is the σ_{22} obtained from the HRR solution. This figure shows that the distribution of σ_{22} at the mid-plane ahead of the crack tip is largely influenced by a/W. For the deeply-cracked specimen (i.e. SEB64), the distribution of σ_{22} is approximately linear for $r/(J_{mid}/\sigma_0) > 1$ and $J_{mid}/b\sigma_0 \geq 0.014$, implying a strong impingement of the bending stress on the crack-tip stress field. As a/W decreases from 0.64 to 0.42 and then to 0.24, the impact of the bending stress on σ_{22} becomes less and less pronounced. Furthermore, at $r/(J_{mid}/\sigma_0) = 2$ and similar loading levels (e.g. $J_{mid}/b\sigma_0 \approx 0.025$), the difference between the σ_{22} values corresponding to the HRR solution and FEA results increases as a/W decreases, which reflects a decrease in the constraint level as a/W decreases.

3.3.3 Determination of Constraint Parameters

The constraint parameters Q, A_2, h and T_z at the mid-plane were evaluated at $J_{ave} = J_{0.2}$ for the six SE(B) specimens in this study. Four different Q parameters, namely Q_{HRR}, Q_m, Q_{BM1} and Q_{BM2}, were evaluated. Equations (3.2) and (3.4) were used to evaluate Q_{HRR} and Q_m, respectively. Q_{BM1} and Q_{BM2} were both evaluated from Eq. (3.5) at $r/(J_{mid}/\sigma_0) = 2$ and $\theta = 0$. For Q_{BM1}, C is calculated from Eq. (3.6) with $r_1/(J_{mid}/\sigma_0) = 1$ and $r_2/(J_{mid}/\sigma_0) = 5$, whereas $C = 6$ in Eq. (3.5) for Q_{BM2}. The parameter A_2 was computed from Eq. (3.7) with $r/(J_{mid}/\sigma_0) = 2$. The stress triaxiality parameter h was computed using Eq. (3.10) based on the output hydrostatic stress σ_h and von Mises effective stress σ_e from FEA. Finally, the constraint parameter T_z was evaluated using Eq. (3.11) based on the three normal stresses, σ_{11}, σ_{22} and σ_{33}, obtained from FEA. Values of these constraint parameters are tabulated in Table 3.2.

3.4 Construction and Validation of Constraint-corrected *J-R* Curve

In this study, the *J-R* curves of the four medium- and deeply-cracked specimens (i.e. SEB42, SEB43, SEB63 and SEB64) were used to develop the constraint-corrected *J-R* curves, whereas the *J-R* curve of the two shallow-cracked specimens (i.e. SEB24 and SEB25) were used to validate the developed constraint-corrected *J-R* curve.

Figures (3.8) through (3.14) depict the relationship between $J_{0.2}$ and $J_{1.0}$ as obtained from the experimentally-determined *J-R* curves associated with the six specimens and the corresponding values of the constraint parameters, Q_{HRR}, Q_m, Q_{BM1}, Q_{BM2}, A_2, h and T_z. These figures indicate that the value of a given constraint parameter in general decreases as $J_{0.2}$ ($J_{1.0}$) increases, which is consistent with the impact of the constraint effect on the *J-R* curve as reported in the literature. Based on the approach suggested by Zhu and Leis (2005, 2006a), and the consideration that a limit number (i.e. four) of experimentally-determined *J-R* curves are available, the following linear regression equations between $J_{0.2}$ ($J_{1.0}$) and the constraint parameter Y were developed based on their values associated

with SEB64, SEB63, SEB43 and SEB42. These regression equations are also shown in Fig. (3.8) through (3.14).

$$J_{0.2} = q_1 Y + q_2 \tag{3.17a}$$

$$J_{1.0} = q_3 Y + q_4 \tag{3.17b}$$

Substituting Eqs. (3.17a) and (3.17b) into (3.15a) and (3.15b) then leads to the following equations for C_1 and C_2 as functions of Y:

$$C_1(Y) = q_3 Y + q_4 \tag{3.18a}$$

$$C_2(Y) = \frac{\ln(q_1 Y + q_2) - \ln(q_3 Y + q_4)}{\ln 0.2} \tag{3.18b}$$

Figure 3.15 depicts C_2 obtained from Eq. (3.18b) as a function of Y. It can be seen that C_2 is approximately a linear function of Y. For simplicity, another linear regression equation was developed for $C_2(Y)$ obtained from Eq. (3.18b), leading to the following approximate expression of $C_2(Y)$:

$$C_2(Y) = q_5 Y + q_6 \tag{3.18c}$$

where the fitting coefficients q_i (i = 1, 2, …6) corresponding to different constraint parameters are tabulated in Table 3.3.

Figures (3.16) through (3.22) depict the constraint-corrected *J-R* curves and the experimentally determined *J-R* curves. For deeply- and medium-cracked specimens, the constraint-corrected *J-R* curves agree well with those obtained from the experiments, as expected. To validate the constraint-corrected *J-R* curves, the *J-R* curves for the two shallow-cracked specimens (SEB25 and SEB24) were predicted from Eq. (3.13) with $C_1(Y)$ and $C_2(Y)$ given by Eqs. (3.18a) and (3.18c) respectively, where the value of the constraint parameter Y was obtained from the 3D FEA. The predicted *J-R* curves were compared with the corresponding experimentally determined *J-R* curves in Figs. (3.16b) through (3.22b). Tables 3.4 and 3.5 show the errors of the *J* values in the predicted *J-R*

curves at different crack extensions for SEB25 and SEB24 specimens, respectively. The error, e, was calculated using the following equation:

$$e = \frac{J_{p\Delta a} - J_{\Delta a}}{J_{\Delta a}} \times 100\% \tag{3.19}$$

where $J_{\Delta a}$ and $J_{p\Delta a}$ denote the J values in the experimentally-determined and the predicted J-R curves at a given crack extension Δa. A positive value of e means overestimation of J, whereas a negative value of e means underestimation of J. Tables 3.4 and 3.5 indicate that the predicted J-R curves for SEB25 and SEB24 underestimate the corresponding actual J values at Δa = 0.2 mm, regardless of the constraint parameter used. For 0.2 mm < $\Delta a \leq$ 0.7 mm, the errors in the predicted J based on all the considered constraint parameters except Q_{HRR} and Q_m are less than or around 10%, whereas the errors in the predicted J at Δa = 0.7 mm are about 14% for the Q_{HRR}- and Q_m-based constraint-corrected J-R curves. For 0.7 mm < $\Delta a \leq$ 1.5 mm, the Q_{BM1}-based constraint-corrected J-R curve results in the most accurate prediction of J, with the maximum error of about 3%; the T_z- and A_2-based constraint-corrected J-R curves lead to maximum errors of predictions of J about 14 and 16%, respectively. On the other than hand, the Q_{HRR}-, Q_{BM2}- and Q_m-based constraint-corrected J-R curves lead to relatively poorly predicted J values for 0.7 mm < $\Delta a \leq$ 1.5 mm, with the maximum errors about 25%. The above results suggest that three constraint parameters, namely Q_{BM1}, T_z and A_2, are adequate for developing the constraint-corrected J-R curve based on SE(B) specimens, whereas Q_{HRR}, Q_{BM2} and Q_m are inadequate for such development. However, this observation is based on a limited number (i.e. six) of specimens, and needs to be further confirmed with more investigations in the future.

To apply the developed constraint-corrected J-R curve to actual pipelines containing cracks, 3D FEA of the pipelines under the applicable loading conditions needs to be carried out to determine the value of the constraint parameter (e.g. Q_{BM1}, h and T_z) at the mid-plane along the crack front. The value of the constraint parameter can then be substituted into the constraint-corrected J-R curve to develop the J-R curve that is

specific for the particular pipeline. This *J-R* curve can then be used to accurately evaluate the structural integrity of the pipeline.

3.5 Conclusions

The constraint- corrected *J-R* curves for X80 grade pipeline steel were developed based on 3D FEA. The constraint parameters for a set of SE(B) specimens reported in the literature were evaluated using 3D large displacement/large strain FEA. The constraint parameters were combined with the experimentally determined *J-R* curves corresponding to medium- and deeply-cracked SE(B) specimens to develop constraint corrected *J-R* curve. Compared with the previous 2D FEA-based studies on constraint-corrected *J-R* curves, the present study can better simulate the actual 3D specimen configuration (such as the presence of side grooves) and test condition (such as the kinematics of the specimen during test). The constraint parameters considered in this study include Q, A_2, h and T_z. The Q parameters investigated in this study include Q_{HRR}, the load-independence corrected Q, Q_m, and bending-corrected Q, Q_{BM1} and Q_{BM2}.

Six side-grooved SE(B) specimens with different crack lengths (a/W) (i.e. a/W = 0.24, 0.25, 0.42, 0.43, 0.63 and 0.64) were modeled in the FEA. The 8-node 3D brick elements with 2×2×2 integration were used. The displacement-controlled loading was applied in the FEA. A blunt crack tip with a radius r_w = 0.003 mm was modeled to facilitate the large-deformation calculation. Two contact rollers were defined to simulate the rollers supporting and loading the specimen.

The average J value over the entire crack front and the local J value at each layer along the crack front were output together with the state of stress ahead of the crack tip at the mid-thickness of the crack front. The distribution of the local J along the crack front was observed to depend on a/W and the loading level. For similar loading levels the distribution of the local J along the crack front tends to be more uniform as a/W increases. For a given a/W ratio, the distribution of local J becomes less uniform as the loading level increases. The distribution of the opening stress at the mid-plane ahead of the crack

tip is largely influenced by a/W. At $r/(J_{mid}/\sigma_0) = 2$ and similar loading levels (e.g. $J_{mid}/b\sigma_0 \approx 0.025$), the difference between the opening stress values corresponding to the HRR solution and FEA results increases as a/W decreases, which reflects a decrease in the constraint level as a/W decreases.

The developed constraint-corrected *J-R* curve was validated using the *J-R* curve obtained from shallow-cracked SE(B) specimens. Among all the constraint parameters investigated in this study, it is observed that the constraint-corrected *J-R* curves developed based on Q_{BM1}, T_z and A_2 lead to reasonably accurate predictions of J for a wide range of crack extensions (0.2 mm < $\Delta a \leq$ 1.5 mm), whereas the parameters Q_{HRR}, Q_{BM2} and Q_m are considered inadequate for developing the constraint-corrected *J-R* curves because the corresponding constraint-corrected *J-R* curves lead to relatively poor predictions of the J values for 0.7 mm < $\Delta a \leq$ 1.5 mm. Further investigations on more SE(B) specimens are needed to confirm this observation.

The approach for constructing the constrain-corrected *J-R* curve presented in this study can be used to develop the structure-specific *J-R* curve based on *J-R* curves obtained from small-scale test specimens. The use of the structure-specific *J-R* curve will improve the accuracy of the integrity assessment of structures such as energy pipelines containing planar defects.

References

ADINA. *Theory and Modeling Guide*, ADINA R. & D. Inc., Watertown, USA; 2012.

Anderson TL. *Fracture Mechanics—Fundamentals and Applications*, Third edition. CRC Press, Boca Raton; 2005.

API. *API Specification 5L: Specification for Line Pipe*, Ed. 45, American Petroleum Institute, Washington, D.C.; 2012.

ASTM. *ASTM E1820-11E2*: *Standard Test Method for Measurement of Fracture Toughness*, ASTM, West Conshohocken, PA; 2013.

ASTM. *ASTM E399-12E1*: *Standard Test Method for Linear-Elastic Plane-Strain Fracture Toughness K_{Ic} of Metallic Materials*, ASTM, West Conshohocken, PA; 2013.

Brocks W, Schmitt W. The Second Parameter in *J-R* curves: Constraint or Triaxiality ?. *Constraint Effects in Fracture Theory and Applications: Second Volume*, *ASTM STP 1244*; 1995;1244:209-31.

Chao YJ, Yang S, Sutton MA. On the Fracture of Solids Characterized by One or Two Parameters: Theory and Practice. *Journal of the Mechanics and Physics of Solids*; 1994;42:629-47.

Chao YJ, Zhang L. Tables of Plane Strain Crack Tip Fields: HRR and Higher Order Terms, *Me-Report,*97-1, Department of Mechanical Engineering, University of South Carolina; 1997.

Chao YJ, Zhu XK. Constraint-Modified *J-R* Curves and Its Applications to Ductile Crack Growth. *International Journal of Fracture Mechanics*; 2000;106:135-60.

Chao YJ, Zhu XK, Kim Y, Lar PS, Pechersky MJ, Morgan MJ. Characterization of Crack-Tip Field and Constraint for Bending Specimens under Large-scale Yielding. *International Journal of Fracture Mechanics*; 2004;127:283-302.

Graba M, Gałkiewicz J. Influence of the Crack Tip Model on Results of the Finite Elements Method. *Journal of Theoretical and Applied Mechanics*; 2007;45(2):225-37.

Guo W. Elastoplastic Three Dimensional Crack Border Field—I. Singular Structure of the Field. *Engineering Fracture Mechanics*; 1993a;46:93-104.

Guo W. Elastoplastic Three Dimensional Crack Border Field—II. Asymptotic Solution for the Field. *Engineering Fracture Mechanics*; 1993b;46:105-13.

Guo W. Elastoplastic Three Dimensional Crack Border Field—III. Fracture Parameters. *Engineering Fracture Mechanics*; 1995;51:51-71.

Joyce JA, Link RE. Effects of Constraint on Upper Shelf Fracture Toughness. *Fracture Mechanics ASTM STP 1256*, ASTM; 1995;26:142-77.

Joyce JA, Link RE. Application of Two-parameter Elastic-plastic Fracture Mechanics to Analysis of Structures. *Engineering Fracture Mechanics*; 1997;57:431-46.

Kim YJ, Kim JS, Cho SM, Kim YJ. 3-D Constraint Effects on *J* Testing and Crack Tip Constraint in M(T), SE(B), SE(T) and C(T) Specimens: Numerical Study. *Engineering Fracture Mechanics*; 2004;71:1203-18.

Kulka RS, Sherry AH. Fracture Toughness Evaluation in C(T) Specimens with Reduced Out-of-plane Constraint. *ASME 2012 Pressure Vessels & Piping Conference* (PVP-2012). July 15–19th, 2012, Toronto, Canada; 2012. p. PVP2012-78751.

Lam PS, Chao YJ, Zhu XK. Kim Y, Sindelar RL. Determination of Constraint-Modified *J-R* Curves For Carbon Steel Storage Tanks. *ASME Journal of Pressure Vessel Technology*; 2003;125:136-42.

Laukkanen A, Nevasmaa P, Keinänen H, Wallin K. Fracture Toughness Transferability Study between the Master Curve Method and a Pressure Vessel Nozzle Using Local Approach. *ASME, Pressure Vessels and Piping Division (Publication) PVP, Application of Fracture Mechanics in Failure Assessment*; 2003;462:155-64.

Minami F, Toyoda M. Evaluation of Fracture Toughness Results and Transferability to Fracture Assessment of Welded Joints. *ASTM Special Technical Publication*; 1997;1332:315-40.

O'Dowd NP, Shih CF. Family of Crack-tip Fields Characterized by a Triaxiality Parameter—I. Structure of Fields. *Journal of the Mechanics and Physics of Solids*; 1991;39(8):989-1015.

O'Dowd NP, Shih CF. Family of Crack-tip Fields Characterized by a Triaxiality

Parameter—II. Fracture applications. *Journal of the Mechanics and Physics of Solids*; 1992;40:939-63.

O'Dowd NP, Shih CF. Two-parameter Fracture Mechanics: Theory and Applications. Fracture Mechanics. *ASTM STP 1207, American Society for Testing and Materials, Philadelphia*; 1994;24:21-47.

Ruggieri C, Gao X, Dodds RH. Transferability of Elastic-plastic Fracture Toughness Using the Weibull Stress Approach: Significance of Parameter Calibration. *Engineering Fracture Mechanics*; 2000;67(2):101-17.

Scibetta M, Schuurmans, J, Lucon E. Experimental Study of the Fracture Toughness Transferability to Pressurized Thermal Shock Representative Loading Conditions. *ASTM Special Technical Publication*; 2009;1508:499-517.

Shen G, Tyson WR, Glover A, Horsley D. Constraint Effects On Linepipe Toughness. *Proceedings of the 4th International Conference on Pipeline Technology*, May 9–13, Ostend, Belgium; 2004;2:703-20.

Wang ZX, Lam PS, Chao YJ. Quantification of Ductile Crack Growth in 18G2A Steel at Different Constraint Levels. *ASME Journal of Pressure Vessel Technology*; 2009;86:221-7.

Yang S, Chao YJ, Sutton MA. Complete Theoretical Analysis for Higher Order Asymptotic Terms and the HRR Zone at a Crack Tip for Mode I and Mode II Loading of a Hardening Material. *Acta Mechanica*; 1993a;98:79-98.

Yang S, Chao YJ, Sutton MA. Higher-order Asymptotic Fields in a Power-law Hardening Material. *Engineering Fracture Mechanics*; 1993b;45:1-20.

Zhu XK, Jang SK, *J-R* Curves Corrected by Load-Independent Constraint Parameter in Ductile Crack Growth. *Engineering Fracture Mechanics*; 2001;68:285-301.

Zhu XK, Leis BN, Joyce JA. Constraint Corrected *J-R* Curves and Its Application to Fracture Assessment for X80 Pipelines. *Journal of ASTM International*; 2005;3(6):1-17.

Zhu XK, Leis BN, Joyce JA. Application of Constraint Corrected *J-R* Curves to Fracture Analysis of Pipelines. *Journal of Pressure Vessel Technology*; 2006a;128:581-9.

Zhu XK, Leis BN, Joyce JA. Bending Modified *J–Q* Theory and Crack-tip Constraint Quantification. *International Journal of Fracture*; 2006b;141:115-34.

Zhu XK, Joyce JA. Review of Fracture Toughness (*G*, *K*, *J*, *CTOD*, CTOA) Testing and Standardization. *Engineering Fracture Mechanics*; 2012;85:1-46.

Table 3.1: Parameters of the experimental *J-R* curve for SE(B) specimens

Specimen ID	a/W	C_1 (N/mm)	C_2	$J_{0.2}$ (N/mm)	$J_{1.0}$ (N/mm)
SEB24	0.240	1200	0.666	416	1200
SEB25	0.250	1190	0.654	414	1190
SEB42	0.420	1000	0.761	294	1000
SEB43	0.430	1110	0.688	368	1110
SEB63	0.630	678	0.621	250	678
SEB64	0.640	758	0.583	297	757

Table 3.2: Constraint parameters for SE(B) specimens

Specimen ID	SEB64	SEB63	SEB43	SEB42	SEB25	SEB24
$J_{0.2}$ (N/mm)	297	250	368	294	414	416
$J_{1.0}$ (N/mm)	757	678	1110	1000	1190	1200
Q_{HRR}	-0.303	-0.192	-0.507	-0.379	-0.703	-0.718
Q_m	-0.233	-0.149	-0.382	-0.290	-0.525	-0.536
Q_{BM1}	0.954	0.675	0.218	0.264	-0.020	-0.037
Q_{BM2}	0.731	0.524	0.164	0.202	-0.015	-0.028
A_2	-0.156	-0.122	-0.200	-0.176	-0.236	-0.238
h	2.22	2.37	1.89	2.00	1.66	1.65
T_Z	0.359	0.372	0.303	0.323	0.277	0.276

Table 3.3: Coefficients q_i for the constraint-corrected *J-R* curve

	q_1 (N/mm)	q_2 (N/mm)	q_3 (N/mm)	q_4 (N/mm)	q_5	q_6
Q_{HRR}	-353	180	-1480	378	-0.317	0.554
Q_m	-477	177	-2000	361	-0.436	0.549
Q_{BM1}	-101	343	-657	1150	-0.267	0.770
Q_{BM2}	-323	287	-1670	812	-0.516	0.638
A_2	-1380	77.0	-5890	76.0	-1.40	0.433
h	-219	763	-1050	3090	-0.290	1.27
T_Z	-1340	757	-6390	3050	-1.75	1.25

Table 3.4: Error of the predicted *J-R* curve for SEB25

		Δa (mm)					
		0.2	0.5	0.7	1.0	1.2	1.5
Error, e (%)	Q_{HRR}	-2.2	9.5	14	19	22	25
	Q_m	-2.6	9.1	14	19	22	25
	Q_{BM1}	-19	-9.8	-6.1	-1.9	0.23	3.0
	Q_{BM2}	-9.7	5.2	11	18	22	26
	A_2	-7.4	2.5	6.4	11	13	16
	h	-8.7	3.4	8.2	14	16	20
	T_Z	-10	-0.11	3.9	8.3	11	14

Table 3.5: Error of the predicted *J-R* curve for SEB24

		Δa (mm)					
		0.2	0.5	0.7	1.0	1.2	1.5
Error, e (%)	Q_{HRR}	-1.7	9.8	14	19	22	25
	Q_m	-2.2	9.3	14	19	22	25
	Q_{BM1}	-19	-10	-6.7	-2.7	-0.65	2.0
	Q_{BM2}	-9.5	5.3	11	18	22	26
	A_2	-7.2	2.4	6.2	10	13	15
	h	-8.5	3.3	7.9	13	16	19
	T_Z	-10	-0.58	3.2	7.4	9.7	12

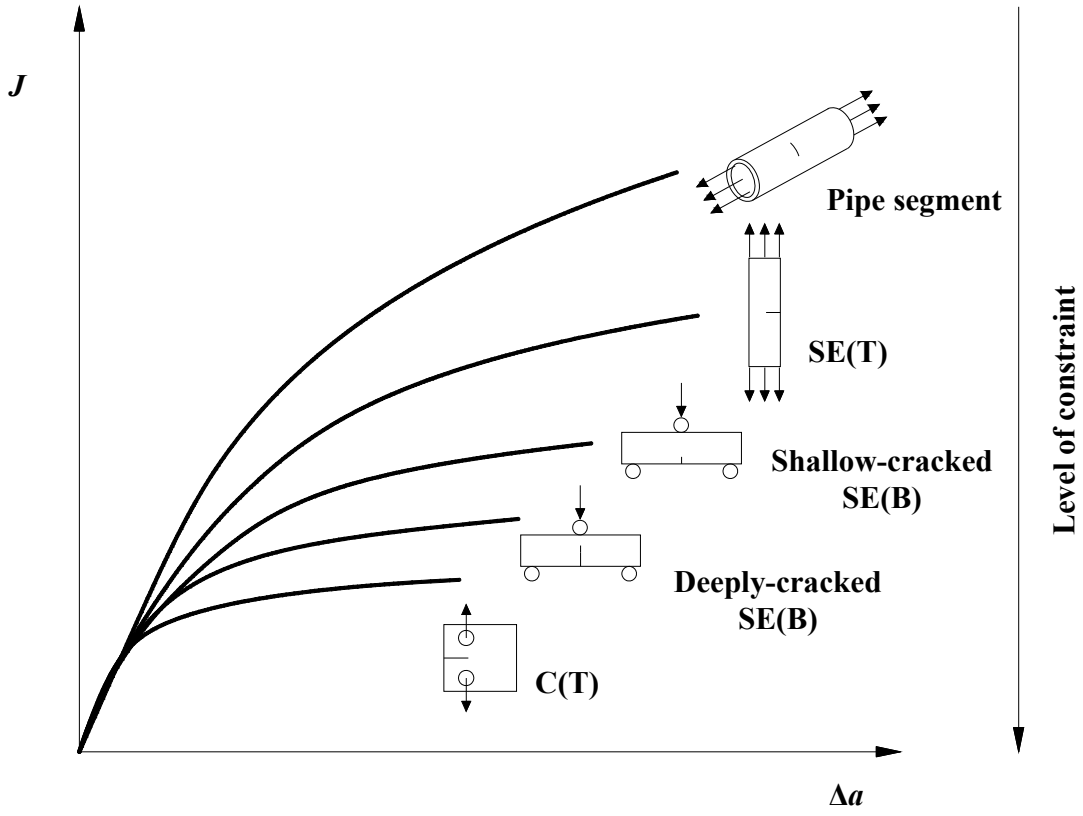

Figure 3.1: Typical *J-R* curves from different types of specimens

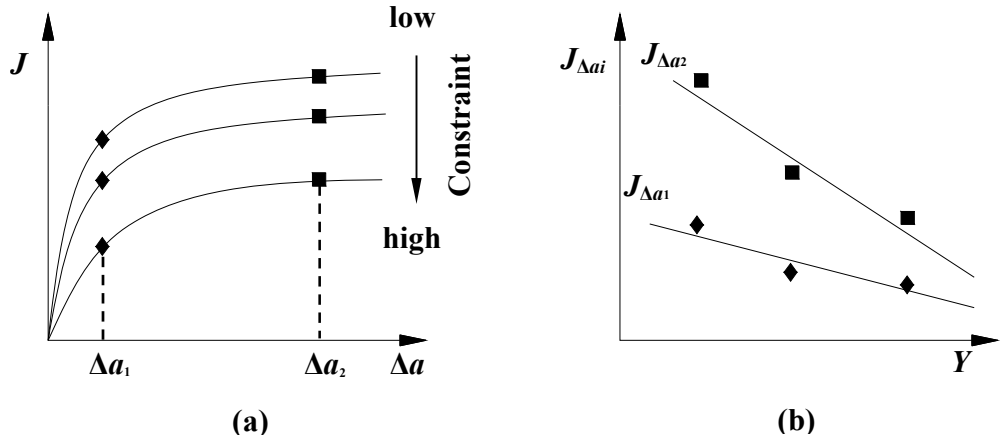

Figure 3.2: Analysis procedures for constructing the constraint-corrected *J-R* curves

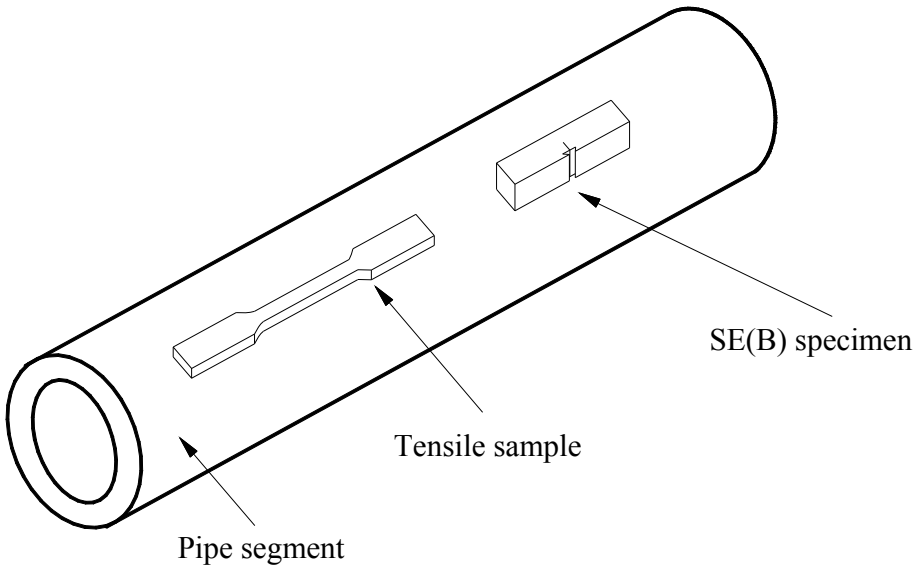

Figure 3.3: Orientations and Locations of SE(B) specimens and tensile sample

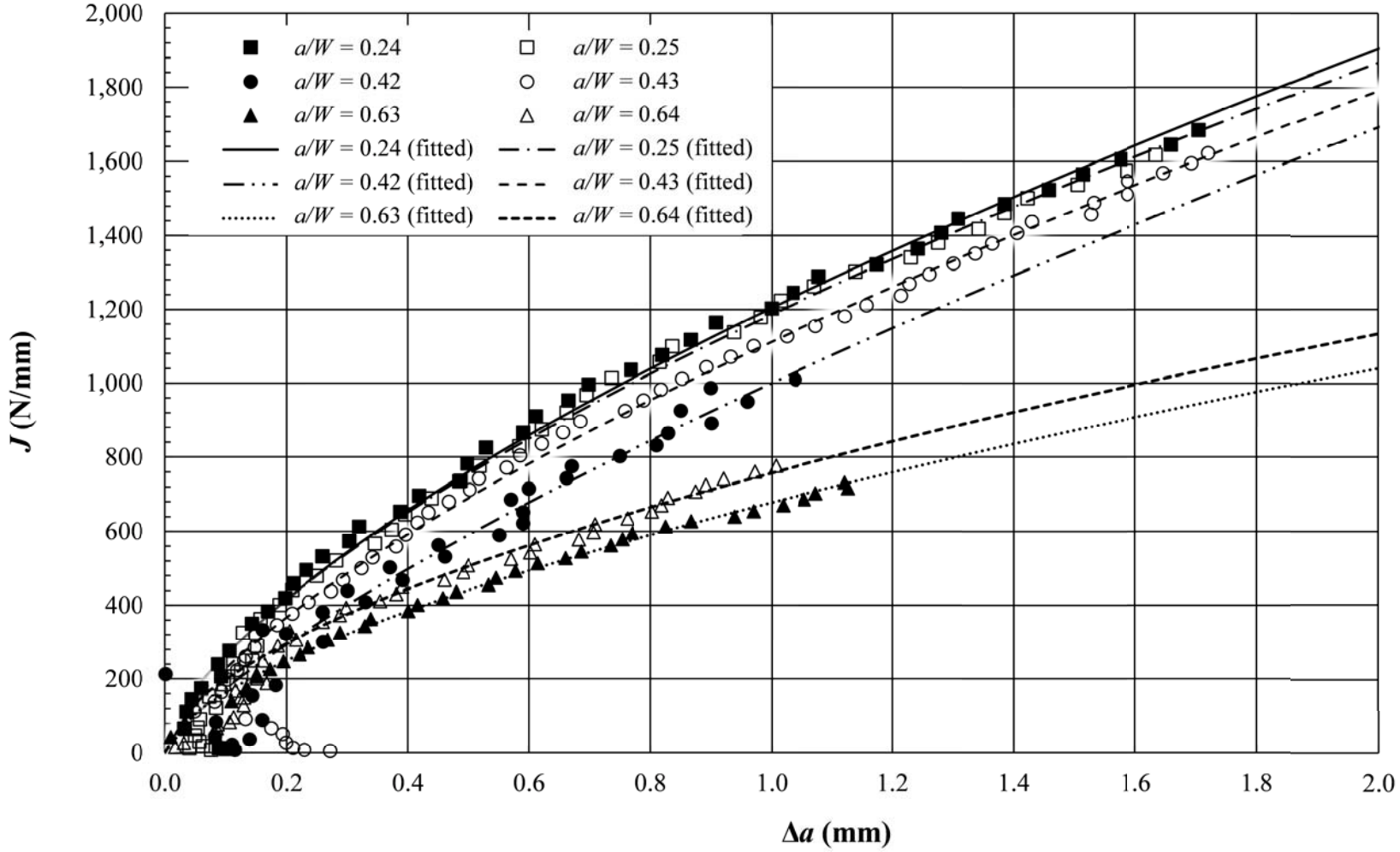

Figure 3.4: Experimentally determined *J-R* curves for SE(B) specimens (Shen et al., 2004)

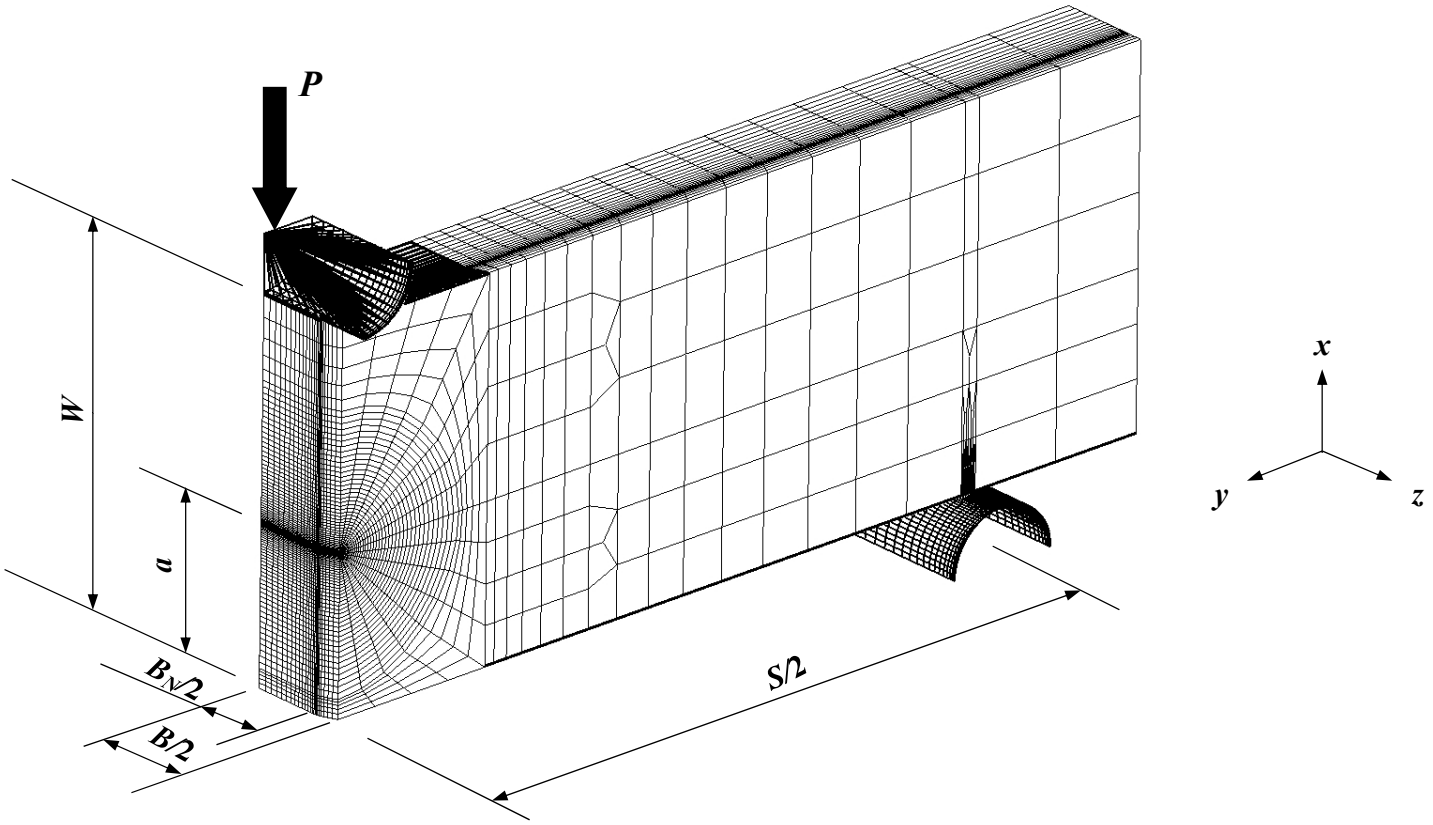

Figure 3.5: FEA model for SE(B) specimen with a/W= 0.42

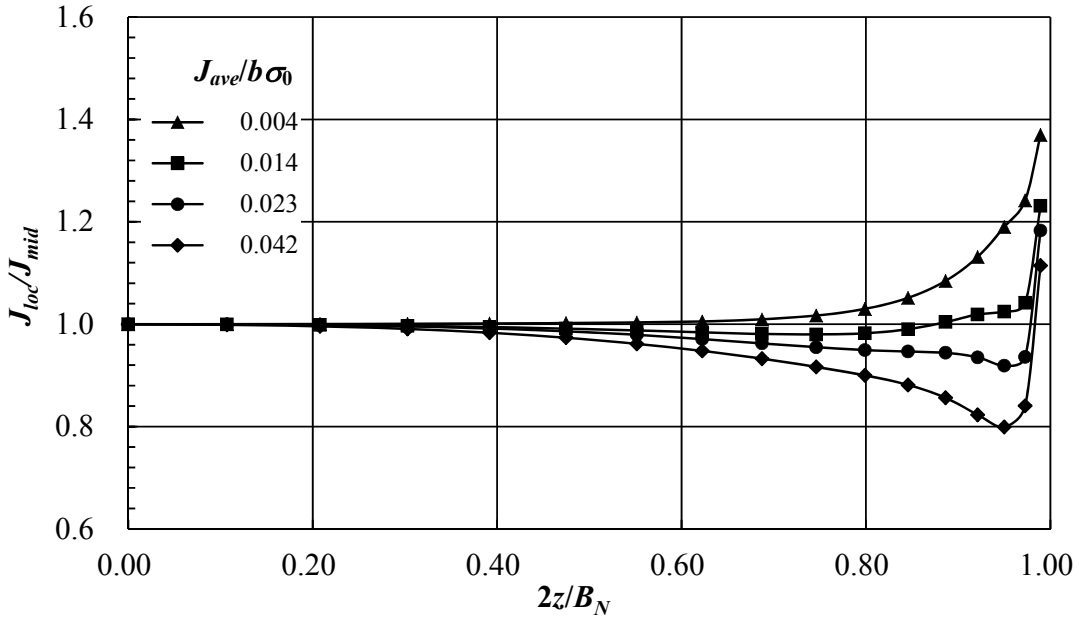

(a) a/W= 0.64

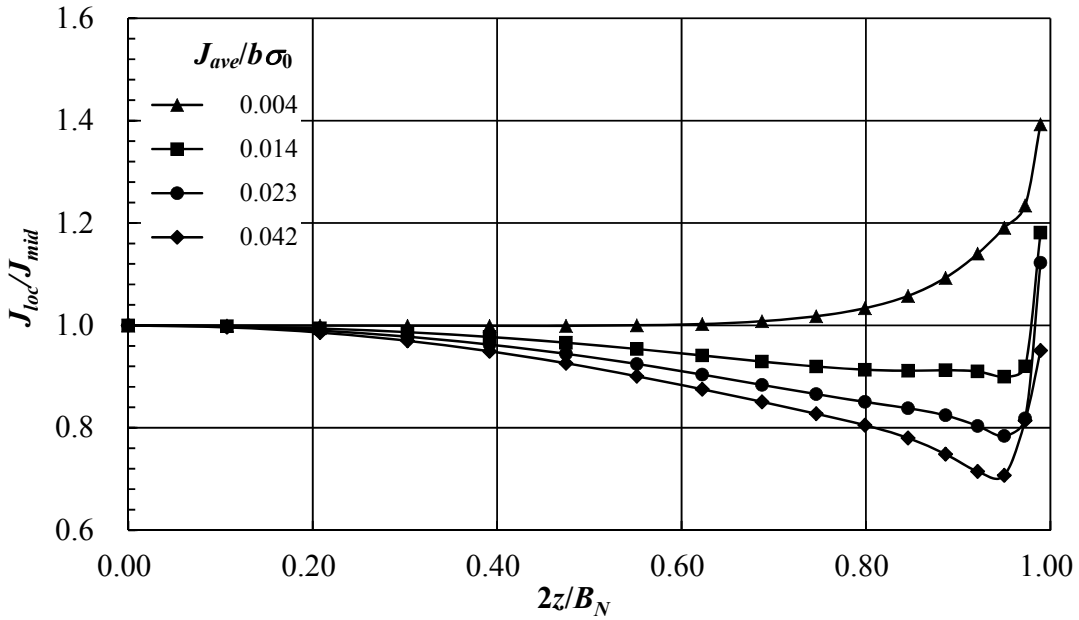

(b) a/W= 0.42

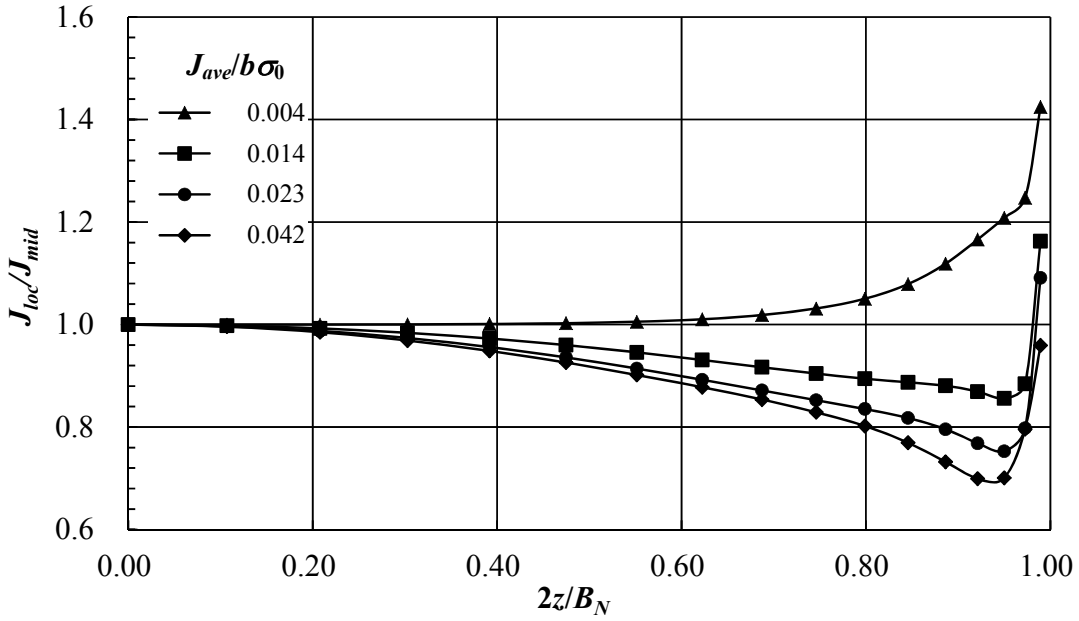

(c) a/W= 0.24

Figure 3.6: Distributions of the local J along the crack front for SE(B) specimens

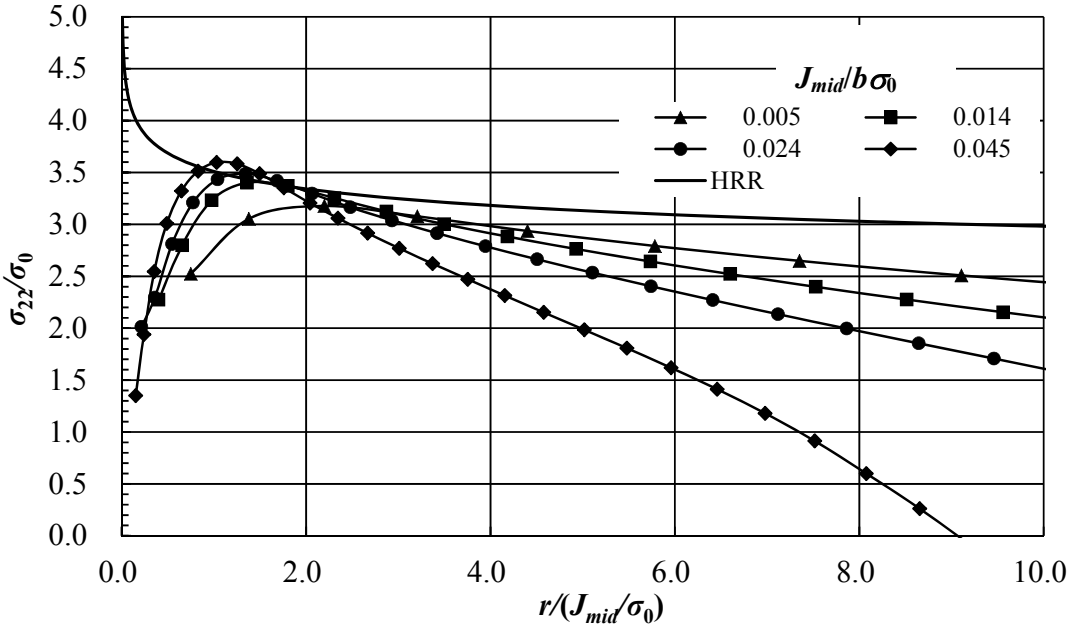

(a) a/W= 0.64

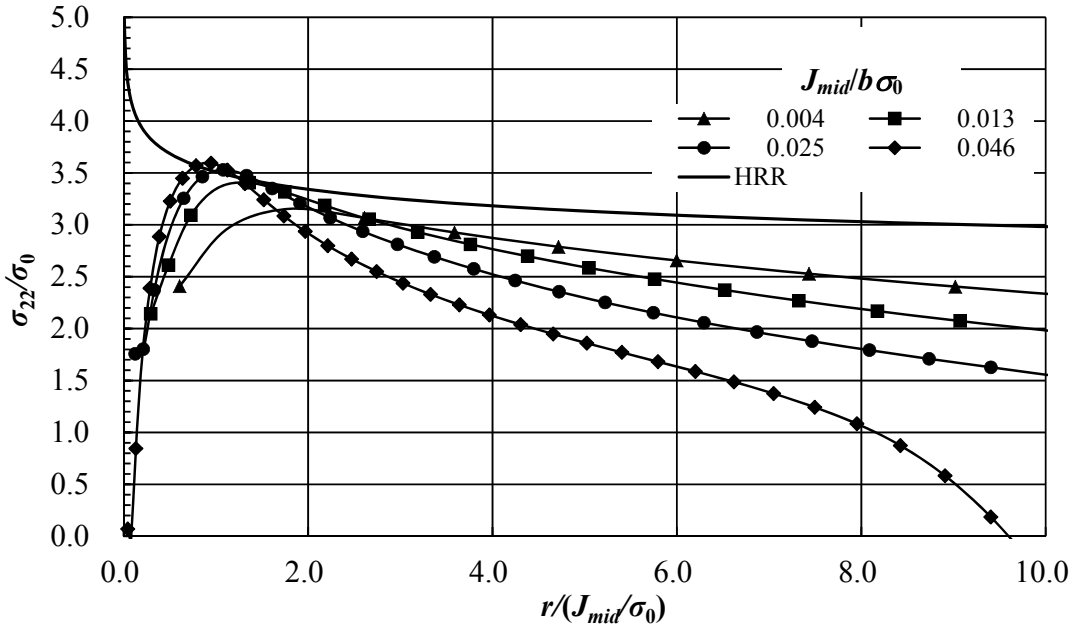

(b) a/W= 0.42

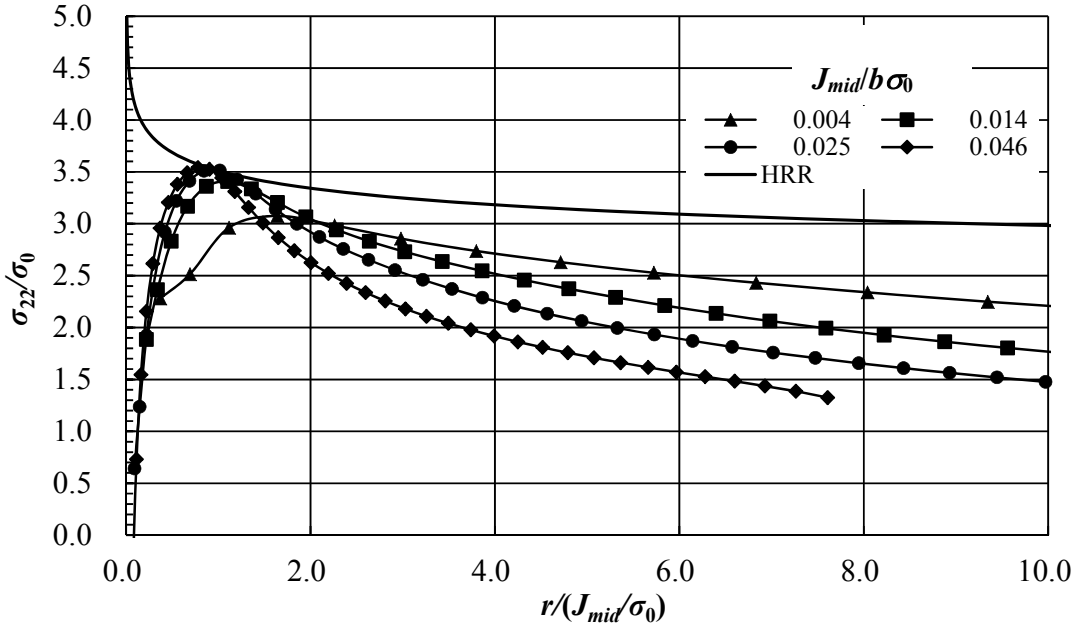

(c) a/W= 0.24

Figure 3.7: Distributions of the crack opening stress as a function of distance from the crack tip for SE(B) specimens

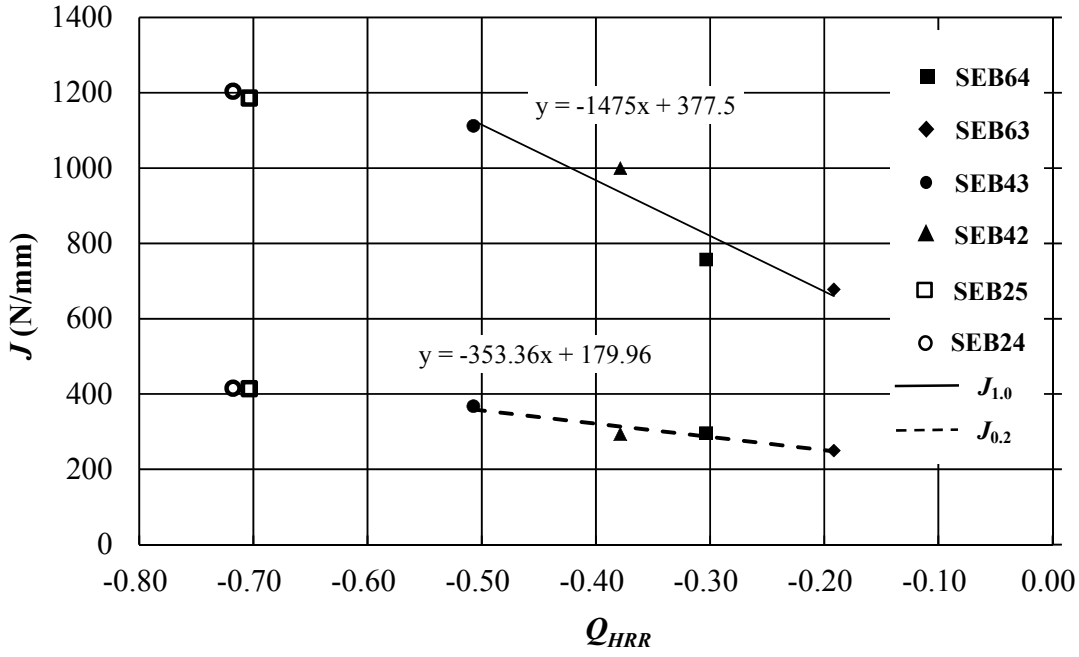

Figure 3.8: Variation of $J_{0.2}$ and $J_{1.0}$ with Q_{HRR}

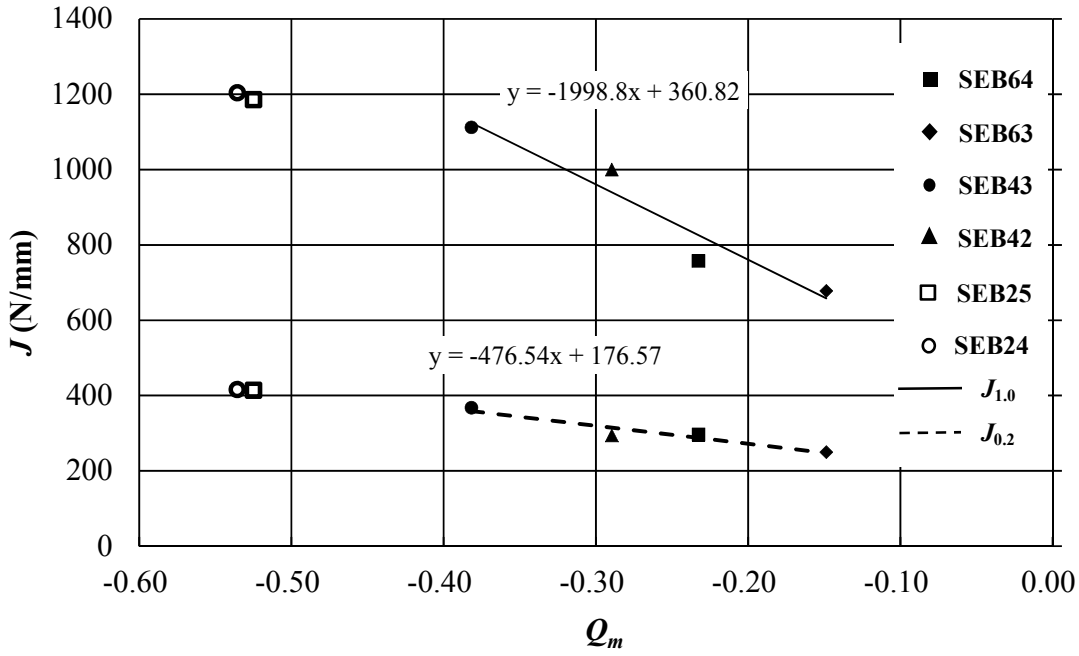

Figure 3.9: Variation of $J_{0.2}$ and $J_{1.0}$ with Q_m

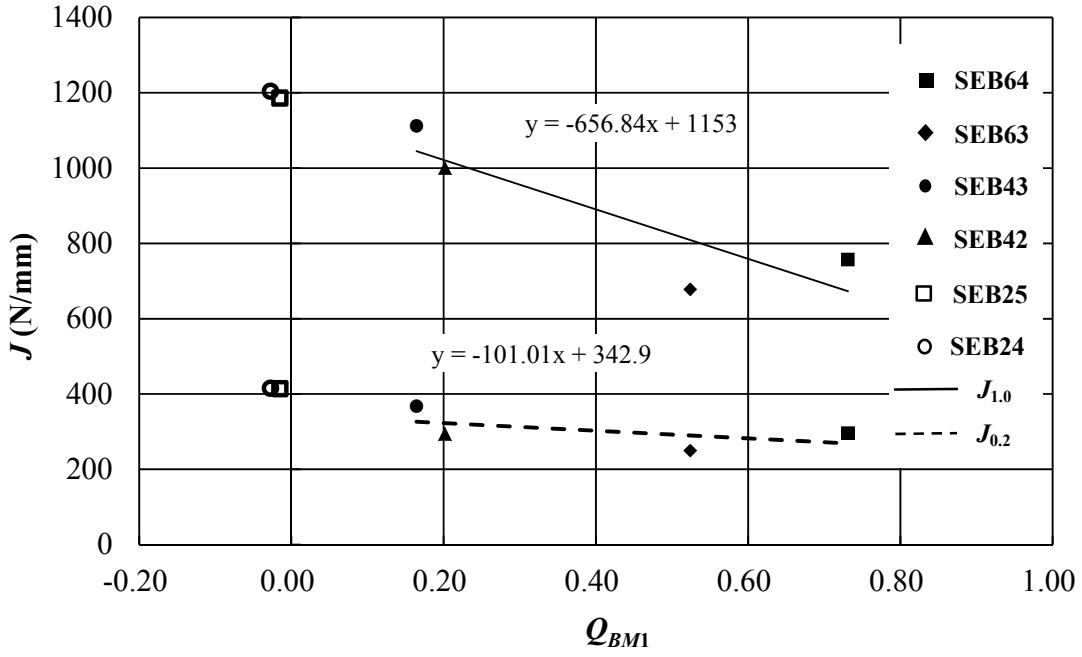

Figure 3.10: Variation of $J_{0.2}$ and $J_{1.0}$ with Q_{BM1}

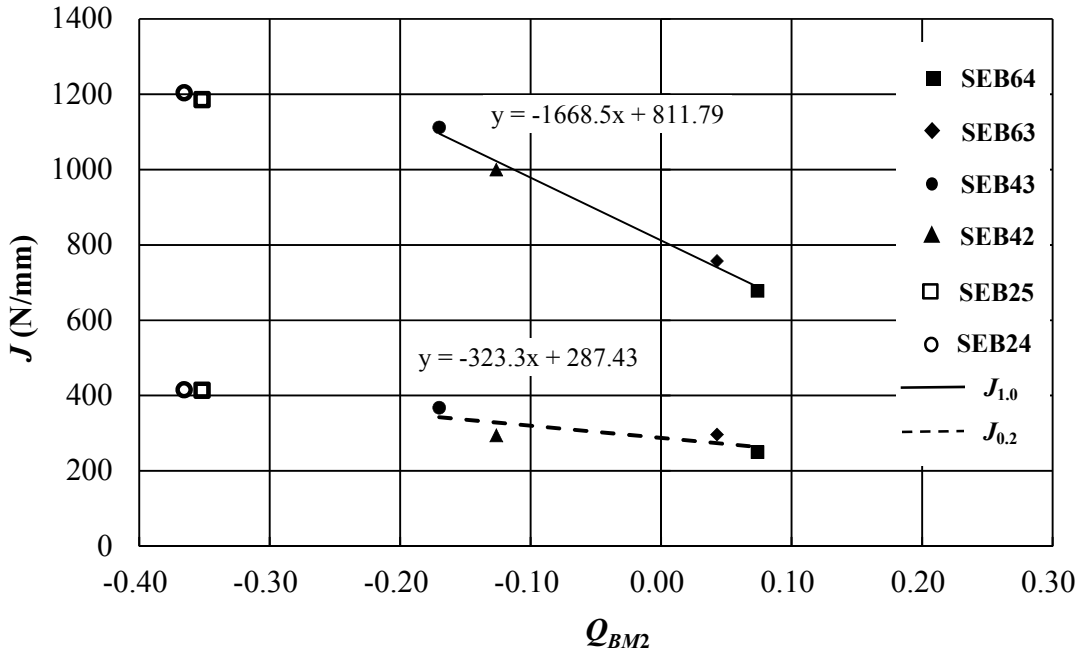

Figure 3.11: Variation of $J_{0.2}$ and $J_{1.0}$ with Q_{BM2}

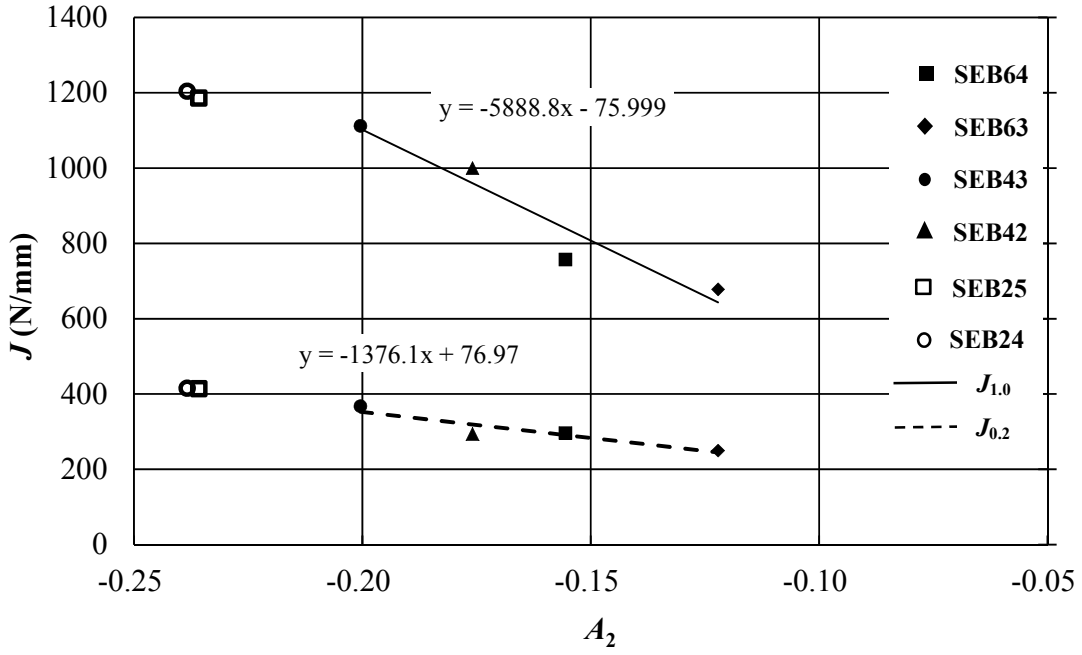

Figure 3.12: Variation of $J_{0.2}$ and $J_{1.0}$ with A_2

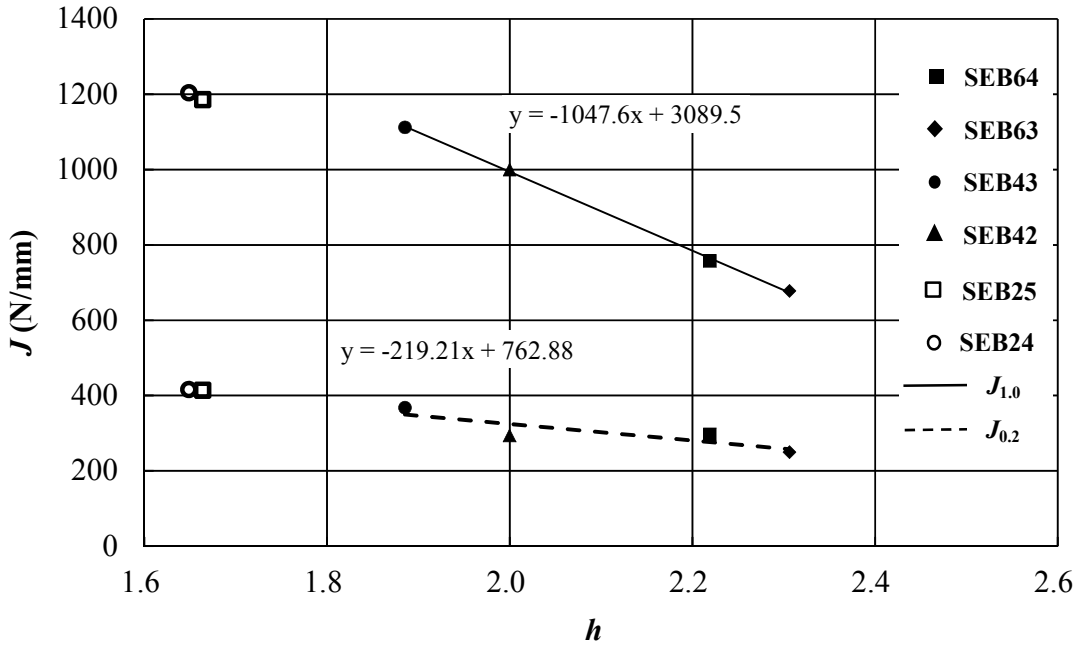

Figure 3.13: Variation of $J_{0.2}$ and $J_{1.0}$ with h

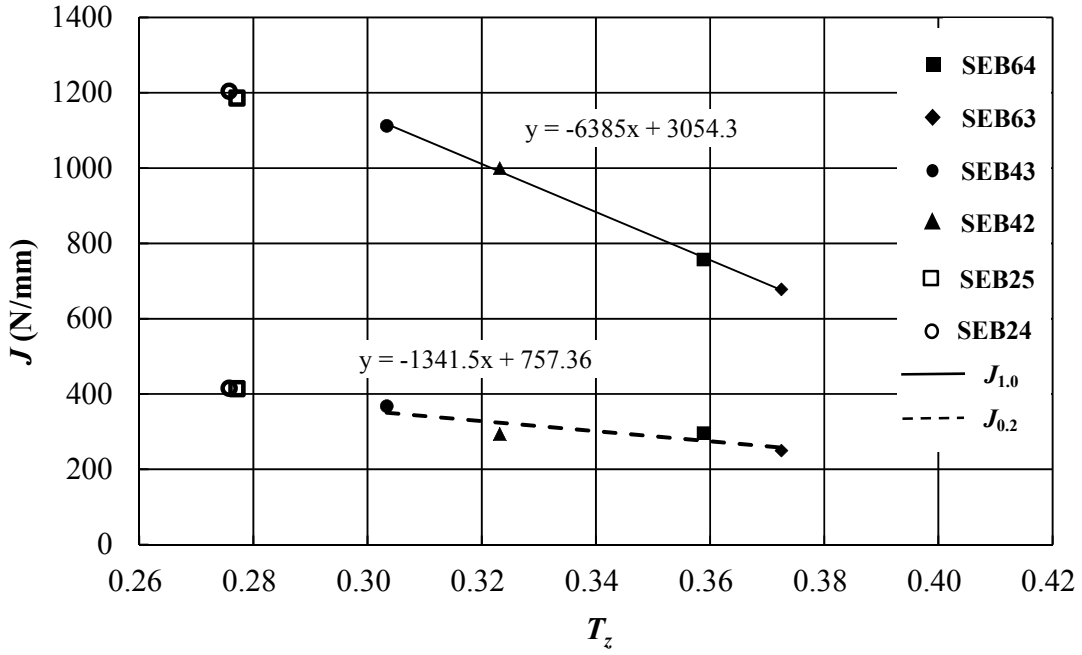

Figure 3.14: Variation of $J_{0.2}$ and $J_{1.0}$ with T_z

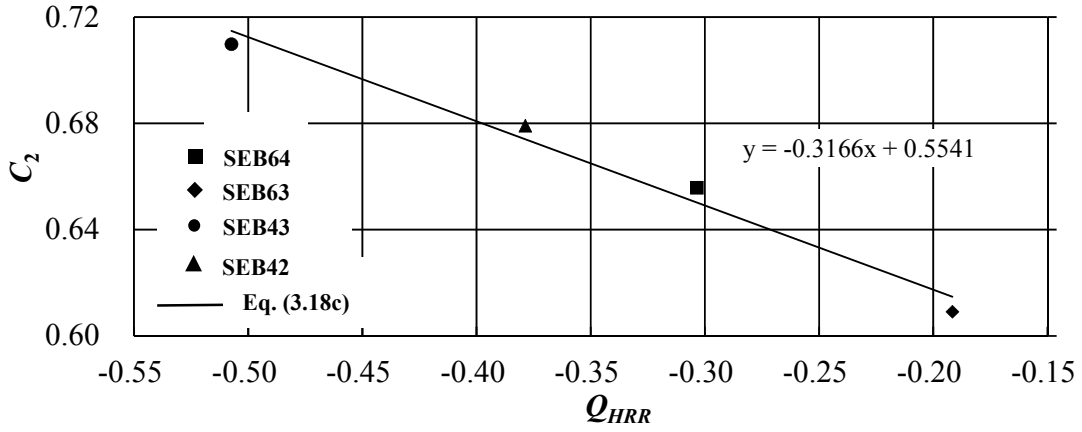

(a) C_2 vs. Q_{HRR}

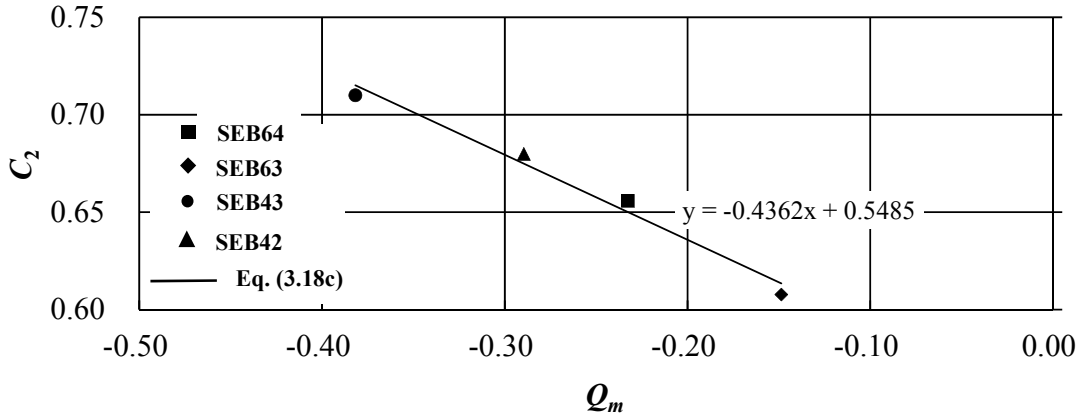

(b) C_2 vs. Q_m

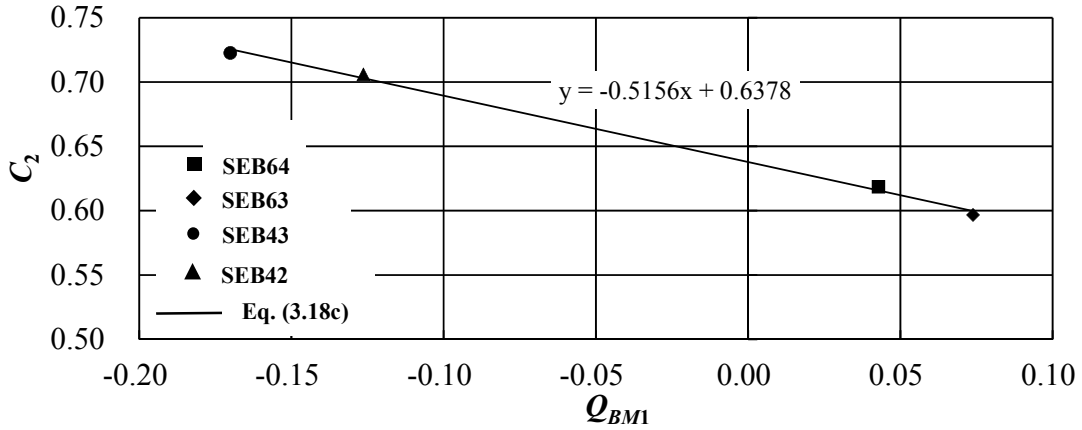

(c) C_2 vs. Q_{BM1}

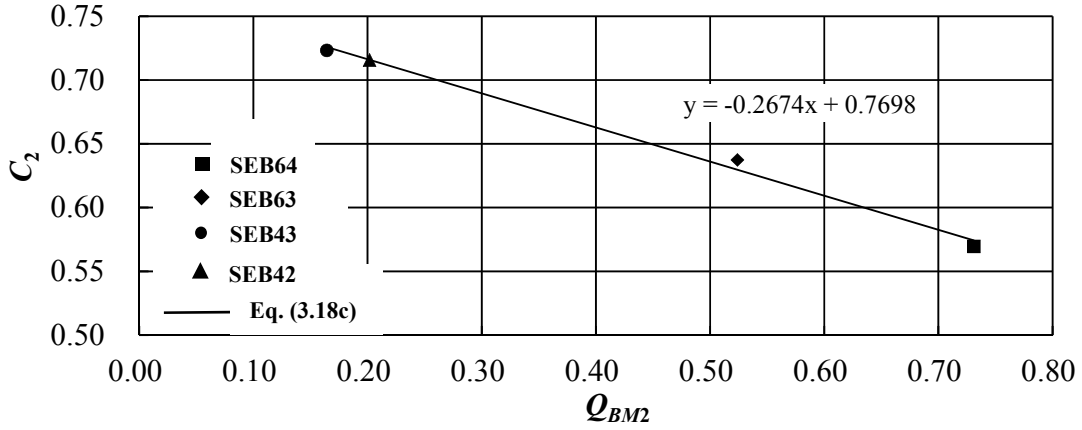

(d) C_2 vs. Q_{BM2}

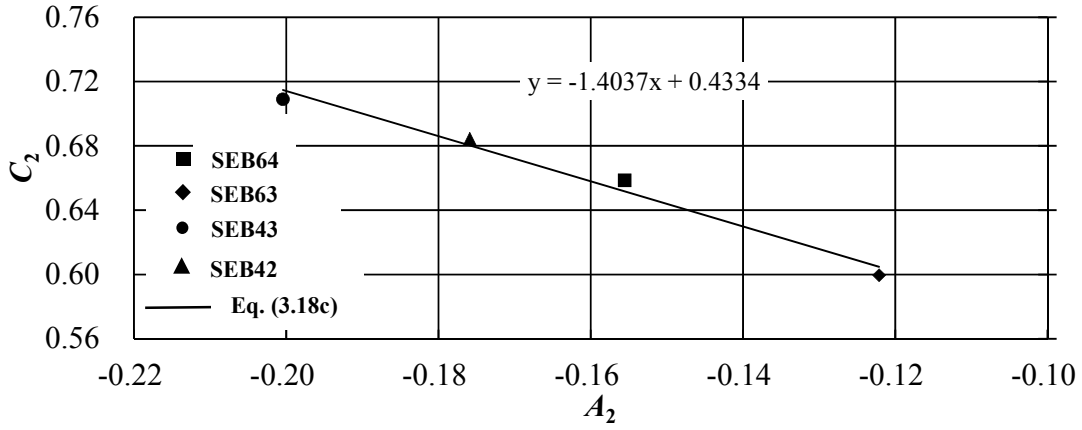

(e) C_2 vs. A_2

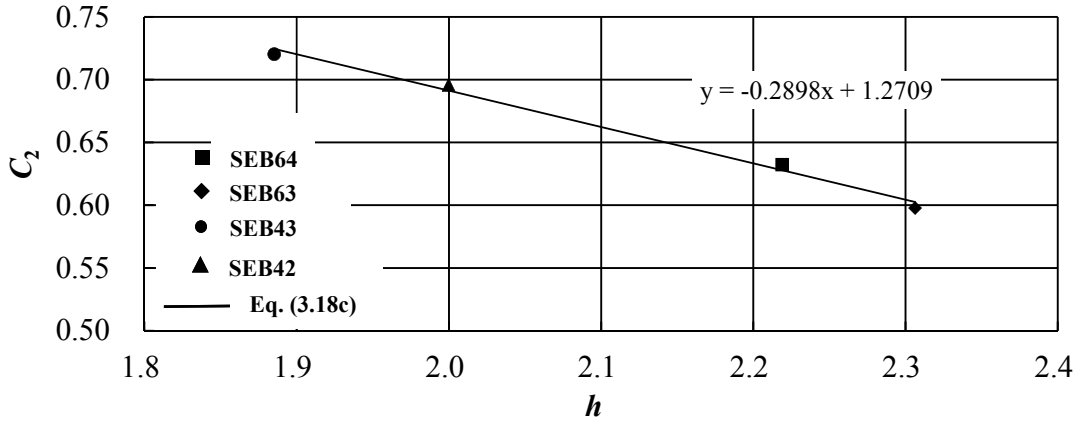

(f) C_2 vs. h

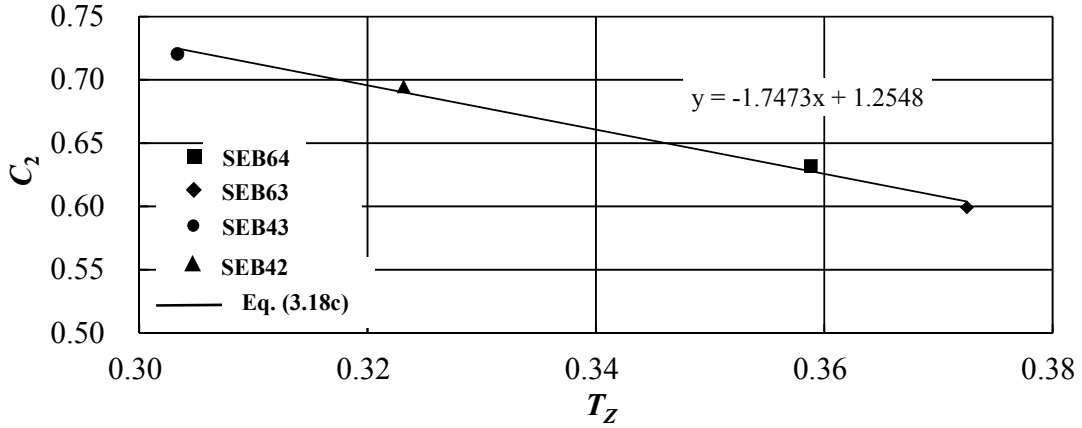

(g) C_2 vs. T_Z

Figure 3.15: C_2 obtained in Eq. (3.18b) as a function of constraint parameter

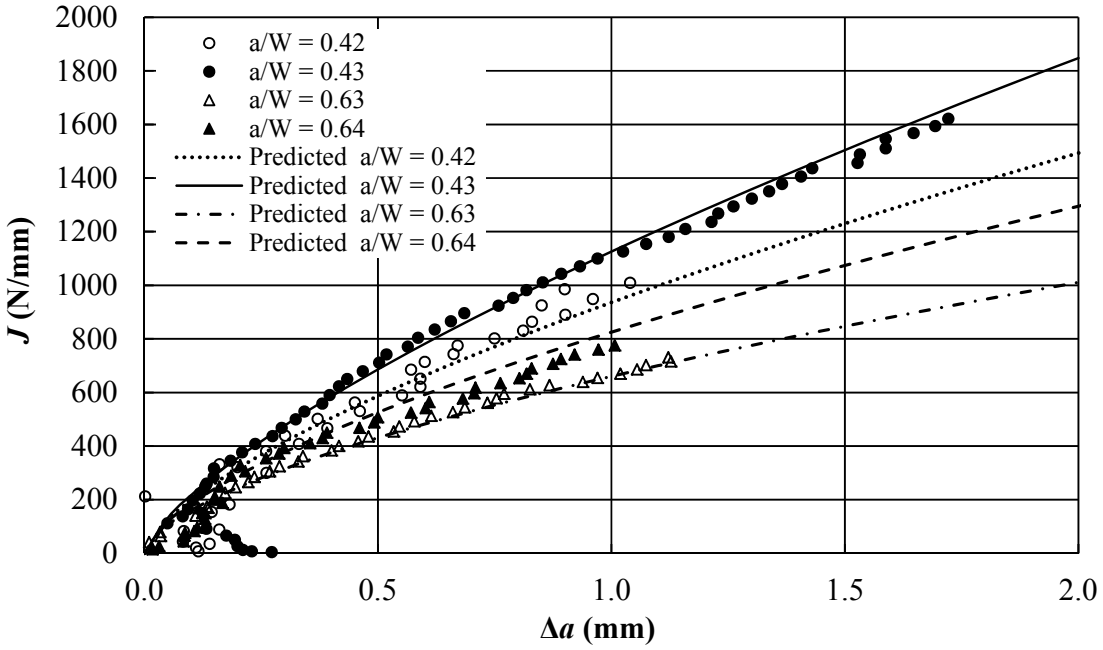

(a) Deeply- and medium-cracked specimens

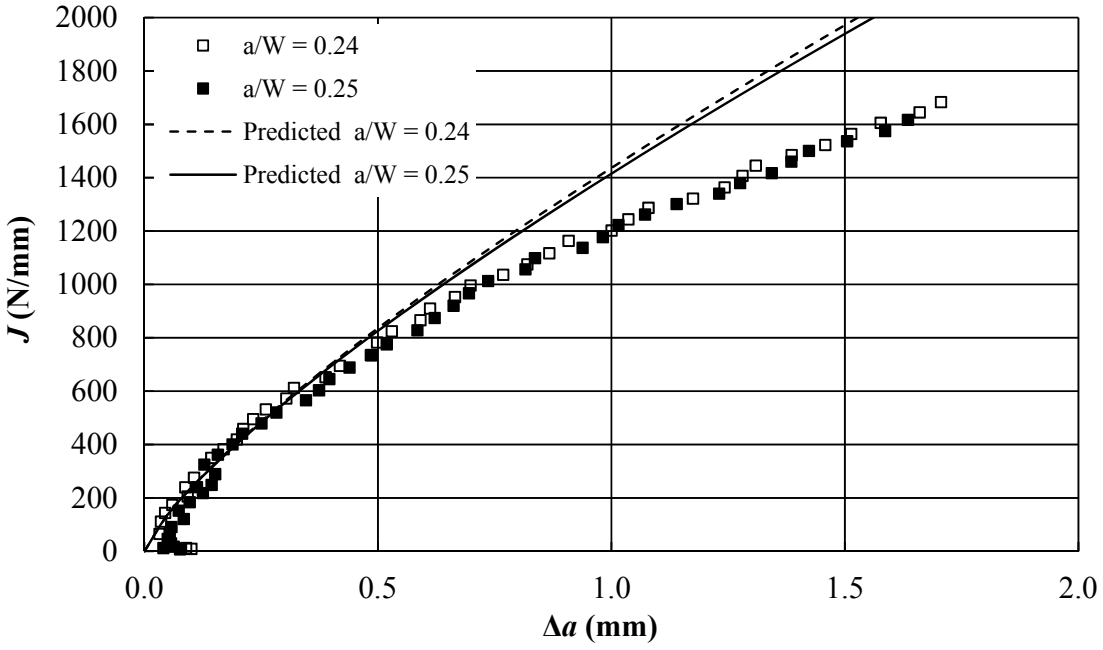

(b) Shallow-cracked specimens

Figure 3.16: Constraint-corrected *J*-R curves for SE(B) specimens based on Q_{HRR}

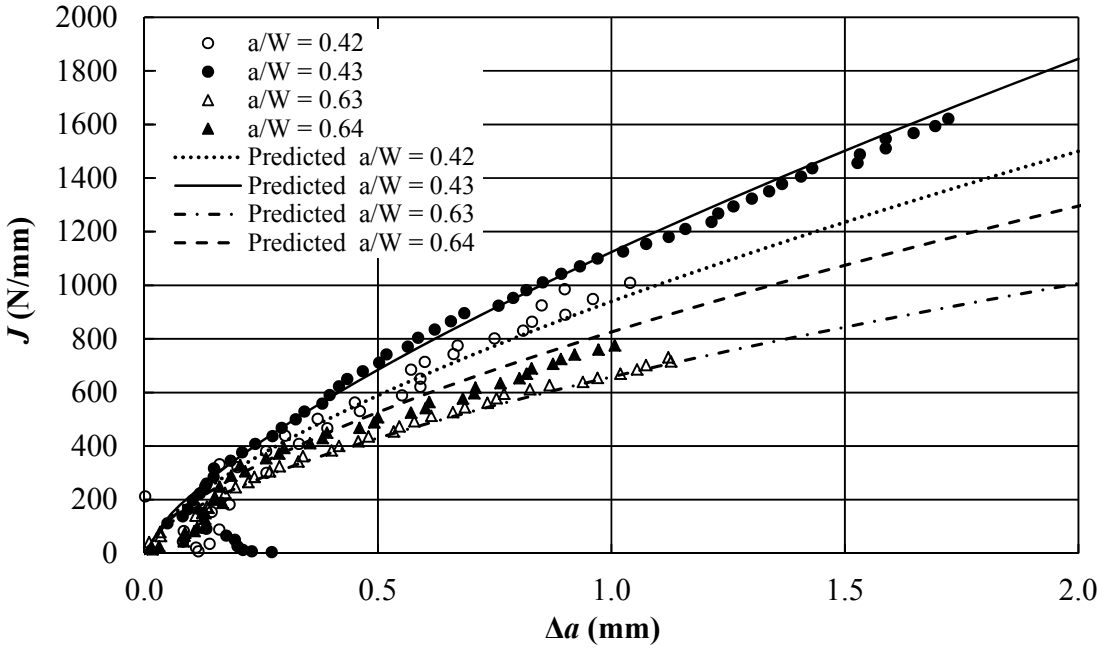

(a) Deeply- and medium-cracked specimens

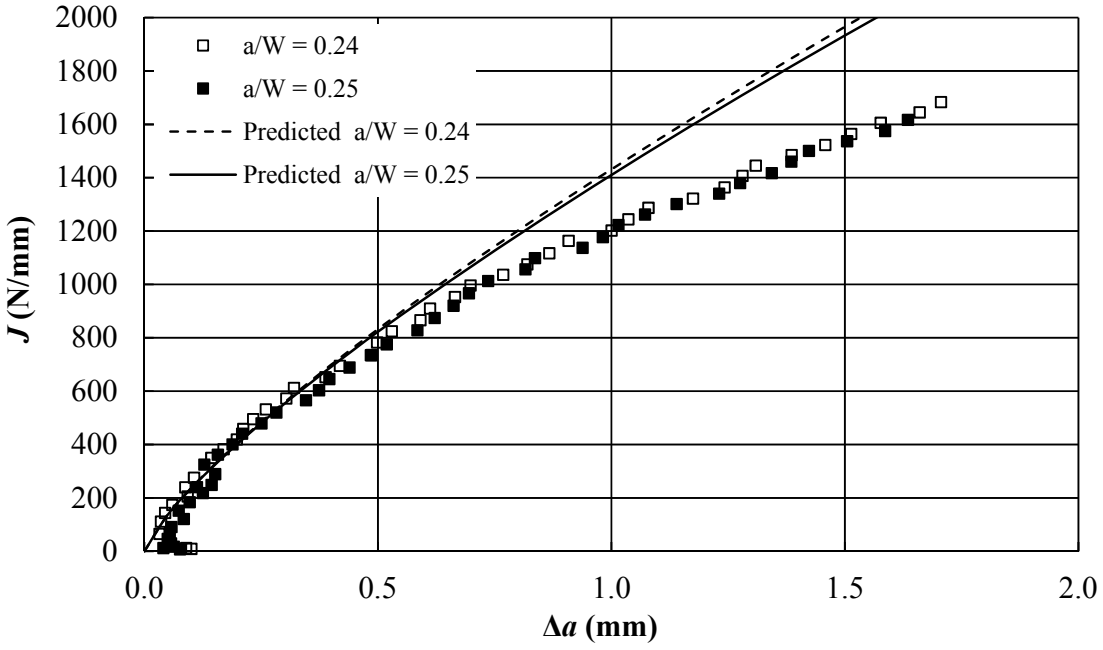

(b) Shallow-cracked specimens

Figure 3.17: Constraint-corrected *J*-R curves for SE(B) specimens based on Q_m

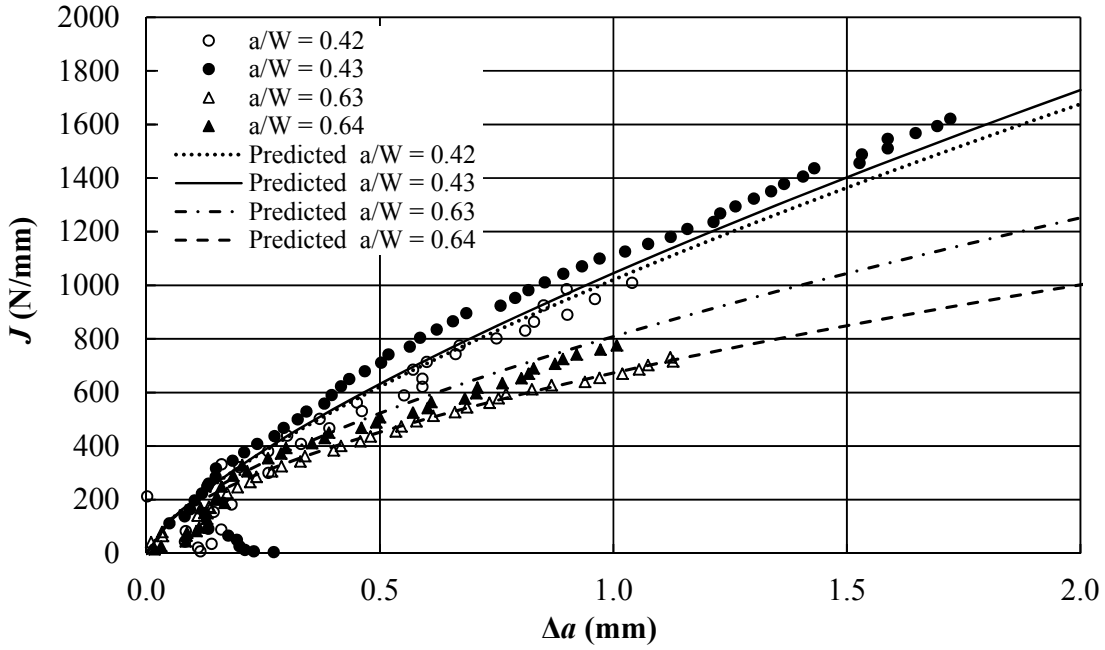

(a) Deeply- and medium-cracked specimens

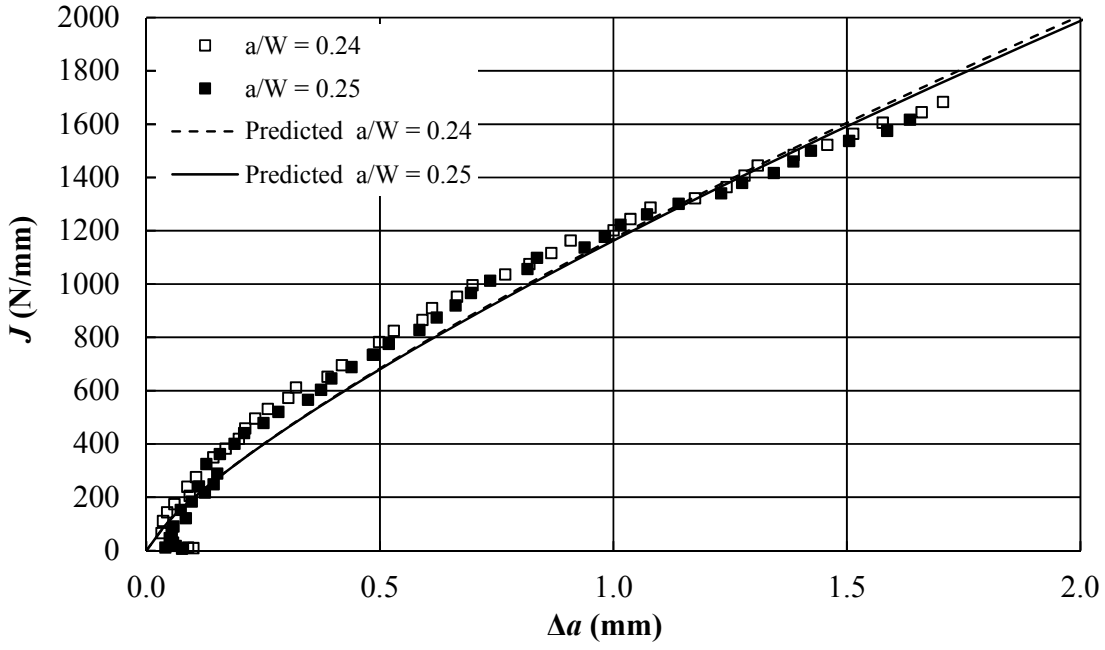

(b) Shallow-cracked specimens

Figure 3.18: Constraint-corrected *J*-R curves for SE(B) specimens based on Q_{BM1}

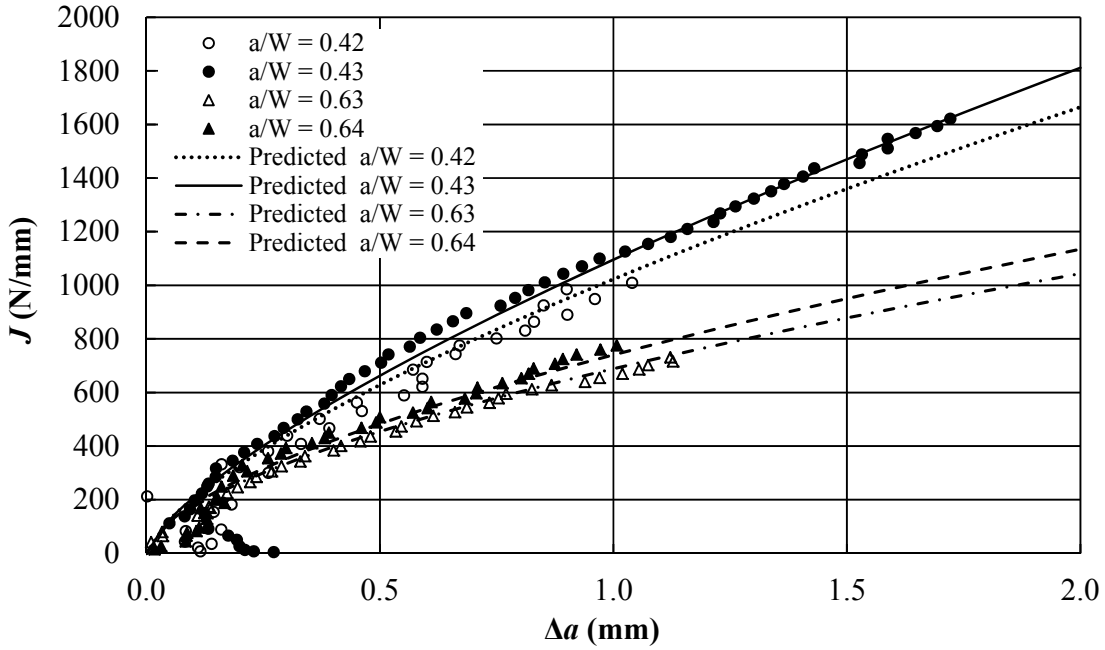

(a) Deeply- and medium-cracked specimens

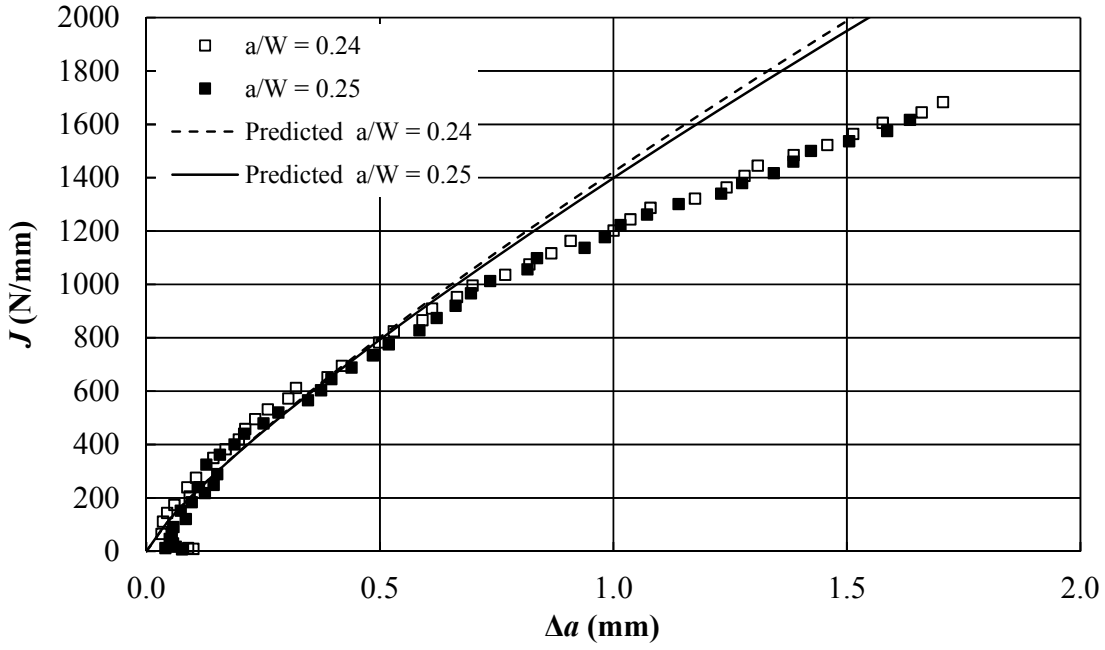

(b) Shallow-cracked specimens

Figure 3.19: Constraint-corrected *J*-R curves for SE(B) specimens based on Q_{BM2}

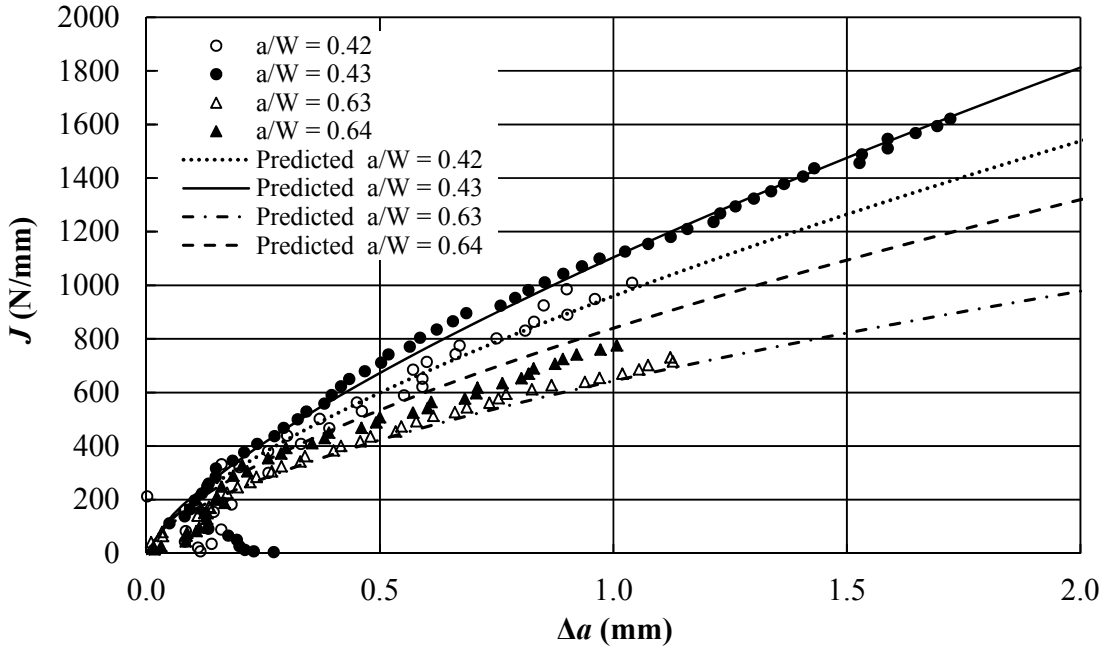

(a) Deeply- and medium-cracked specimens

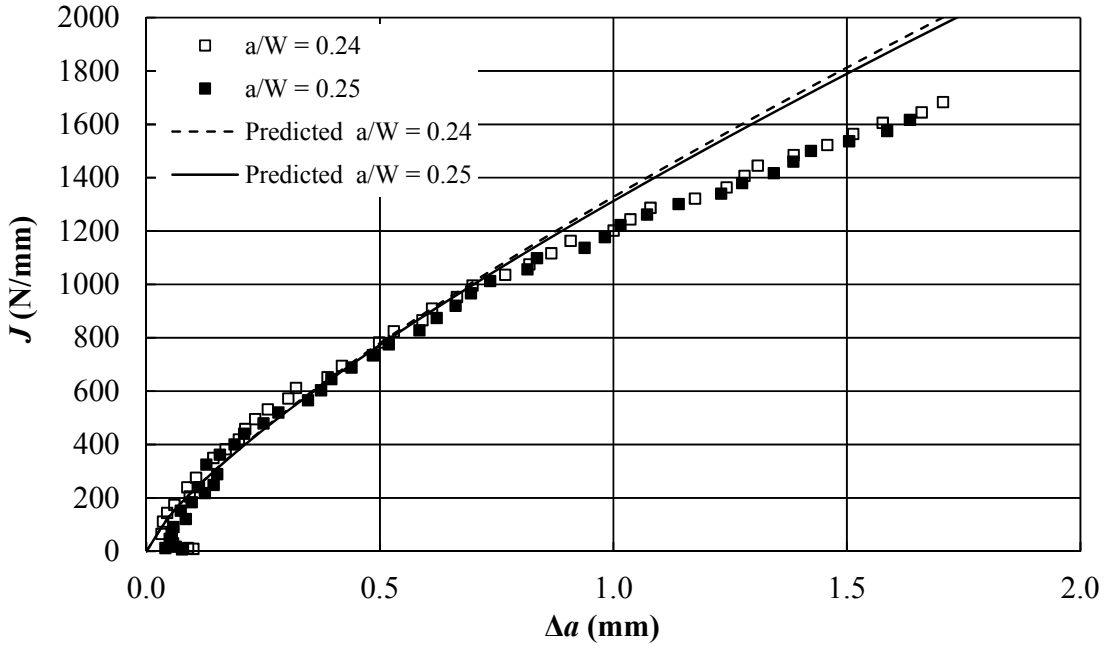

(b) Shallow-cracked specimens

Figure 3.20: Constraint-corrected *J*-R curves for SE(B) specimens based on A_2

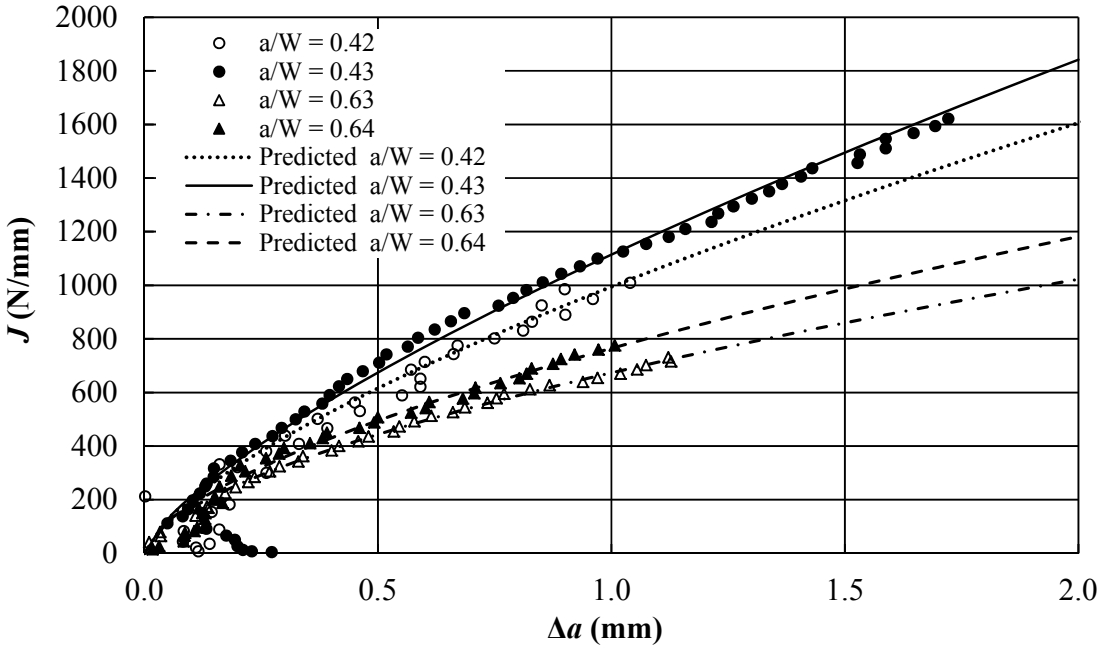

(a) Deeply- and medium-cracked specimens

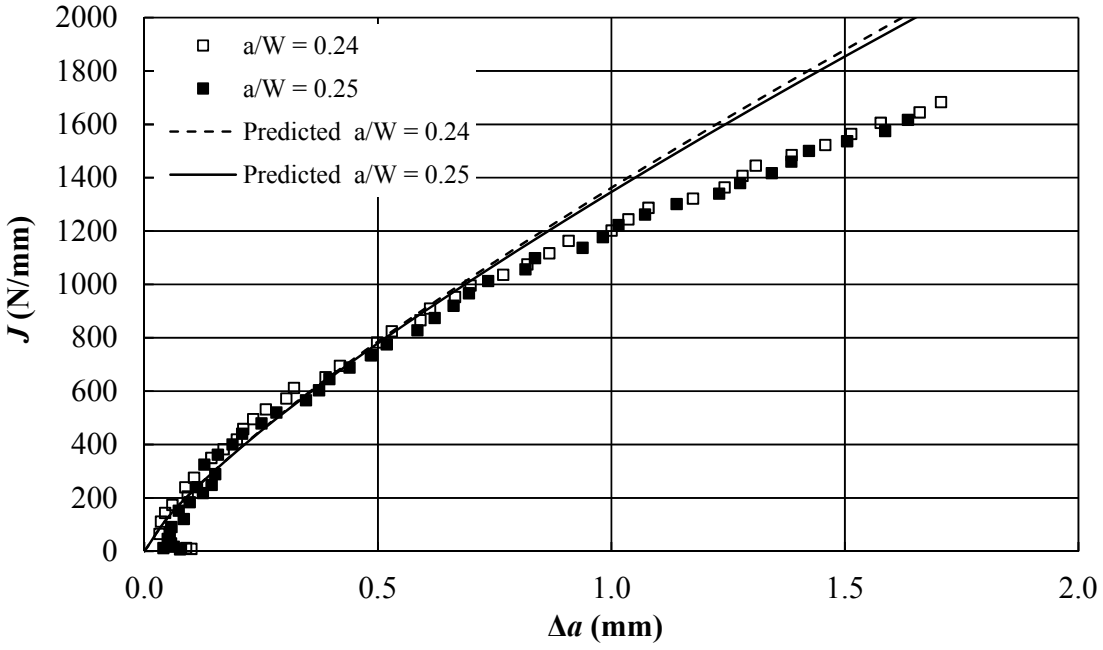

(b) Shallow-cracked specimens

Figure 3.21: Constraint-corrected *J*-R curves for SE(B) specimens based on *h*

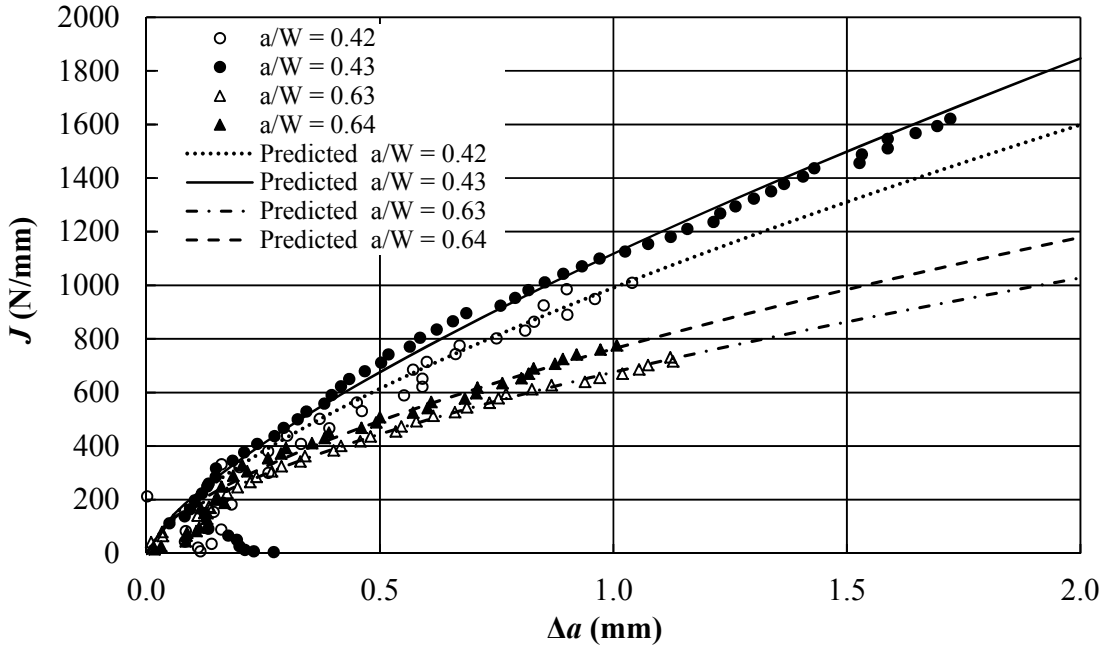

(a) Deeply- and medium-cracked specimens

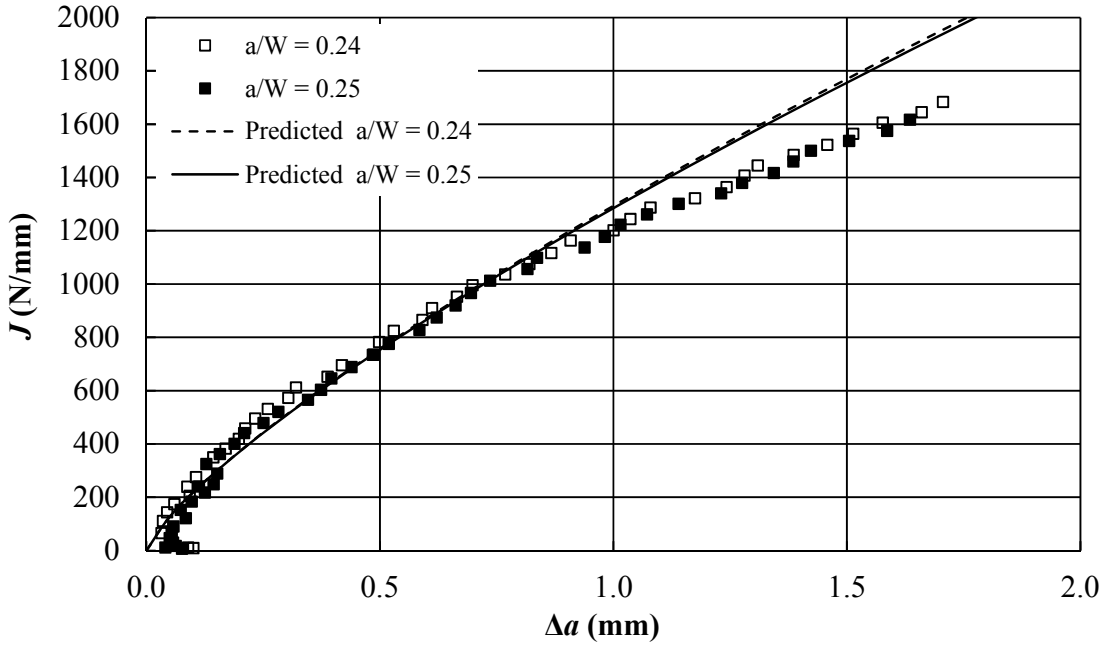

(b) Shallow-cracked specimens

Figure 3.22: Constraint-corrected *J*-R curves for SE(B) specimens based on T_z

Chapter 4 Summary and Conclusions

4.1 General

The fracture toughness of the pipe steel and weldments is a key input to the structural integrity assessment and strain-based design of energy pipelines with respect to planar defects. For ductile materials such as the modern pipe steels, the fracture process is often accompanied by relatively large plastic deformation at the crack tip and considerable crack extension. In this case, the fracture toughness is typically characterized by the so-called fracture toughness resistance curve (e.g. *J-R* curve).

The fracture toughness resistance curve is typically determined from small-scale test specimens such as the single-edge notched bend (SE(B)) and compact tension (C(T)) specimens, which have been standardized in standards such as ASTM E1820-11E2 (ASTM, 2013) and BS748 (BSI, 1997). There are two main components of a *J-R* curve, namely the crack growth, Δa, and the J value corresponding to this particular crack growth. The plastic geometry factor, i.e. the η_{pl} factor, used to estimate J in the *J-R* curve test based on the SE(B) specimen specified in the present standards are primarily obtained from the two-dimensional (2D) small-strain finite element analysis (FEA), whereas the real specimens and cracks are three-dimensional (3D). It is therefore expected that the 3D FEA will lead to more accurate evaluations of the η_{pl} factor than the 2D FEA.

It is well recognized that the fracture toughness resistance curve depends on the crack tip constraint. A high level of constraint results in a low toughness resistance curve, and a low level of constraint results in a high toughness resistance curve (Yuan and Brocks, 1998). Standard SE(B) and C(T) specimens are deeply cracked to ensure a high constraint level at the crack tip such that the corresponding toughness resistance curves represent the lower bound values. On the other hand, the crack tip constraint level for real cracks in pipelines is typically low because these cracks are generally shallow and under the tension-dominated remote stress field. The application of the fracture resistance curve obtained from high-constraint specimens to low-constraint real structures may lead to overly conservative design and assessment. One of the approaches to reduce

the conservatism is to develop constraint-corrected *J-R* curves (Chao and Zhu, 2000; Zhu and Jang, 2001; Zhu and Leis, 2005 and 2006). The constraint-corrected *J-R* curves reported in the literature are all developed based on the 2D small-strain FEA, which may not adequately simulate actual specimens that are 3D. Furthermore, the constraint parameter Q and A_2 are employed to develop the constraint-corrected *J-R* curves in the literature, whereas the use of other constraint parameters such as h and T_z has not been explored.

Given the aforementioned issues related to the *J-R* curve, two studies were carried out and are reported in this thesis. In the first study the η_{pl} factor, used to evaluate J in a *J-R* curve test based on the SE(B) specimen was developed based on the 3D FEA. In the second study, the constraint-corrected *J-R* curves for high-strength pipe steels were developed based on 3D FEA as well as the *J-R* curves experimentally determined using SE(B) specimens. The summaries and conclusions corresponding to these two studies are presented in Sections 4.2 and 4.3, respectively, followed by recommendations for future work in Section 4.3.

4.2 Evaluation of Plastic Geometry Factors for SE(B) Specimens Based on Three-dimensional Finite Element Analysis

Three-dimensional FEA was carried out to perform a systematic investigation of the plastic η factor (η_{pl}) for SE(B) specimens. The incremental-plasticity together with the large-displacement/large-strain formulation was used in the analysis. The von Mises yield criterion with isotropic hardening was adopted. The load-line displacement (*LLD*)- and crack mouth opening displacement (*CMOD*)-based η_{pl} factors corresponding to the average J value over the crack front as well as the local J value at the mid-plane were evaluated and tabulated. The impact of *a/W*, *B/W*, side-grooves and strain hardening characteristics on η_{pl} was investigated.

Three values of the strain hardening exponent, namely n = 5, 10 and 15, were considered to investigate the influence of n on η_{pl}. The baseline cases were chosen as those cases

with n = 10. For cases with n = 5 and 10, both plane-sided (PS) and side-grooved (SG) specimens were studied with three specimen thicknesses (B) (i.e. B/W = 0.5, 1 and 2), and six crack lengths (a/W) (i.e. a/W = 0.3 to 0.7 with an increment of 0.1). For cases with n = 15 materials, only plane-sided specimens with B/W = 0.5 and three crack lengths (i.e. a/W = 0.3, 0.5, and 0.7) were investigated. The 8-node 3D brick elements with 2×2×2 integration were used. The displacement-controlled loading was applied in the FEA. To facilitate the large-deformation calculation, a blunt crack tip with a radius r_w = 0.003 mm was modeled as well as the definition of two contact rollers which can simulate the rollers supporting and loading the specimen.

It is observed that η_{pl} is load-dependent for $P \leq 1.7P_l$, where P_l is the reference load, and becomes approximately independent of the load for $P > 1.7P_l$. Based on a previous experimental study (Wang et al., 2012) and consideration of the path-independence of J, the η_{pl} factors investigated in this study was evaluated based on a certain range of $\bar{J}_{pl}$ vs. $\bar{A}_{pl}$ data, where $\bar{J}_{pl}$ and $\bar{A}_{pl}$ are non-dimensionalized J and plastic area, respectively. For materials with n = 5 and 10, the η_{pl} factors for specimens with $a/W \geq 0.4$ were evaluated by linearly fitting the $\bar{J}_{pl}$ vs. $\bar{A}_{pl}$ data corresponding to $1.0P_l \leq P \leq 2.0P_l$. The η_{pl} factors for specimens with a/W = 0.3 were evaluated based on data within the range of $1.0P_l \leq P \leq 1.7P_l$. For n =15 materials, η_{pl} was evaluated based on data within the range of $1.0P_l \leq P \leq 1.7P_l$ for specimens with $a/W \geq 0.4$, and $1.0P_l \leq P \leq 1.5P_l$ for specimens with a/W = 0.3.

For the baseline case, i.e. n = 10, it is observed that the B/W ratio and side-grooves have an observable impact on η_{pl}, and η_{mid} tends to be more impacted by B/W and side-grooves than η_{ave}. The value of η_{mid} generally decreases as the B/W ratio increases. Except for the side-grooved specimens with a/W = 0.6 and 0.7, the η_{ave}^{LLD} values obtained in this study are generally lower than 1.9 that is suggested in ASTM E1820-11E2 for deeply-cracked (i.e. $0.45 \leq a/W \leq 0.7$) SE(B) specimens; the η_{ave}^{CMOD} values obtained in this study corresponding to the plane-sided and side-grooved specimens with $a/W \geq 0.4$ are generally lower and higher than those evaluated from the equation suggested in ASTM E1820-11E2, respectively, and for both the plane-sided and side-grooved specimens with a/W = 0.3, the η_{ave}^{CMOD} values obtained in this study are somewhat higher than those

evaluated from the ASTM E1820-11E2 equation. Both *LLD*- and *CMOD*-based η_{pl} for specimens with $B/W = 0.5$ and $a/W = 0.5$ and 0.7 are found to be insensitive to the strain hardening exponent n in the range of $n = 10$ to 15, whereas η_{pl} for the same specimens are found to be sensitive to n in the range $n = 5$ to 10.

The results of the present study can improve the accuracy of the *J-R* curve experimentally determined from the SE(B) specimens given that the 3D FEA employed in the study can more realistically simulate the real specimens than the conventional 2D FEA. The research outcome also facilitates the evaluation of *J-R* curves using non-standard (e.g. shallow-cracked) SE(B) specimens.

4.3 Constraint- corrected *J-R* Curves for Pipeline Steels

The constraint- corrected *J-R* curves for X80 grade pipeline steel were developed based on 3D FEA. The constraint parameters for a set of SE(B) specimens reported in the literature were evaluated using 3D large displacement/large strain FEA. The constraint parameters were combined with the experimentally determined *J-R* curves corresponding to medium- and deeply cracked SE(B) specimens to develop constraint corrected *J-R* curve.

Six side-grooved SE(B) specimens with different crack lengths (a/W) (i.e. $a/W = 0.24$, 0.25, 0.42, 0.43, 0.63 and 0.64) and same thickness (B/W) (i.e. $B/W = 0.5$) were investigated in the FEA. The 8-node 3D isoparametric brick elements with 2×2×2 integration were used with the displacement-controlled loading applied in the FEA. A blunt crack tip with a radius $r_w = 0.003$ mm was modeled to facilitate the large-deformation calculation. Two contact rollers were defined to simulate the rollers supporting and loading the specimen.

Four constraint parameters Q, A_2, h and T_z were considered in this study where the Q parameters investigated in this study include Q_{HRR}, the load-independence corrected Q, Q_m, and bending-corrected Q, Q_{BM1} and Q_{BM2}. The *J-R* curves of the four medium- and deeply-cracked specimens (i.e. $a/W = 0.64$, 0.63, 0.43 and 0.42) were used to develop the

constraint-corrected *J-R* curves, whereas the *J-R* curve of the two shallow-cracked specimens (i.e. a/W = 0.24 and 0.25) were used to validate the developed constraint-corrected *J-R* curve. The errors of the *J* values corresponding to crack extensions of 0.2, 0.5, 0.7, 1.0, 1.2 and 1.5 mm in the predicted *J-R* curves were evaluated to examine the accuracy of the developed constraint-corrected *J-R* curve based on different constraint parameters. Three constraint parameters, namely Q_{BM1}, T_z and A_2, are considered adequate for developing the constraint-corrected *J-R* curve based on SE(B) specimens, with the maximum error of prediction being less than 16% for a wide range of crack extensions (0.2 mm < $\Delta a \leq$ 1.5 mm). On the other hand, Q_{HRR}, Q_{BM2} and Q_m are considered inadequate for characterizing the constraint-corrected *J-R* curve because the errors in the predicted *J* values are relatively large (maximum error of around 25%) for 0.7 mm < $\Delta a \leq$ 1.5 mm. Further investigations on more SE(B) specimens are needed to support this conclusion.

The developed constraint-corrected *J-R* curve can be applied to actual pipelines containing cracks with the assistance of FEA. Three-dimensional FEA of the pipelines under the applicable loading conditions needs to be carried out to determine the value of the constraint parameter (e.g. Q_{BM1}, h and T_z) at the mid-plane along the crack front. The value of the constraint parameter can then be substituted into the constraint-corrected *J-R* curve to develop the *J-R* curve that is specific for the particular pipeline. This *J-R* curve can then be used to accurately evaluate the structural integrity of the pipeline.

4.4 Recommendations for Future Work

Recommendations for future work are as follows:

1) Further studies can be carried out to develop empirical equations for *LLD*-based and *CMOD*-based η_{pl} as a function of a/W, B/W and n for the SE(B) specimens based on the results reported in Chapter 2, which will facilitate the *J-R* curve testing for a wide range of geometric configurations and crack lengths of SE(B) specimens.

2) Systematic 3D FEA-based investigations of the η_{pl} factor for C(T) and SE(T) specimens, similar to that carried out in Chapter 2 for the SE(B) specimen, can be performed.

3) The η_{pl} factor for specimens containing weldment should be evaluated and compared with those for specimens made of the base metal only.

4) To develop more generally applicable constraint-corrected *J-R* curves, experimentally-determined *J-R* curves and constraint parameters for different types of specimens such as C(T) and SE(T) should be involved in the study.

References

ASTM. ASTM E1820-11E2: *Standard Test Method for Measurement of Fracture Toughness*, ASTM, West Conshohocken, PA; 2013.

BSI. *BS 7448: Fracture Mechanics Toughness Tests*, British Standard Institution, London; 1997.

Chao YJ, Zhu XK. Constraint-Modified *J-R* Curves and Its Applications to Ductile Crack Growth. *International Journal of Fracture Mechanics*; 2000;106:135-60.

Dodds RH, Ruggier C, Koppenhefer K. 3D Constraint effects on models for transferability of cleavage fracture toughness. *ASTM STP 1321*, 1997:179-97.

Wang E, Zhou W, Shen G, Duan D. An Experimental Study on *J*(*CTOD*)-*R* Curves of Single Edge Tension Specimens for X80 Steel. *Proceedings of the 2012 9th Iternational Pipeline Conference*, September 24-28, Calgary, Canada; 2012. p. IPC2012-90323.

Yuan H, Brocks W. Quantification of Constraint Effects in Elastic-plastic Crack Front Fields. *Journal of the Mechanics and Physics of Solids*; 1998;46(2);219-41.

Zhu XK, Jang SK, *J-R* Curves Corrected by Load-Independent Constraint Parameter in Ductile Crack Growth. *Engineering Fracture Mechanics*; 2001;68:285-301.

Zhu XK, Leis BN, Joyce JA. Constraint Corrected *J-R* Curves and Its Application to Fracture Assessment for X80 Pipelines. *Journal of ASTM International*; 2005;3(6):1-17.

Zhu XK, Leis BN, Joyce JA. Application of Constraint Corrected *J-R* Curves to Fracture Analysis of Pipelines. *Journal of Pressure Vessel Technology*; 2006;128:581-9.

Appendix A Computation of *J*-integral using Virtual Crack Extension Method

Parks (1974) and Hellen (1975) first developed the virtual crack extension approach based on the finite element method to calculate the energy release rate in elastic bodies (Anderson, 2005). deLorenzi (1982, 1985) improved the virtual crack extension method, which is used in the FEA reported in this thesis and is briefly described here.

Figure A.1 schematically shows the virtual crack extension method in two-dimensional analysis. The crack front is surrounded by three zones of material divided by two contours. During the crack advance, material points in zone I are rigidly translated in the x_1 direction by an amount Δx_1, while points in zone III remain fixed, causing a distortion in the material in zone II. Since zone I contains the crack front, the crack length is increased by an amount Δa. This virtual translation of the material points is defined as the "virtual shift" in ADINA (ADINA, 2012). For a material that obeys the deformation plasticity theory, deLorenzi (1982, 1985) showed that the energy release rate in a two-dimensional body can be expressed as:

$$J = \frac{1}{\Delta a}\int_{A_C}\left(\sigma_{ij}\frac{\partial u_j}{\partial x_1} - w\delta_{i1}\right)\frac{\partial \Delta x_1}{\partial x_i}dA_C \tag{A.1}$$

where u_i is components of the displacement (i = 1 or 2); w is the strain energy density; A_C is area of the cracked body, and δ_{ij} is the Kronecker delta.

In the virtual crack extension method adopted in ADINA (ADINA, 2012), a more general form of Eq. (A.1) is used to calculate J considering 3D cracked body (deLorenzi, 1982 and 1985):

$$J = \frac{1}{\Delta A_C}\int_{V_C}\left(\sigma_{ij}\frac{\partial u_i}{\partial x_k} - w\delta_{ik}\right)\frac{\partial \Delta x_k}{\partial x_j}dV_C \tag{A.2}$$

where V_C is volume of the cracked body; Δx_k is components of the virtual crack extension vector (k = 1, 2 or 3), and ΔA_C is the increase in crack area corresponding to Δx_k.

The calculation of ΔA_C is discussed here. For a 2D cracked body, $\Delta A_C = b\sqrt{\Delta x_1^2 + \Delta x_2^2}$ where b is the thickness at the crack tip. Figure A.2 schematically shows the virtual shift in 3D analysis. For a 3D cracked body, $\Delta A_C = \int \sqrt{\Delta x_i' \Delta x_i'}\, ds$ where $\Delta x_i' = \Delta x_i - (\sum_{j=1}^{3} t_j \Delta x_j) t_i$, t_i (i = 1, 2 or 3) is the component or directional cosine of the unit tangent vector along the crack front and ds is the differential length along the crack front (see Fig. A.2). The definition of $\Delta x_i'$ ensures that it is perpendicular to t_i. In a 3D problem, J typically varies along the crack front. Defining ΔA_C in the above way would result in a local measure of J (Anderson, 2005).

The virtual crack extension formulation of J requires an area integration and a volume integration for 2D and 3D analysis, respectively. Such an approach is easier to implement numerically and is more accurate than contour and surface integrations for 2D and 3D problems, respectively (Anderson, 2005). Note that Eq. (A.2) is the basic expression of J and does not consider the impacts of hoop stress and pressure, thermal effect, and dynamic effect (ADINA, 2012). Additional information about the virtual crack extension approach can be found in the relevant literature (e.g. ADINA, 2012; Anderson, 2005; deLorenzi, 1982 and 1985; Hellen, 1975).

References

Anderson TL. *Fracture Mechanics—Fundamentals and Applications*, Third edition. CRC Press, Boca Raton; 2005.

ADINA. *Theory and Modeling Guide*, ADINA R. & D. Inc., Watertown, USA; 2012.

deLorenzi HG. On the Energy Release Rate and the *J*-Integral of 3-D Crack Configurations. *International Journal of Fracture*; 1982;19:183-93.

deLorenzi HG. Energy Release Rate Calculation by the Finite Element Method. *Engineering Fracture Mechanics*; 1985;21:129-43.

Hellen TK. On the Method of Virtual Crack Extension. *International Journal for Numerical Methods in Engineering*; 1975;9:187-207.

Parks DM. A Stiffness Derivative Finite Element Technique for Determination of Crack Tip Stress Intensity Factors. *International Journal of Fracture*; 1974;10:487-502.

I: zone rigidly shifted by virtual shift

II: zone distorted by virtual shift

III: zone unchanged by virtual shift

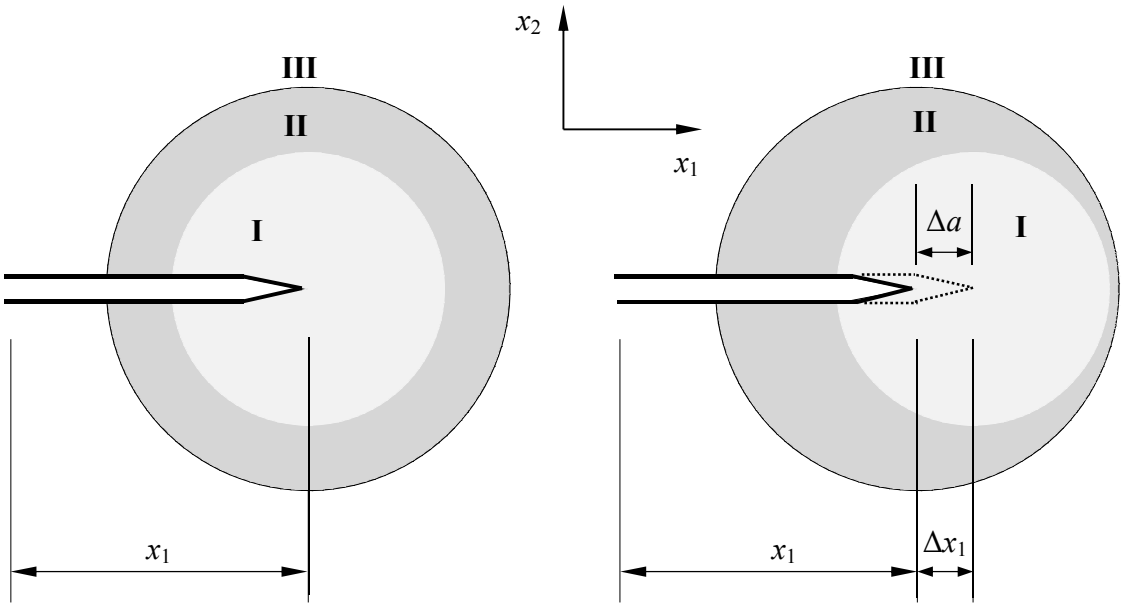

(a) Before the virtual shift **(b) After the virtual shift**

Figure A.1: The virtual crack extension method in two-dimensional analysis

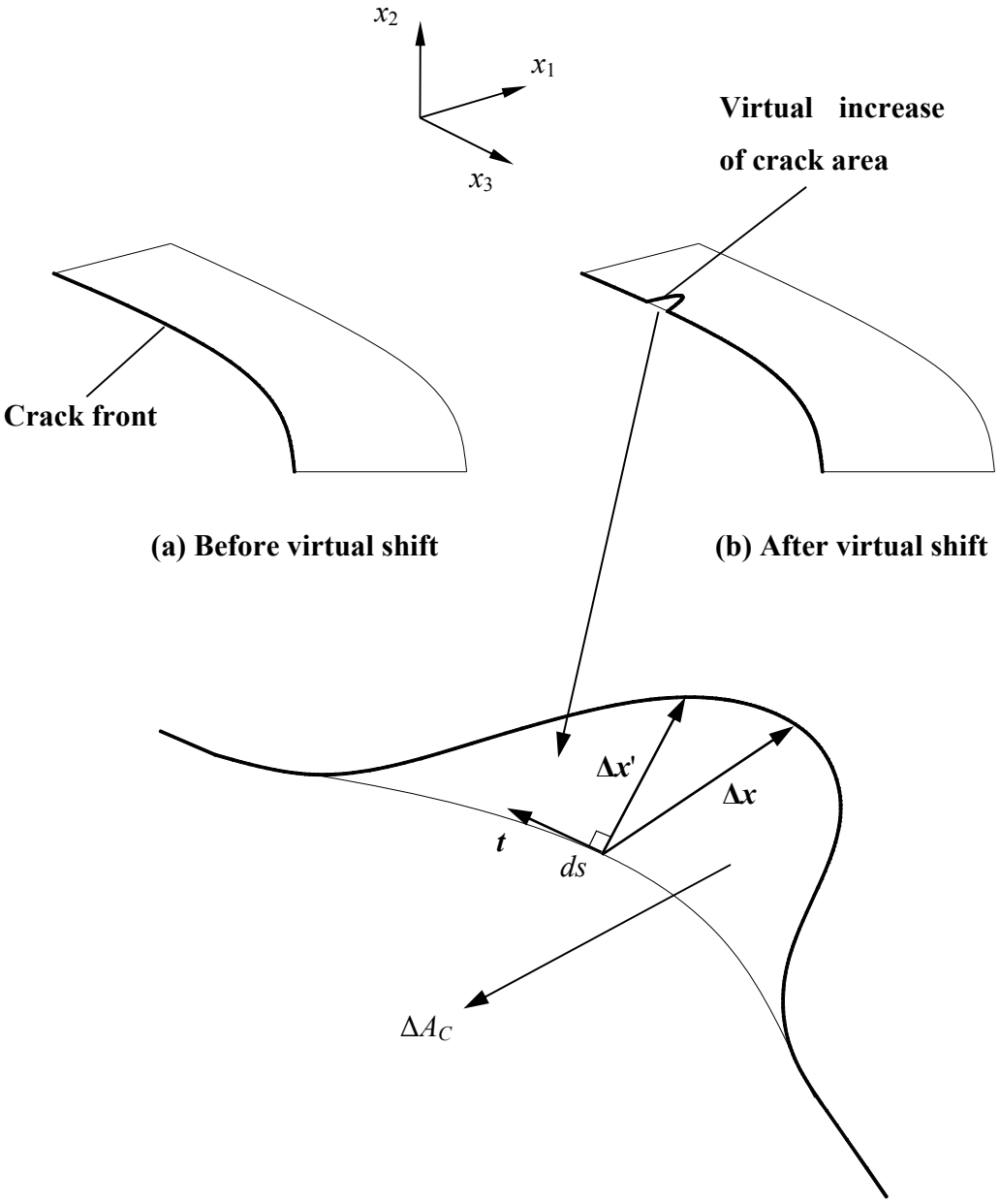

Figure A.2: The virtual shift in three-dimensional analysis

Appendix B Unloading Compliance Method for Evaluating the Crack Length

The elastic unloading compliance method (Clarke et al., 1976) is used to evaluate the immediate crack length and plastic work done in the specimen. Figure B.1 schematically shows the elastic unloading compliance method. A number of loading-unloading-reloading sequences were conducted to each specimen during the test. At loading step *i* during the test, the slope of the corresponding unloading line was evaluated by the least square fit to obtain the instant compliance C_i (i.e. the inverse of the stiffness), which is a function of the instant crack length, a_i (see Fig. B.1). The extended unloading line (see Fig. B.1) can separate the total area under the load-displacement curve into an elastic component and a plastic component in order to determine the instant η_{pl} factor as described in Section 2.1.2 (see Fig. 2.3). The relationship between the compliance and the crack length can be written in the following general expression (Tada *et al*., 2000):

$$E'BC_i = f\left(\frac{a_i}{W}\right) \tag{B.1}$$

where *E'* is the effective modulus of elasticity (*E'*= *E* for the plane stress condition, and *E'*= $E/(1-\nu^2)$ for the plane strain condition); *B* is the thickness of the specimen, and *f* is a function that depends on the specimen type and loading configuration. In order to predict the instantaneous crack length from the compliance, Eq. (B.1) can be recast as

$$\frac{a_i}{W} = g\left(E'BC_i\right) \tag{B.2}$$

where the compliance C_i can be determined based on either *LLD* or *CMOD*. Note that *CMOD* is usually preferred over *LLD* for predicting *a*/*W* because the former can be more easily and accurately measured than the latter (Zhu et al., 2008). The function *g* in Eq. (B.2) has been investigated extensively in the literature for different fracture toughness specimens corresponding to *CMOD*-based compliances, C_i^{CMOD} (e.g. Wu, 1984; Joyce, 1992; Saxena and Hudak, 1978; Shen and Tyson, 2009).

Wu (1984) proposed the following equation for deeply-cracked ($0.45 \le a/W \le 0.7$) SE(B) specimens, which has been adopted in ASTM E1820-11E2:

$$\begin{cases} \dfrac{a_i}{W} = 0.9997482 - 3.9504u_i + 2.9821u_i^2 - 3.21408u_i^3 \\ \qquad +51.51564u_i^4 - 113.031u_i^5 \\ u_i = \dfrac{1}{\sqrt{\dfrac{B_e W C_i^{CMOD} E'}{S/4}} + 1} \end{cases} \tag{B.3}$$

where $B_e = B - (B - B_N)^2/B$ (ASTM, 2011) is the effective specimen thickness. For shallow-cracked ($0.05 \le a/W \le 0.45$) SE(B) specimen, it is recommended in ASTM E1820-11E2 that a_i/W be calculated as follows (Joyce, 1992):

$$\begin{cases} \dfrac{a_i}{W} = 1.01878 - 4.5367u_i + 9.0101u_i^2 - 27.333u_i^3 \\ \qquad +74.4u_i^4 - 71.489u_i^5 \\ u_i = \dfrac{1}{\sqrt{\dfrac{B_e W C_i^{CMOD} E'}{S/4}} + 1} \end{cases} \tag{B.4}$$

For C(T) specimens, Saxena and Hudak (1978) developed the following equation to estimate the crack length, which has been adopted in ASTM E1820-11E2:

$$\begin{cases} \dfrac{a_i}{W} = 1.000196 - 4.06319u_i + 11.242u_i^2 - 106.043u_i^3 \\ \qquad +464.335u_i^4 - 650.677u_i^5 \\ u_i = \dfrac{1}{\sqrt{B_e C_{c(i)}^{CMOD} E'} + 1} \end{cases} \tag{B.5}$$

Shen and Tyson (2009) developed the following expression of a/W for the clamped SE(T) specimens with a daylight over width ratio of 10 (i.e. H/W = 10), which has not been standardized:

$$\begin{cases} \dfrac{a_i}{W} = 2.072 - 16.411u_i + 79.600u_i^2 - 211.670u_i^3 + 236.857u_i^4 \\ \qquad +27.371u_i^5 - 179.740u_i^6 - 86.280u_i^7 + 171.764u_i^8 \\ u_i = \dfrac{1}{\sqrt{B_e C_{c(i)}^{CMOD} E' + 1}} \end{cases} \tag{B.6}$$

The parameter $C_{c(i)}^{CMOD}$ in Eq. (B.5) and (B.6) is the rotation corrected compliance. Detailed procedures to account for the rotation correction for the C(T) and SE(T) specimens are not discussed in this thesis and can be found in the relevant literature (e.g. Gray et al., 1979; Joyce and Link, 1995; Cravero and Ruggieri, 2007; Shen and Tyson, 2009).

References

ASTM. ASTM E1820-11E2: *Standard Test Method for Measurement of Fracture Toughness*, ASTM, West Conshohocken, PA; 2013.

Clarke GA, Andrews WR, Paris PC, Schmidt DW. Single Specimen Tests for J_{Ic} Determination. *Mechanics of Crack Growth, ASTM STP 590, American Society for Testing and Materials*, Philadelphia; 1976;27-42.

Cravero S, Ruggieri C. Estimation Procedure of *J-R*esistance Curves for SE(T) Fracture Specimens Using Unloading Compliance. *Engineering Fracture Mechanics*; 2007;74:2735–57.

Gray RA, Loss FJ, Menke BH. Development of *J-R* Curve Procedures. NRL-EPRI Research Program (RP 886.2), Evaluation and Prediction of Neutron Embrittlement in

Reactor for CY 1978, NRL Report 8327, Naval Research Laboratory, Washington, D.C.; 1979.

Joyce JA. *J* Resistance Curve Testing of Short Crack Bend Specimens Using Unloading Compliance. *Fracture Mechanics*, *Twenty-Second Symposium*, *ASTM STP 1131*, American Society for Testing and Materials, West Conshohocken, PA; 1992;1:904-26.

Joyce JA, Link RE. Effect of Constraint on Upper Shelf Fracture Toughness. *Fracture Mechanics*, *ASTM STP 1256*, ASTM International, West Conshohocken, PA; 1995;26:142–77.

Saxena A, Hudak SJ. Review and Extension of Compliance Information for Common Crack Growth Specimens. *International Journal of Fracture*; 1978;14(5):453-68.

Shen G, Tyson WR. Crack Size Evaluation Using Unloading Compliance in Single-specimen Single-edge-notched Tension Fracture Toughness Testing. *Journal of Testing and Evaluation*; 2009;37(4):347–57.

Tada H, Paris PC, Irwin GR. *The Stress Analysis of Cracks Handbook*, Third edition. ASME Press, New York; 2000.

Wu S. Crack Length Calculation Formula for Three Point Bend Specimens. *International Journal of Fracture*; 1984;24(1):33-8.

Zhu XK, Leis BN, Joyce JA. Experimental Estimation of *J-R* Curves From Load-*CMOD* Record for SE(B) Specimens. *Journal of ASTM International*; 2008;5:231–45.

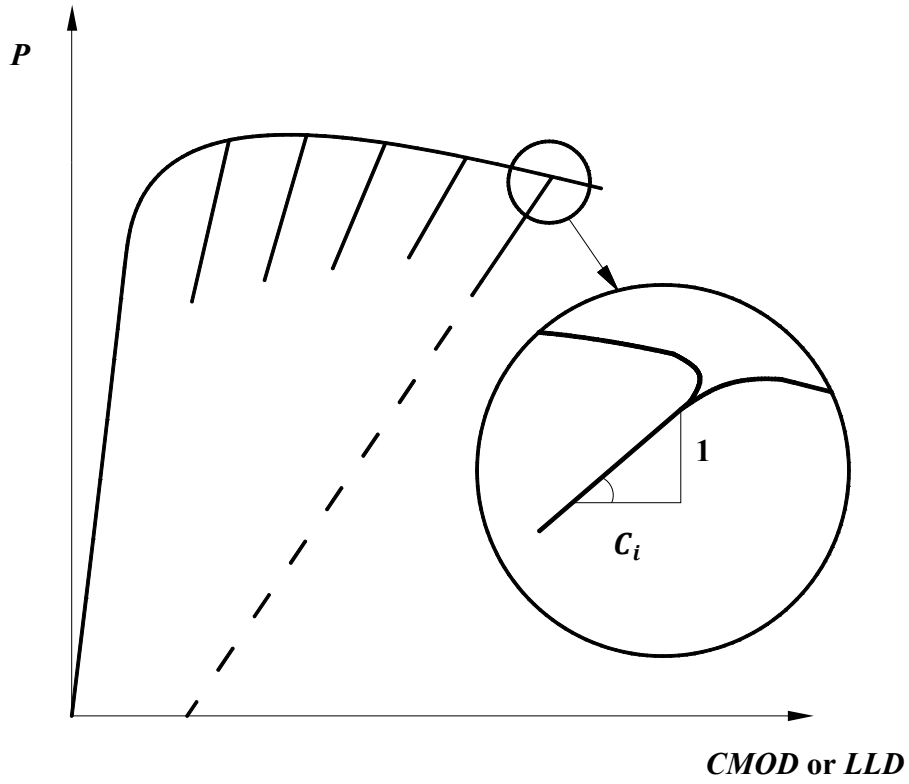

Figure B.1: Schematic of the elastic unloading compliance method

Curriculum Vitae

Name: Yifan HUANG

Post-secondary Education and Degrees:
China University of Mining and Technology
Xuzhou, Jiangsu, China
2007-2011, B.E.Sc. (Civil Engineering)

The University of Western Ontario
London, Ontario, Canada
2011-2013, M.E.Sc. (Structural Engineering)

Honours and Awards:
Scholarship of Excellent Student, CUMT
2007-2010

Related Work Experience
Teaching Assistant
The University of Western Ontario
2011-2013

Research Assistant
The University of Western Ontario
2011-2013

Publications:

Huang Y, Zhou W, Wang E, Shen G. Evaluation of Plastic η Factors for SE(B) Specimens Based on Three-dimensional Finite Element Analysis. *Proc 23rd Int Offshore and Polar Eng Conf*, June 30 - July 5, Anchorage, ISOPE; 2013:591-7.